

Pulsar-wind nebulae and magnetar outflows: observations at radio, X-ray, and gamma-ray wavelengths

Stephen P. Reynolds · George G. Pavlov · Oleg Kargaltsev · Noel Klingler · Matthieu Renaud · Sandro Mereghetti

Received: date / Accepted: date

Abstract We review observations of several classes of neutron-star-powered outflows: pulsar-wind nebulae (PWNe) inside shell supernova remnants (SNRs), PWNe interacting directly with interstellar medium (ISM), and magnetar-powered outflows. We describe radio, X-ray, and gamma-ray observations of PWNe, focusing first on integrated spectral-energy distributions (SEDs) and global spectral properties. High-resolution X-ray imaging of PWNe shows a bewildering array of morphologies, with jets, trails, and other structures. Several of the 23 so far identified magnetars show evidence for continuous or sporadic emission of material, sometimes associated with giant flares, and a few “magnetar-wind nebula” have been recently identified.

Keywords First keyword · Second keyword · More

1 Introduction

Pulsars emit relativistic winds in a variety of forms, not well understood at this time. The outflows consist of some combination of highly relativistic leptons (e^+/e^- pairs) and perhaps ions as well, and magnetic field. The winds initially appear to be “dark” because they are cold in the comoving frame, but become thermalized somehow at a wind termination shock, which may or may not resemble a traditional perpendicular shock. Its location is fixed by pressure balance between the outgoing wind and the local ambient medium, which is either a shell supernova-remnant (SNR) interior (see Fig. 1), or for older pulsars that have outlived their SNR, undisturbed interstellar medium (ISM). Beyond this point, radiation from the outflows is apparent, and the observed object is known as a pulsar-wind nebula (PWN). [See Gaensler and Slane (2006) and Kargaltsev and Pavlov (2008) for general reviews of PWNe.] The broadband spatially integrated spectral-energy distribution (SED) appears to consist of two parts: a lower-energy spectrum of synchrotron emission, responsible for emission from

S. Reynolds
Physics Department, North Carolina State University
Tel.: +01-919-515-7751
Fax: +01-919-515-6538
E-mail: reynolds@ncsu.edu

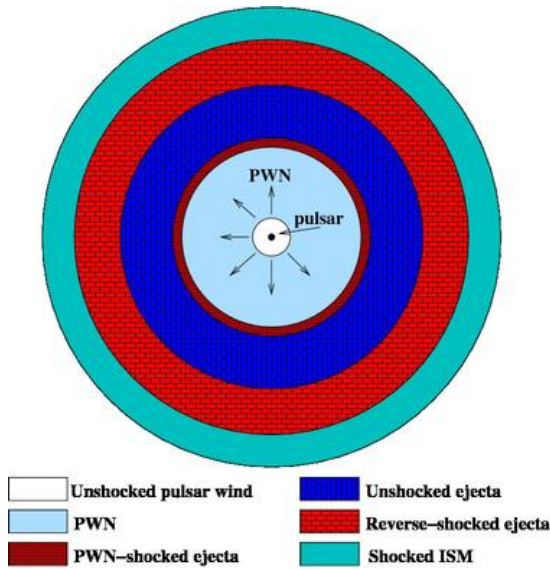


Fig. 1 Cartoon of PWN inside a shell SNR. The SNR blast wave is the outermost circle.

low radio frequencies to X-rays and into the MeV range (in the few cases where it is detectable at those energies), and a higher-energy spectrum in the GeV-TeV range, in most cases attributed to inverse-Compton upscattering of any of various possible photon fields: the PWN's own synchrotron photons ("synchrotron self-Compton," SSC), the cosmic microwave background (ICMB), or local optical/IR radiation fields. In a few cases, it may be that this emission is produced by relativistic ions colliding inelastically with thermal gas and producing both charged and neutral pions. The π^0 mesons decay to photons, producing a continuum above the kinematic threshold of about 150 MeV. But this hadronic process is not thought to be a major contributor to most PWN GeV-TeV spectra.

We structure this review mainly from young to older objects. Pulsars live far longer than their natal supernova remnant, so a relatively small fraction of PWNe should still be found within a SNR. However, this subclass offers an excellent chance to understand pulsar outflows, as information from the SNR can add to what can be deduced from the PWN alone. Other PWNe without clear evidence of a surrounding shell still have unmistakable signs of youth. The first part of this review will focus on those two subclasses, on their integrated SEDs and on their spatially resolved spectral properties. Pulsars older than the typical lifetime of an SNR continue to emit winds, which interact directly with the surrounding medium. The second part of this review deals with radio and X-ray emission from these PWNe. Some of both young and older X-ray PWNe emit gamma-rays as well, but the gamma-ray class is predominantly made up of much older objects which may be unprepossessing or undetectable at longer wavelengths. The third part of the review covers the gamma-ray properties of PWNe of all ages. Finally, magnetars have unique characteristics in terms of outflows; these characteristics are described in the last part of this chapter.

While the gross properties of PWNe (mean sizes, integrated spectra) provide one kind of information on the basic physics, a great deal can also be learned from detailed morphological investigations. The *Chandra* X-ray Observatory has provided a rich collection of imaging information down to sub-arcsecond scales, and we review that collection as well. Many of

these objects are also older, with the pulsar wind interacting directly with ISM, sometimes in a well-defined bow shock, but in other cases in unusual and perplexing morphologies. Finally, we describe evidence for outflows from magnetars, neutron stars with very strong magnetic fields and a propensity to emit giant flares. Evidence for ejection of material seems strong. While clear cases of steady outflows (“magnetar-wind nebulae”) have not yet been firmly confirmed, candidates have been identified. We also mention gamma-ray binaries, in which the relativistic pulsar wind interacts with a wind from the binary companion, but these systems are described more fully elsewhere.

2 Synchrotron emission from young pulsar-wind nebulae: radio to X-rays

The synchrotron spectrum of PWNe contains the most specific information about the particle spectrum injected into the nebula at the wind termination shock (WTS), though the unknown magnetic-field structure can complicate the extraction of that information. Furthermore, the injected spectrum can change with time and location, due to evolutionary effects and particle propagation, e.g., advection or diffusion. Disentangling these effects is essential to understand the nature of particle energization at the WTS.

Figure 2 illustrates four PWN/SNR combinations, in which the pulsars are well studied. The PWNe are asymmetric and structured, and for G292.0+1.8, not centered on the pulsar. However, these systems are amenable to detailed interpretation based on analysis of both the PWN nonthermal radiation and the properties of the surrounding SNR. In both B0540–693 (Williams et al. 2008) and G11.2–0.3 (Borkowski et al. 2016), the PWN’s interaction with the SNR inner ejecta is important in the overall characterization of the object.

Young objects like the Crab or 3C 58 (unlikely to be the remnant of an event in 1181 AD, but still only of order 2000 yr old; Chevalier 2005), without clear evidence of a shell, also show properties consistent with expansion into a low-density medium which is probably itself expanding. Simple 1-D models show that as long as the pulsar maintains its original energy-loss rate, the PWN expands into uniformly expanding ejecta with radius $R \propto t^{6/5}$ (Reynolds and Chevalier 1984; van der Swaluw et al. 2001), producing a shock wave into the inner ejecta that strengthens with time. (See Fig. 1).

These two classes of young PWNe, with and without SNR shells, will be the focus of this section.

2.1 General properties of the PWN synchrotron spectrum

Pulsar-wind nebulae were originally defined by radio properties: “flat” radio spectrum (that is, energy spectral index $\alpha \sim 0 - 0.4$ where $S_\nu \propto \nu^{-\alpha}$ is the energy flux), center-brightened morphology, and high radio polarization (e.g., Weiler and Panagia 1978). The catalog remained small, however, until the high spatial resolution of *Chandra* and *XMM-Newton* allowed the identification of PWNe in shells and in confused regions, at which point a large increase in identified PWNe began which continues to this day. The catalog by Kargaltsev et al. (2013) lists 70 X-ray PWNe with known pulsars, and 6 more objects identified at gamma-ray energies without currently known X-ray counterparts. Many of the PWNe discovered at X-ray or gamma-ray energies have weak, poorly known, or undetectable radio emission. In Green’s catalog of SNRs and PWNe (Green 2009), 26 PWNe in shells (formerly known as “composite” SNRs) and another 13 isolated PWNe (once called “plerions”)

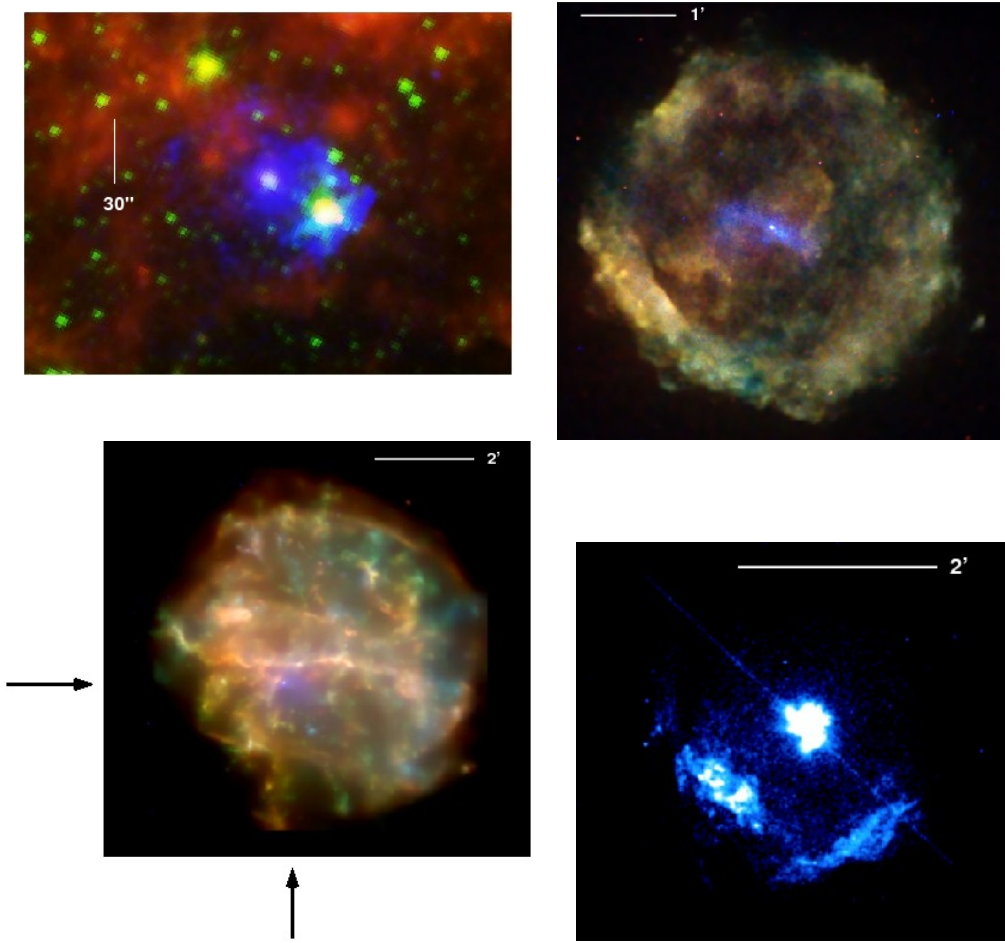


Fig. 2 Upper left: B0540–693 in the Large Magellanic Cloud (Williams et al. 2008). Red, *Spitzer* 8 μm ; green, *Spitzer* 3.6 μm ; blue, *Chandra* 0.5 – 8 keV. The pulsar and surrounding PWN is barely resolved at the center of the frame, just above and to the left of the bright foreground star. Upper right: G11.2–0.3 with *Chandra* (Borkowski et al. 2016). Red: 0.6 – 1.2 keV; green, 1.2 – 3.3 keV; blue, 3.3 – 8 keV. The PWN is visible in blue. Lower left: G292.0+1.8 with *Chandra* (Park et al. 2007). Red: 0.3 – 0.8 keV; green, 0.8 – 1.7 keV; blue, 1.7 – 8 keV. The PWN is the purplish region slightly SE of the center, and the pulsar (indicated by arrows) is at its NE edge. Lower right: Kes 75 with *Chandra* (Gavril et al. 2008). The pulsar is highly piled up, as the readout streak indicates.

are listed. This catalog began as a listing of radio SNRs, and does not include pulsar bow-shock nebulae or other manifestations of pulsar outflows without clear radio counterparts. With the addition of two more recent discoveries, Fig. 3 shows the distribution of PWN radio spectral indices. Since there are a few good cases of steeper-spectrum PWNe ($\alpha > 0.4$), it is possible that more such objects exist but have been selected against. However, the three steep-spectrum PWNe ($\alpha \geq 0.6$) are all anomalous in other ways as well. It is also possible that some very flat-spectrum objects ($\alpha \sim 0.1$) have been mistaken for H II regions, since strong radio polarization, the usual discriminator, is not found in all objects.

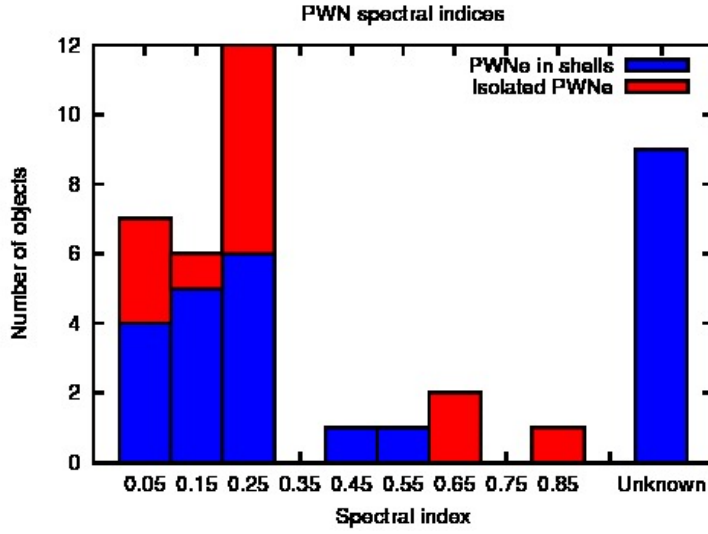


Fig. 3 Distribution of radio spectral indices α ($S_\nu \propto \nu^{-\alpha}$) of 39 PWNe in shells (blue) and isolated (red). Many of the former have poorly known radio spectral indices. Typical uncertainties on α are ± 0.1 . The three steep-spectrum PWNe ($\alpha \geq 0.6$) are all anomalous in other ways as well.

Table 1 *Spitzer* observations of PWNe

Object	Type	Detectors ^a	Result	Reference
Crab	PWN	I, M, S	Images, spectrum	Temim et al. (2006)
G21.5–0.9	PWN	I, M	Images	Zajczyk et al. (2012)
3C58	PWN	I, M	Images	Slane et al. (2008)
G54.1+0.3	PWN, IR shell	I, M, S	Images, spectrum	Temim et al. (2010)
B0540–693	PWN, shell	I, M, S	Images, spectrum	Williams et al. (2008)

^aI: IRAC (3.6, 4.5, 5.8, & 8.0 μm). M: MIPS (24, 70, 160 μm). S: IR Spectrograph (5 – 35 μm)

The three anomalous steep-spectrum PWNe are shown in Fig. 4. The first two, DA 495 and G76.9+1.0, with $\alpha = 0.87 \pm 0.1$ (Kotthes et al. 2008) and 0.62 ± 0.04 (Landecker et al. 1993), have strikingly similar double-lobed morphology, with tiny extended X-ray sources in the center of each. G141.2+5.0 (Reynolds and Borkowski 2016) shows a simple center-brightened morphology, but with a central X-ray source unresolved by *Chandra*. It is not known how these objects fit into the overall PWN scheme; no data are available for any at other wavelengths.

For many PWNe, no other observations are available at frequencies below the X-ray regime. But a few have been imaged with *Spitzer* (see Fig. 5 and Table 1). Much of the emission is thermal radiation from dust grains, or fine-structure spectral lines, but some synchrotron continuum is evident in the Crab, 3C 58, and G21.5–0.9.

PWNe are often observed to be smaller at X-ray than at longer wavelengths, as is clearly the case with the Crab Nebula. However, several other prominent PWNe show X-rays extending to the edges of the radio contours, though with greater center-to-edge brightness contrast. Figures 7 and 8 show that both 3C 58 and G54.1+0.3 have X-ray extents comparable to their radio extents.

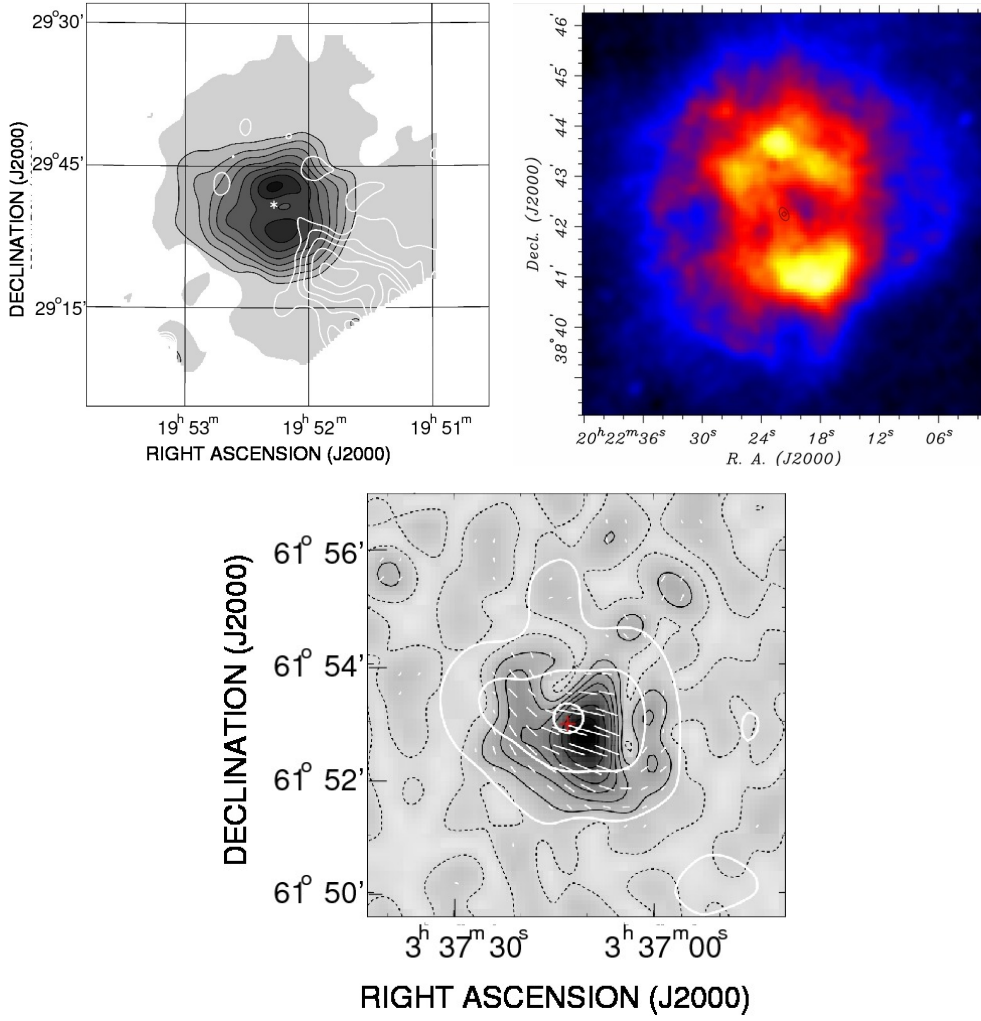


Fig. 4 Three PWNe with steep radio spectra. Upper left: DA 495 (G65.7+1.2) at 1.4 GHz. White contours: a background H II region. Asterisk: a compact X-ray source (Kotthes et al. 2008). Upper right: G76.9+1.0 (Arzoumanian et al. 2011) at 1.4 GHz. Almost invisible contours of extent about $40''$ near the center show the X-ray nebula. Bottom: G141.2+5.0 at 1.4 GHz in polarized intensity (greyscale) with contours indicating total intensity (Kotthes et al. 2014), and the red cross indicating a pointlike X-ray source (Reynolds and Borkowski 2016).

2.2 Imaging PWNe above 10 keV with *NuSTAR*

Spectral inhomogeneity in PWNe is commonly observed at X-ray energies, where energy losses are becoming important. Spectra steepen with distance from the central pulsar, presumably as higher-energy electrons are depleted. The steepening trend tends to begin immediately, as shown in Fig. 9 for three PWNe (Bocchino and Bykov 2001). This behavior is explored more fully below. This means, however, that integrated SEDs may hide important spectral variations. Unfortunately, until recently true imaging at X-ray energies above about

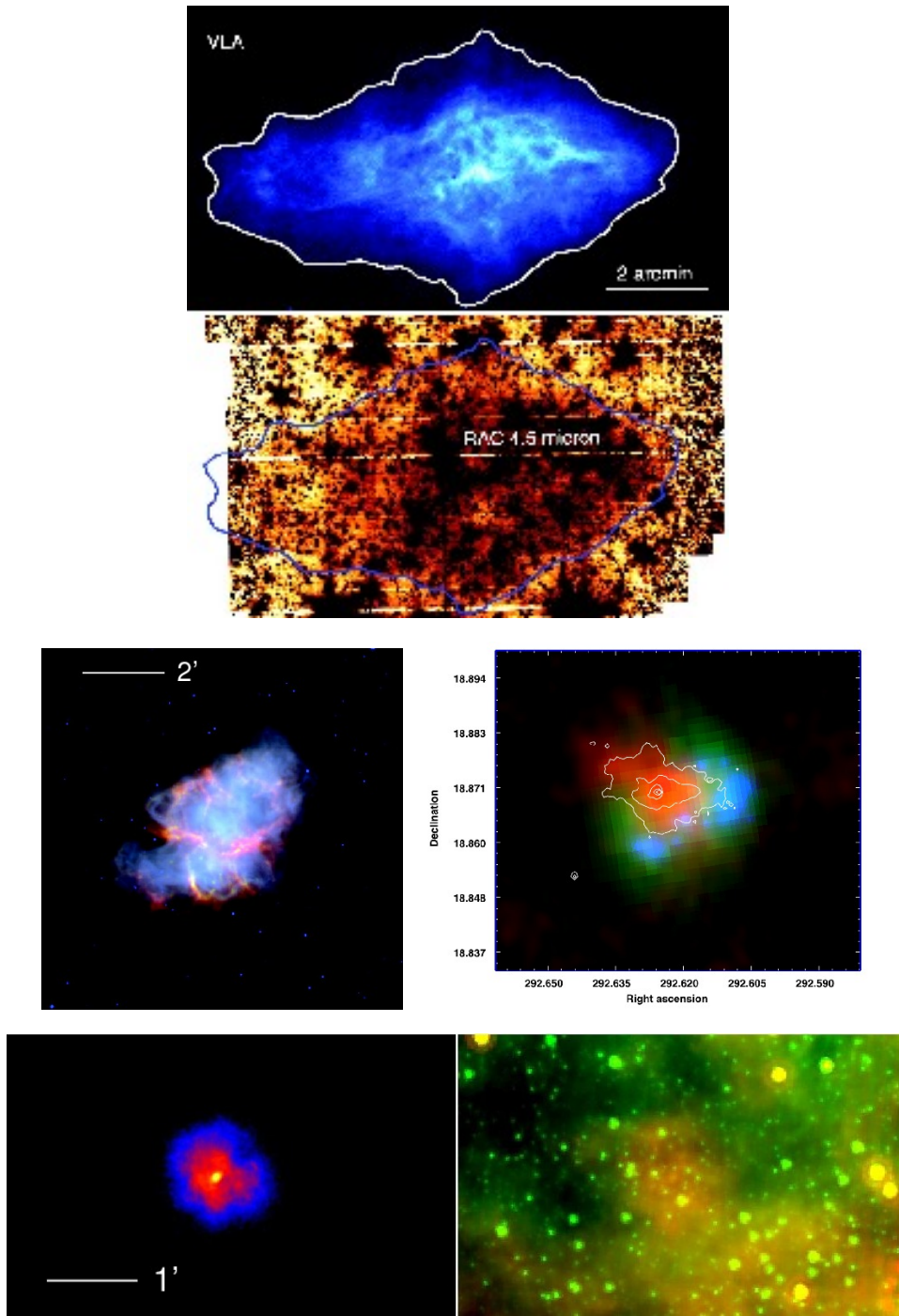


Fig. 5 Top: 3C 58 (Slane et al. 2008). (Upper: radio, VLA at 1.4 GHz (Reynolds and Aller 1988); lower, IR, *Spitzer* at 4.5 μm .) Middle left: Crab Nebula (Temim et al. 2006). Red, 24 μm (mainly [O IV] at 26 μm); green, 8 μm (mainly [Ar II] at 7 μm); blue, 3.6 μm (mainly synchrotron continuum). Middle right: G54.1+0.3 (Temim et al. 2010). Contours, X-ray. Red, radio. Green, 70 μm . Blue, 24 μm . Lower: G21.5-0.9 (Zajczyk et al. 2012). Left: *Chandra* image. Right: Red, 24 μm ; green, 8 μm .

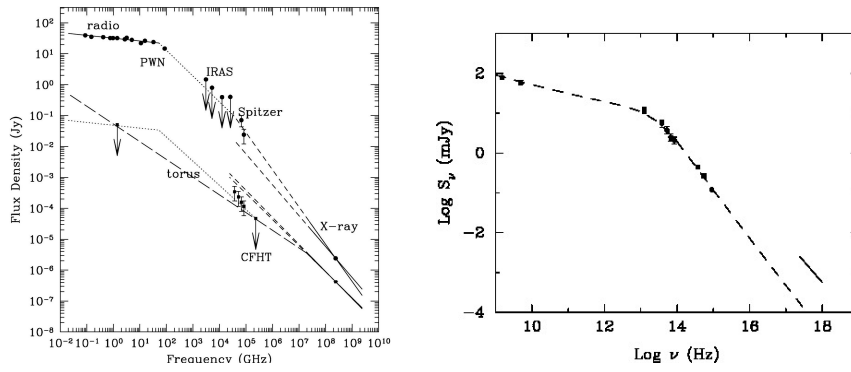


Fig. 6 Left: SED of 3C 58 (Slane et al. 2008). The spatially integrated spectrum is above, and is roughly describable by two power-laws of slopes α of 0.1 and ~ 1 , with a break near 100 GHz. (The small-scale torus requires a considerably more complex spectrum.) Right: SED of B0540-693 in the Large Magellanic Cloud (Williams et al. 2008). Triangles are *Spitzer* observations. The solid line is the *Chandra* spectrum (Kaaret et al. 2001), which is affected by pileup in the pulsar. The PWN X-ray spectrum does not appear to be consistent with the power-law extrapolation from the optical-IR (Serafimovich et al. 2004).

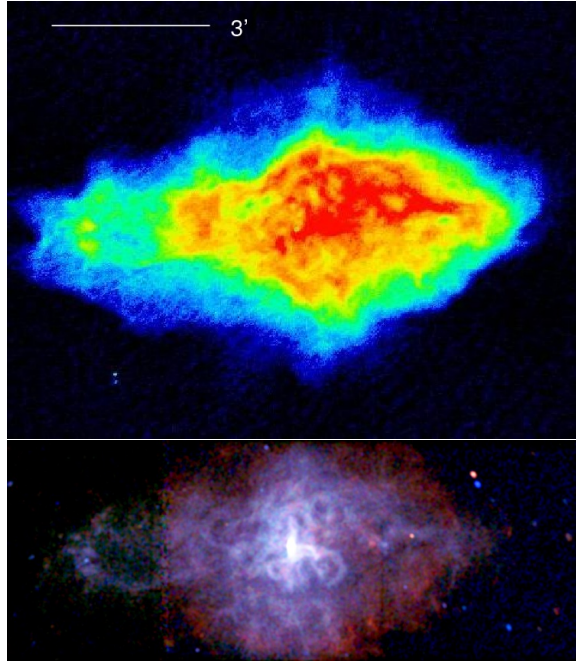


Fig. 7 Top: VLA image of 3C 58 at 1.4 GHz (Reynolds and Aller 1988). Bottom: *Chandra* X-rays (Slane et al. 2008). Note the close correspondence between detailed features, and the similar maximum extent in radio and X-rays.

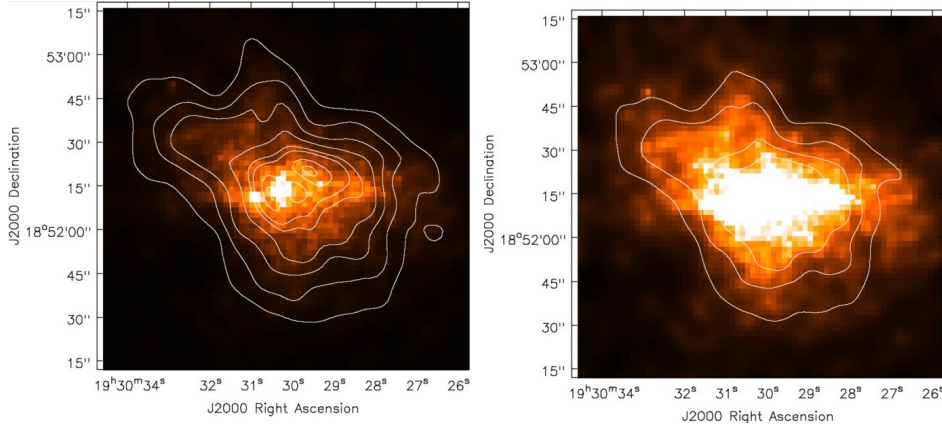


Fig. 8 Images of G54.1+0.3 in radio (contours; VLA at 4.7 GHz) and X-ray (*Chandra*), with two different stretches to emphasize the extent of faint X-ray emission (Lang et al. 2010).

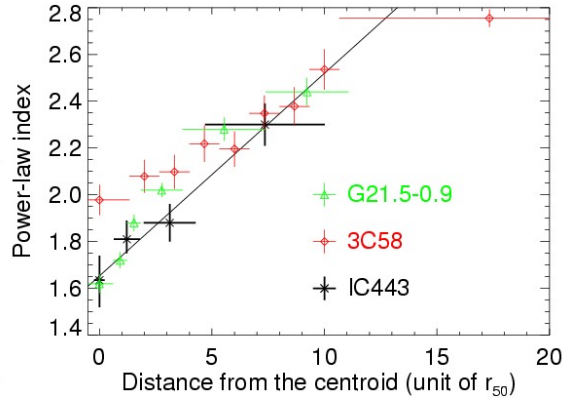


Fig. 9 Steepening of the X-ray spectrum with scaled distance from the center, for three PWNe (Bocchino and Bykov 2001). The distance is in units of the distance at which the surface brightness has dropped a factor of 2 below its peak. The line is a straight-line fit to the IC 443 data only.

10 keV was not available. However, the *NuSTAR* mission, launched in 2012 (Harrison et al. 2013), has brought that capability to the study of PWNe. Results of observations of three PWNe with *NuSTAR* are summarized below; details are in the primary publications listed.

2.2.1 Crab Nebula

For PWNe with a bright pulsar, disentangling the PWN emission from the pulsar, and then searching for spectral variations, requires good resolution in both time and space. Madsen et al. (2015) describe this process in detail for the Crab. The observations were divided into 13 phase intervals of the pulsar rotation period, and only bins 10 – 12, where pulsar emission was negligible, were used for the PWN spatial/spectral analysis (see Figs. 10 and 11). The spatially and temporally integrated signal was calibrated to the accepted power-law shape with $\Gamma = 2.1$ [$F(E) \propto E^{-\Gamma}$ photons $\text{cm}^{-2} \text{s}^{-1} \text{keV}^{-1}$]. But the spectrum is substantially harder at smaller radii. This was known previously through *Chandra* observations (Mori

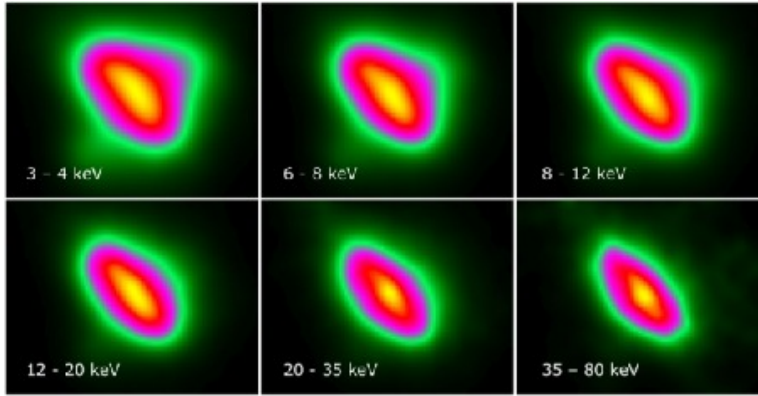


Fig. 10 The Crab Nebula with *NuSTAR* (Madsen et al. 2015), after maximum-entropy deconvolution. The nebula shrinks with increasing photon energy, at different rates in different directions.

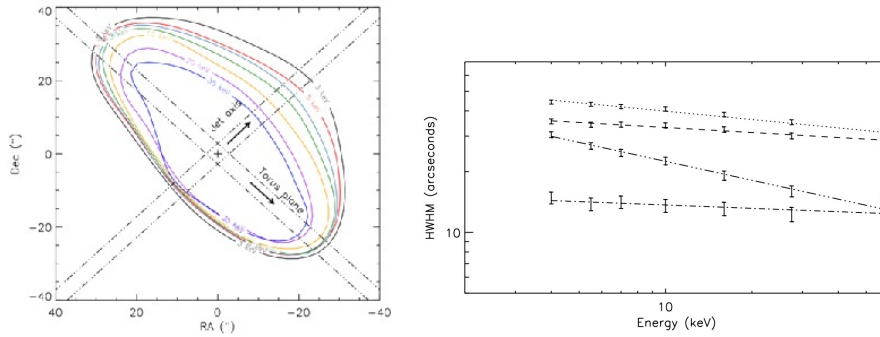


Fig. 11 Left: Crab 50% peak intensity contours at different energies (Madsen et al. 2015). From outside in, 3 – 5, 5 – 6, 6 – 8, 8 – 12, 12 – 20, 20 – 35, and 35 – 78 keV. Right: Fits to the HWHM along different directions. From top to bottom: NE torus plane, SW torus plane, NW jet axis, and SE jet axis.

et al. 2004). However, *NuSTAR* has revealed another important feature: the spectrum of the inner nebula (primarily the torus) appears to steepen by a substantial amount, $\Delta\Gamma \cong 0.25$, above a break energy of about 9 keV. Fig. 12 shows the low and high-energy Γ values, based on the *NuSTAR* data.

The original spherical, steady-state MHD model of Kennel and Coroniti (1984a,b) predicted how the size of the Crab Nebula in the X-ray range should scale with photon energy E : $R \propto E^m$ with $m = -1/9$. This prediction was consistent with results found by several sounding-rocket measurements with lunar occultations in the 1970’s (Kestenbaum et al. 1975; Ku et al. 1976) which obtained $\text{FWHM} \propto E^{-0.148 \pm 0.012}$, fitting Gaussians to the data. This result was regarded as adequate agreement. The *NuSTAR* data show that the shrinkage is spatially varying (Figs. 10 and 11). The fitted values of m are -0.086 ± 0.025 along the NE direction and -0.073 ± 0.028 along the SW, or about -0.08 ± 0.03 along the torus plane. For the SE, m is consistent with zero, but along the NW (“counter-jet” direction), the rate is substantially larger: $m = -0.218 \pm 0.040$. The torus rate is consistent with the Kennel and Coroniti (1984a,b) prediction, but the counter-jet clearly shrinks much more rapidly.

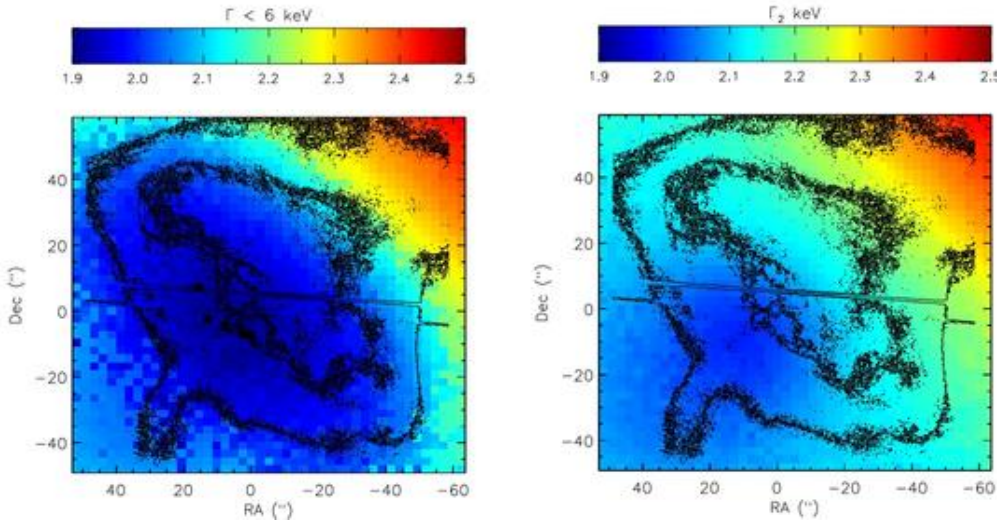


Fig. 12 Left: Crab photon index Γ below 6 keV; right: Γ above 10 keV (Madsen et al. 2015). Contours are from *Chandra* (Mori et al. 2004).

2.2.2 G21.5–0.9

This bright PWN was used for calibration by *NuSTAR* and other missions. It has been reported as a TeV source (Djannati-Ataï et al. 2008, see Fig. 15); while those data appear to lie roughly on an extrapolation from the measurements of *NuSTAR* and INTEGRAL, the TeV emission must be due to a separate process as normal synchrotron emission is limited to photon energies below a few hundred MeV. However, the radio – X-ray spectrum appears to be reasonably well described by two power-laws, requiring a steepening in mid-IR by $\Delta \equiv \alpha(\text{high}) - \alpha(\text{low}) \sim 1.0$, where $\alpha(\text{high})$ is the X-ray energy index ($\alpha_X \equiv \Gamma - 1$).

The fairly symmetric appearance of G21.5–0.9, and its similar size and morphology in radio, IR, and X-rays, are unusual for PWNe. Fig. 13 shows that the PWN sits in the center of an apparent shell of diffuse X-rays. This diffuse emission shows some apparent limb-brightening in the SE and irregular structures to the N which have thermal spectra and appear to be the SNR shell (Bocchino 2005), but there is also a substantial X-ray halo due to scattering by interstellar dust providing the symmetric component of diffuse emission that drops with radius (Bandiera and Bocchino 2004).

NuSTAR observations (Nynka et al. 2014) show substantial shrinkage with X-ray energy (Fig. 14, though the FWHM shrinkage is less dramatic than the drop in total flux). Fig. 15 shows the FWHM shrinkage, well described by a power-law with $m = -0.21 \pm 0.01$, similar to the value found for the Crab counter-jet. The northern part of the shell is detectable in the images to at least 20 keV, suggesting that part of the emission may be nonthermal. The *NuSTAR* spectrum shows, as for the Crab torus, a spectral softening that can be fit with a broken power-law, with Γ steepening from 1.996 ± 0.013 below a break energy $E_b = 9.7^{+1.2}_{-1.4}$ keV to 2.093 ± 0.013 above that energy. (Dust scattering efficiency drops with increasing photon energy and should not affect the spectrum in the *NuSTAR* energy range above 3 keV.)

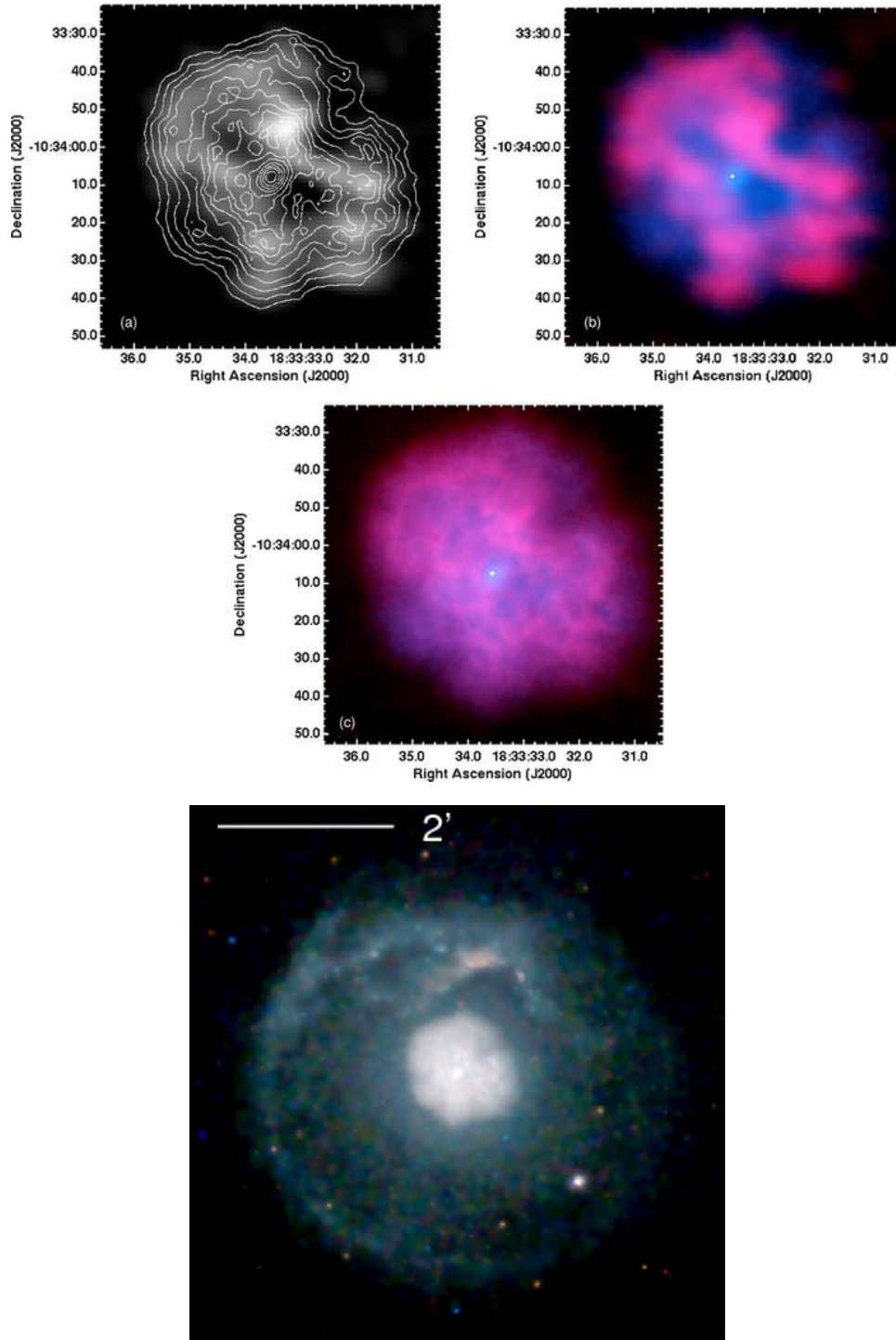


Fig. 13 G21.5-0.9 in radio and X-rays (Matheson and Safi-Harb 2010). Upper left: radio (greyscale; 22.3 GHz from the Nobeyama Millimeter-Wave Array, resolution $8''$ (Fuerst et al. 1988) and X-rays (*Chandra* contours; Matheson and Safi-Harb 2010). Upper right: 22.3 GHz data in red, *Chandra* in blue. Center: 4.75 GHz radio (VLA; Bietenholz and Bartel 2008) in red, same X-rays in blue. Bottom: *Chandra* (Matheson and Safi-Harb 2010).

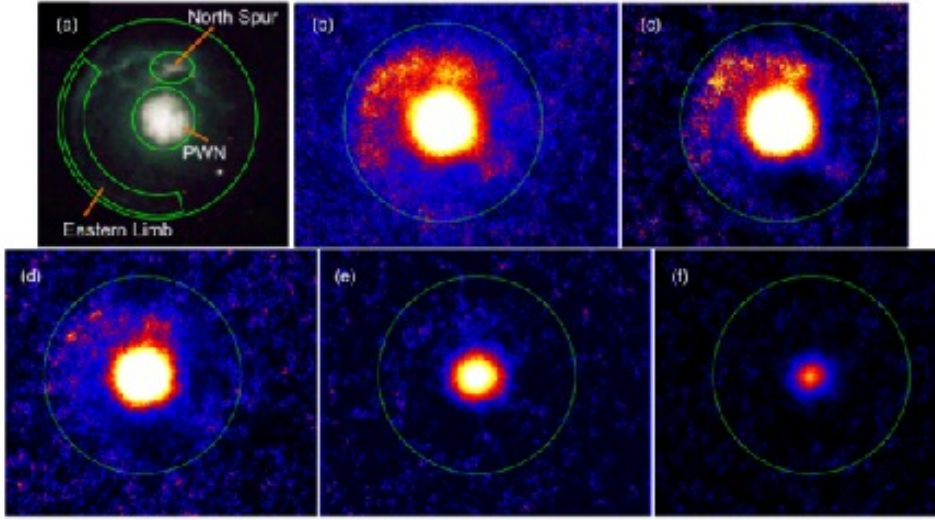


Fig. 14 (a): *Chandra* image of G21.5–0.9 between 3 and 6 keV (Matheson and Safi-Harb 2005). (b) – (f): Deconvolved *NuSTAR* images in various bands: (b) 3 – 6 keV; (c) 6 – 10 keV; (d) 10 – 15 keV; (e) 15 – 20 keV; and (f) 20 – 25 keV. The green circles in panels (b) through (f) have radii of $165''$.

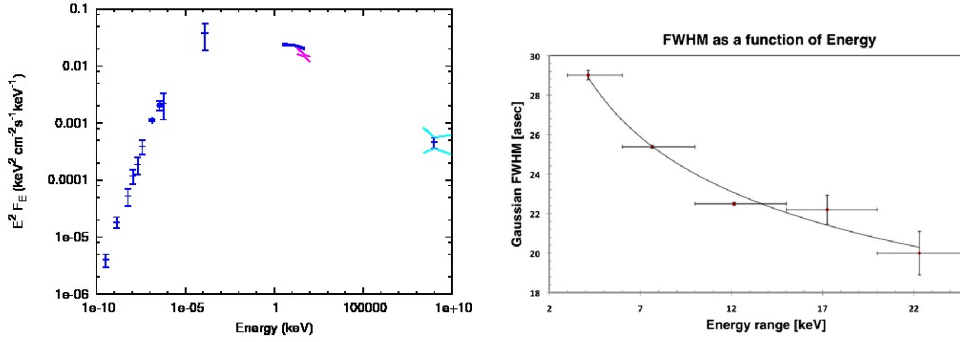


Fig. 15 Left: G21.5–0.9 SED (PWN only). Radio – mm points from Salter et al. (1989); IR point from Zajczyk et al. (2012); blue bowtie, *NuSTAR* (Nynka et al. 2014); magenta bowtie, INTEGRAL (de Rosa et al. 2009); TeV bowtie in cyan, H.E.S.S. (Djannati-Ataï et al. 2008). Right: Shrinkage of G21.5–0.9 with photon energy (Nynka et al. 2014).

2.2.3 MSH 15–52

This complex object has almost no radio counterpart (Gaensler et al. 2002), but is bright at X-ray wavelengths (Fig. 16). It contains a well-known 150 ms pulsar, PSR B1509-58, with a 1600-yr spindown timescale (Seward and Harnden 1982). A bright, curved jet extends to the SE, while long, straighter “fingers” reach to the NW to an H II region, RCW89, which contains small knots of radio and X-ray emission. A TeV detection has been reported (Aharonian et al. 2005). The full SED is shown in Fig. 17.

NuSTAR observations (An et al. 2014) show the same progressive steepening evident in other PWNe. Combined fitting with *Chandra* and *NuSTAR* gives a rate that appears to slow with distance, and can be described by two power-laws (Fig. 18). This steepening is

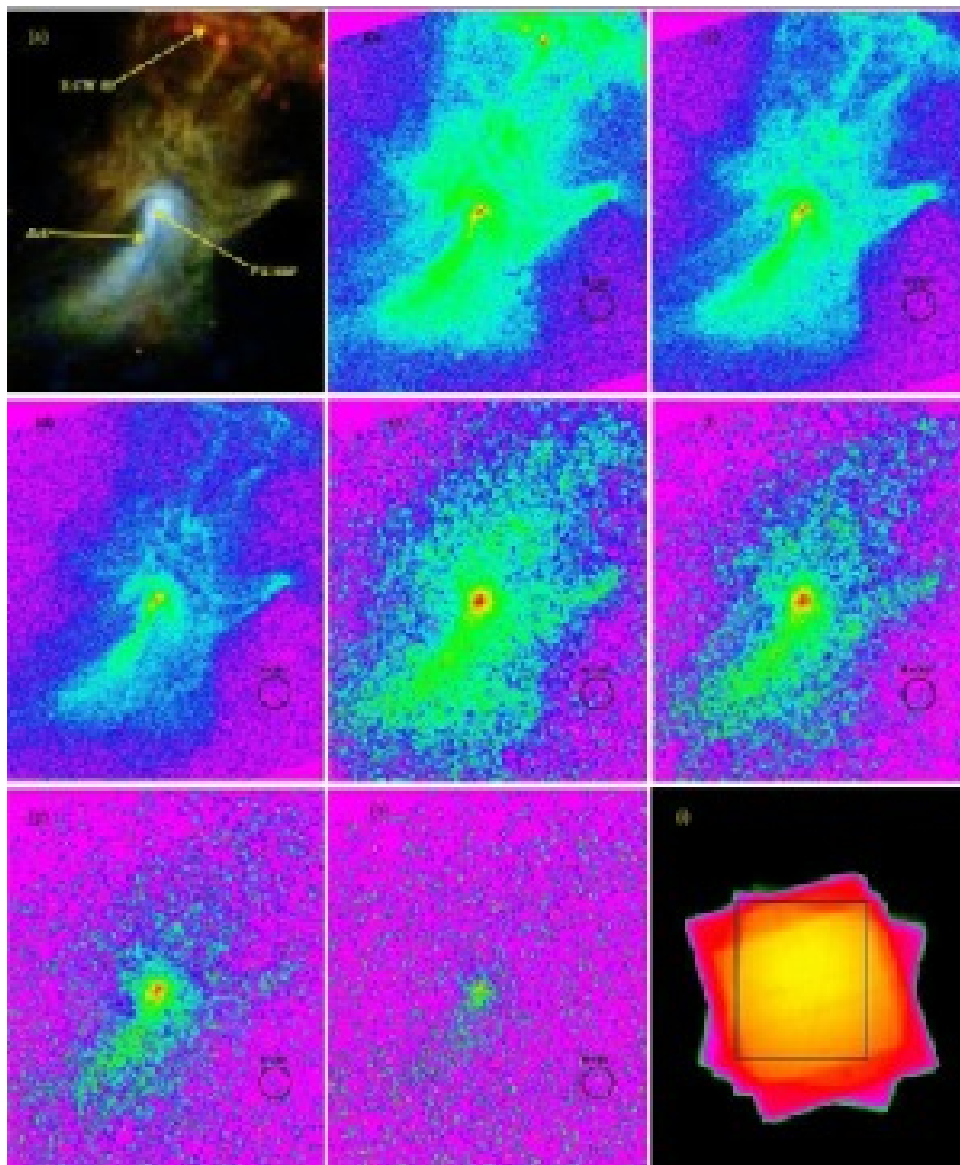


Fig. 16 MSH 15–52 with *Chandra* and *NuSTAR* (An et al. 2014). From left to right, top to bottom: *Chandra*+*NuSTAR*, 0.5 – 40 keV; *Chandra*, 0.5 – 2 keV; *Chandra*, 2 – 4 keV; *Chandra*, 4 – 7 keV; *NuSTAR*, 3 – 7 keV; *NuSTAR*, 7 – 12 keV; *NuSTAR*, 12 – 25 keV; *NuSTAR*, 25 – 40 keV; *NuSTAR* exposure map. All frames except the last are $10' \times 12'$.

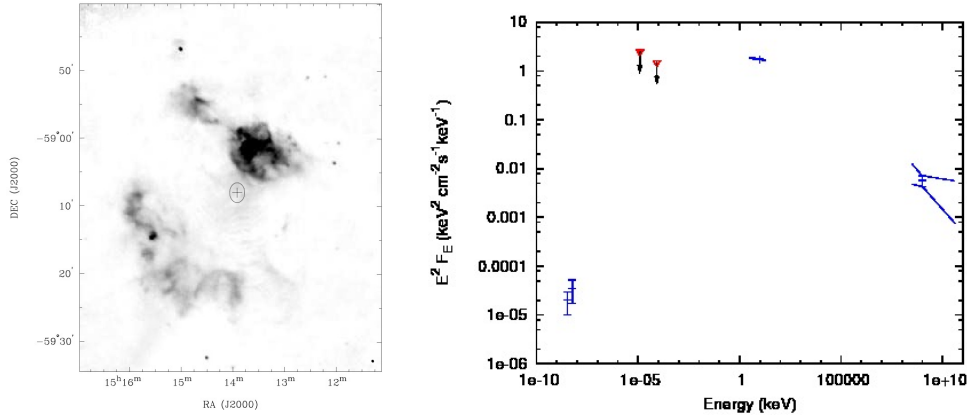


Fig. 17 Left: Radio image of MSH 15–52 at 1.3 GHz with ATCA (Gaensler et al. 1999). The bright horse-shoe to the N is RCW 89. There is little evidence of the PWN; the cross marks the pulsar location. Right: SED for MSH 15–52. Radio: Gaensler et al. (2002). IR upper limits are from Koo et al. (2011). X-rays: An et al. (2014). TeV: Aharonian et al. (2005).

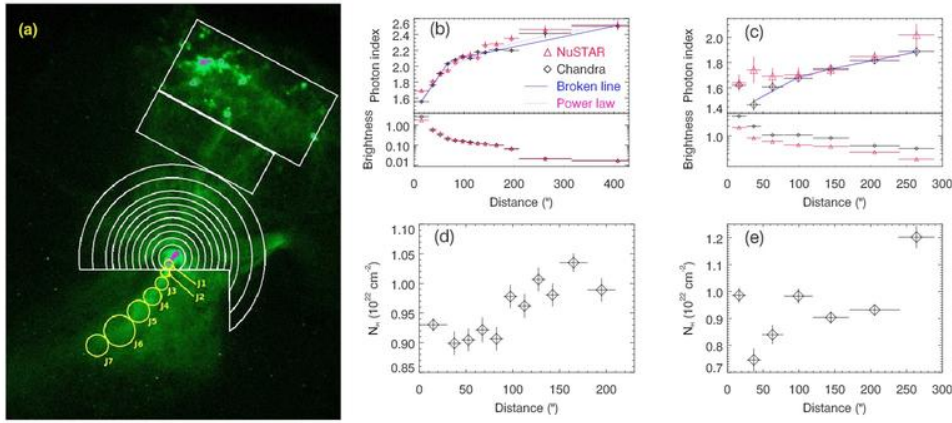


Fig. 18 Left (panel (a)): Regions of MSH 15–52 used for spatially resolved spectroscopy. Panel (b): Photon index as a function of distance to the NW (in the partial annuli). Panel (c): Photon index along the jet to the SE. Panels (d) and (e) give fitted column densities N_H from *Chandra* data as a function of distance from the pulsar, for the northern nebula and the jet, respectively. Figures from An et al. (2014).

reflected in the broader measure of source extent as a function of photon energy (Fig. 19). Profiles were created by summing transversely in a rectangular box of width $100''$ extended along the jet axis. Again, combined data from *Chandra* and *NuSTAR* were used. Power-laws describe the data fairly well, with $m \sim -0.2$ (Fig. 19), a value similar to that found for G21.5–0.9 and for the counterjet of the Crab.

2.3 Spectral breaks in PWNe

The integrated synchrotron spectrum of all known PWNe steepens sharply between radio and X-rays. Steepening due to radiative losses is expected, but steepening can also be caused

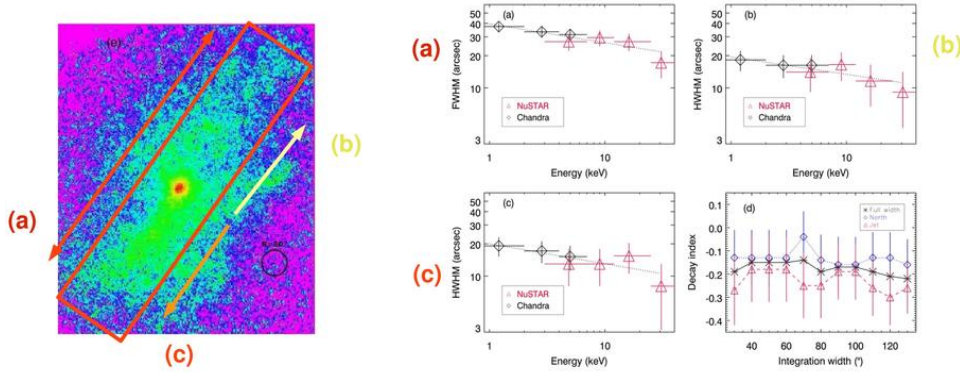


Fig. 19 Left: Box used to extract profiles from *NuSTAR* image of MSH 15–52. Profiles were summed along the minor dimension ($100''$), and extents as a function of energy displayed in panels to the right. Panel (a): FWHM of profiles centered on the pulsar extending in both directions. (b): Extending from the pulsar to the NW. (c) Extending from the pulsar to the SE (along the jet). (d) Energy shrinkage (“decay”) indices m (with extents $\propto E^m$). Plots from An et al. (2014).

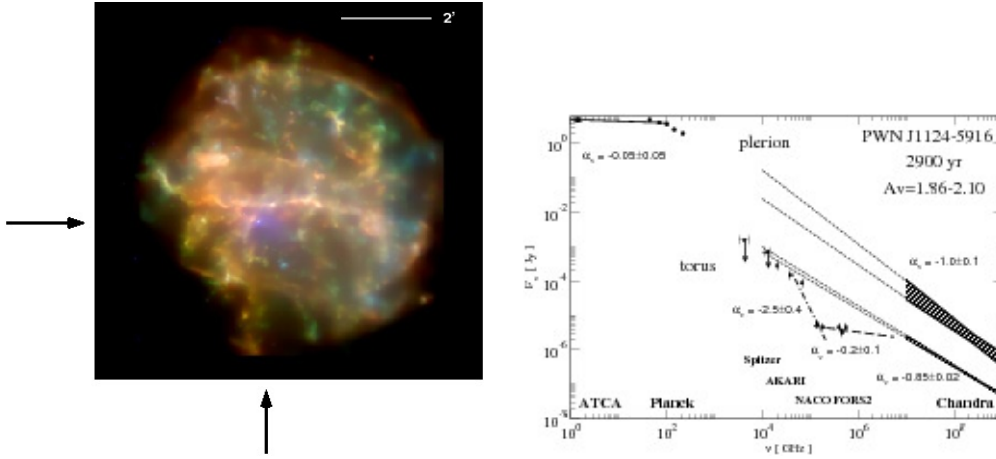


Fig. 20 Left: The shell SNR G292.0+1.8, with the pulsar indicated and the PWN in blue (Park et al. 2007). Right: SEDs of the entire PWN and of the torus [seen in VLT images at H and K_s bands; Zharikov et al. (2013)]. The torus spectrum is complex, but the PWN could be described by a double power-law with a single spectral break around 100 GHz. However, the steepening Δ is almost 1.

by evolutionary effects, such as the dropoff of pulsar luminosity after a few hundred years (e.g., Pacini and Salvati 1973), or by intrinsic structure in the spectrum of particles injected into the nebula at the wind termination shock. It is important to be able to characterize the injected spectrum to understand the physics of particle acceleration, so determining the cause of spectral structure is a necessary part of using PWNe as laboratories for the study of astrophysical particle energization.

While the small-scale torus of a PWN often has a complex, non-monotonic SED (see, for example, Figs. 6 and 20 for the cases of 3C 58 and G292.0+1.8), the larger-scale PWN often has simpler spectral behavior. The spectrum of an initially straight power-law distribution of electrons subject to synchrotron losses steepens at an energy at which the source age

Table 2 Spectral breaks in PWNe

Object	α_{radio}	$\alpha_{\text{X-ray}}$	Δ	Reference
Crab	0.3	1.1	0.8	Manchester et al. (1993)
G11.2−0.3	~ 0	0.9	0.9	Roberts et al. (2003)
Kes 75	0.2	0.9	0.7	Blanton and Helfand (1996)
G54.1+0.3	0.28	0.8	0.5	Lu et al. (2002)
3C 58	0.1	1.1	1.0	Green and Scheuer (1992)
B0540−693	0.25	1.2	0.95	Manchester et al. (1993)
G21.5−0.9	~ 0	1.0	1.0	Salter et al. (1989), Nynka et al. (2014)
MSH 15−52	0.2	1.1	0.9	Gaensler et al. (2002)
G292.0+1.8	0.05	0.9	0.85	Gaensler and Wallace (2003)

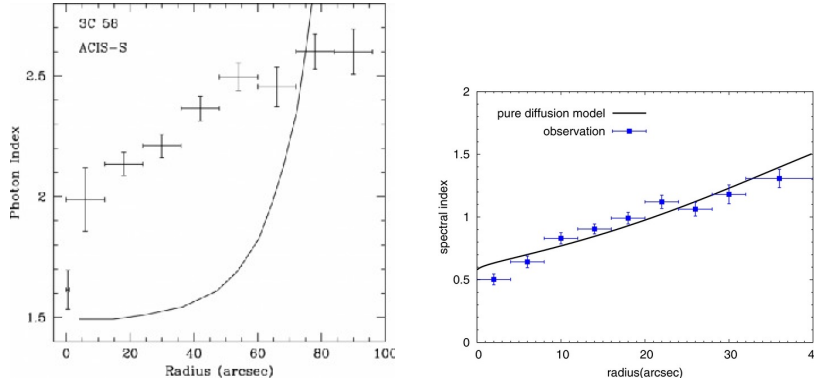


Fig. 21 Left: Observed photon index Γ as a function of radius in 3C 58 (Slane et al. 2004). Curve: Prediction from Kennel-Coroniti pure-MHD spherical advection model (Reynolds 2003). Right: Diffusion model for G21.5−0.9 (Tang and Chevalier 2012, data from Slane et al. (2000)).

equals the synchrotron-loss time (Kardashev 1962). The amount of spectral steepening $\Delta \equiv \alpha(\text{high}) - \alpha(\text{low})$ is 0.5 in the case of a uniform source with constant particle injection, but for inhomogeneous sources, naturally arising from outflow, Δ can differ from 0.5 (Kennel and Coroniti 1984b; Reynolds 2009). Since $\Delta > 0.5$ is far more common than $\Delta = 0.5$ (see Table 2, and Fig. 6 for the examples of 3C58 and 0540−693, both with $\Delta \sim 1$), either these breaks are not due to losses (in which case the absence of loss breaks poses serious modeling problems), or PWNe are significantly inhomogeneous. Outflow models, however, predict spatial dependence of steepening which is at odds with observations (uniform spectra until sudden steepening near the edge, clearly at variance with observed behaviors, e.g., Figs. 9 and 18).

Simple PWN models offer two possibilities for spectral steepening, both based on radiative losses of electrons, but invoking different pictures of particle transport from the wind shock through the nebula. In pure-advection models like those of Kennel and Coroniti (1984a) and Reynolds (2009), steepening can be thought of as due to the shrinkage of effective source size with increasing photon energy, as energy losses deplete electrons with higher energies at smaller radii. However, such models all share one important failing: they predict that the PWN spectral index should be constant throughout the source until a sudden steepening at the (energy-dependent) edge radius (Fig. 21).

However, advection models in inhomogeneous sources can produce the frequently observed steepenings by values Δ greater than 0.5. The models can be tested because they

achieve such values of Δ by source shrinkage at related rates; that is, the source size R obeys $R \propto E^m$ with m and Δ related by the model. The Kennel-Coroniti model predicts $\Delta = (4 + \alpha)/9$, where $\alpha = 0.6$ characterizes the assumed injected spectrum, explaining optical and higher-energy emission. A triumph of this model was the successful explanation ($m = -1/9$) of the rocket observations of the Crab in the 1970's, as described above.

More extreme source gradients are required to produce Δ significantly in excess of 0.5, however. Reynolds (2009) considered ad-hoc source gradients in flow-tube radius, magnetic field, density, and velocity, and connected them to predicted values of Δ . The large parameter space is significantly constrained if the source shrinkage with size can actually be measured. If magnetic-field strength varies as r^{m_B} and density as r^{m_ρ} , conical flows (jets or spherical winds) with $\alpha = 0$ (for simplicity) satisfy

$$\frac{\Delta}{-m} = 3 + m_B + m_\rho. \quad (1)$$

For G21.5–0.9, $\Delta/(-m) = 4.29$ so $m_B + m_\rho = 1.3$, requiring that either magnetic field B or gas density ρ , or both, *rise* with radius. This could conceivably happen due to turbulent amplification of magnetic field and/or mass loading of the PWN outflow (Lyutikov 2003), but seems unlikely. A similar result holds for MSH 15–52, requiring $m_B + m_\rho \sim 1$. While a value for m can be determined for the Crab's counter-jet, an independent value of Δ for that region alone is difficult to obtain, since that feature is embedded in the radio nebula and is not morphologically distinct.

Alternatively, particle transport may occur through diffusion. Purely diffusive models (Gratton 1972; Reynolds and Jones 1991; Tang and Chevalier 2012) can produce fairly linear increases in spectral index with radius (Fig. 21). However, they do not predict a change of source size with photon energy, and the spectral breaks must be intrinsic. Combination models of diffusion and advection (Tang and Chevalier 2012) offer more flexibility, but are not amenable to analytic investigation and have not yet been explored in great detail. These models all remain quite simple, with spherical or simple one-dimensional outflow geometries. The gradual increase of spectral index with radius probably requires a mix of particles of different ages at each radius; such a mix can be achieved by diffusion, but also by more complicated flow geometries, such as the backflows found in relativistic-MHD simulations such as those of Komissarov and Lyubarsky (2004) or Del Zanna et al. (2004).

The question of the origin of the full SED of the synchrotron spectrum from PWNe is thus still unsettled, so the observations cannot yet be brought to bear directly on theories of particle energization in PWNe. Even the fundamental origin of the radio-emitting particles is still mysterious. Relativistic-MHD simulations still lack the ability to make detailed spectral predictions, as these require propagating the full particle spectrum with each fluid element, and are computationally prohibitive at this time. It is most likely, however, that further progress will require the development of this capability. In the meantime, the observational characterization of PWN SEDs and spatially resolved spectra remain important tools for constraining models, and may ultimately contribute essential clues to solutions of these basic problems.

All three PWNe observed with *NuSTAR* have been detected at TeV wavelengths. Gamma-ray observations hold out the promise of further constraining the particle distributions of PWNe known at other wavelengths, but also of discovering new types of object that are predominantly TeV emitters. Both cases are discussed in Section 4.

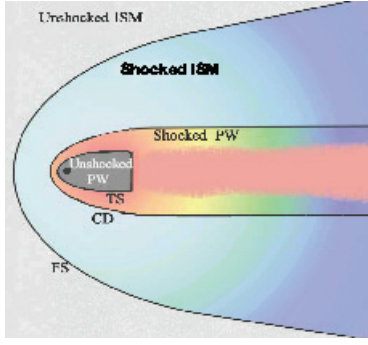


Fig. 22 Cartoon of a head-tail PWN created by a supersonically moving pulsar. A synchrotron (e.g., X-ray) PWN is produced by the shocked PW flowing between the TS and CD surfaces, while the shocked circumstellar medium between the FS and CD surfaces is expected to be the source of IR-optical-UV radiation.

3 X-ray pulsar wind nebulae outside supernova remnants

3.1 Expected general properties of PWNe of supersonically moving pulsars

For the first 500–1000 years after the SN explosion, the SNR’s radius R_{SNR} almost linearly increases with time with a typical speed of $\sim 10,000 \text{ km s}^{-1}$, much faster than the typical pulsar speed of a few hundred km s^{-1} . At larger ages the SNR expansion slows down ($R_{\text{SNR}} \propto t^{2/5}$ and $t^{3/10}$ in the Sedov and pressure-driven snowplow stages, respectively), while the pulsar keeps moving with about the same velocity and eventually leaves the SNR at an age of ~ 20 –200 kyr (see Fig. 4 in Arzoumanian et al. 2002). This means that most of the known pulsars are moving in the ISM with the speed V_{psr} considerably exceeding the speed of sound in the ambient medium, $c_s = (\gamma_{\text{ad}} kT / \mu m_{\text{H}})^{1/2} \sim 3$ –30 km s^{-1} , where γ_{ad} is the adiabatic index ($\gamma_{\text{ad}} = 5/3$ for monoatomic gases), T is the temperature, and μ is the molecular weight. The supersonic motion of the pulsar drastically changes the PWN morphology (see van der Swaluw et al. 2004, Gaensler and Slane 2006, and references therein). Since the ram pressure $p_{\text{ram}} = \rho_{\text{amb}} V_{\text{psr}}^2 = 1.5 \times 10^{-9} n_b (V_{\text{psr}} / 300 \text{ km s}^{-1})^2 \text{ dyn cm}^{-2}$ (where n_b is the ambient baryon number density in units of cm^{-3}) exceeds the ambient pressure p_{amb} ,

$$p_{\text{ram}} / p_{\text{amb}} = \gamma_{\text{ad}} \mathcal{M}^2 \gg 1, \quad (2)$$

($\mathcal{M} = V_{\text{psr}} / c_s$ is the Mach number), the PWN acquires a cometary shape with a compact head around the pulsar and a long tail behind it (Figure 22). In an idealized picture, the interaction of the pulsar wind (PW) with the ambient (circumpulsar) medium creates three distinct regions. The bullet-shaped cavity around the pulsar is filled with the *unshocked relativistic PW* confined within the termination shock (TS). The *shocked PW*, which is the main source of synchrotron radiation in X-rays, is flowing away between the TS and the contact discontinuity (CD) that separates the shocked PW from the shocked ambient medium. Finally, the compressed and heated *shocked ambient medium* between the CD and the forward bow shock (FS) is expected to emit IR-optical-UV radiation in spectral lines and continuum.

For an isotropic pulsar wind, a characteristic distance from the pulsar at which the ram pressure of the unshocked PW, $\dot{E}_w / (4\pi cr^2)$, balances the ram pressure of the ambient medium (the so-called stagnation point) is

$$R_0 = \left(\frac{\dot{E}_w}{4\pi c p_{\text{ram}}} \right)^{1/2} = 1.3 \times 10^{16} \dot{E}_{w,35}^{1/2} n_b^{-1/2} (V_{\text{psr}} / 300 \text{ km s}^{-1})^{-1} \text{ cm}, \quad (3)$$

where $\dot{E}_w = \xi_w \dot{E} = 10^{35} \dot{E}_{w,35} \text{ erg s}^{-1}$, \dot{E} is the pulsar’s spin-down power, and $\xi_w < 1$ is the fraction of \dot{E} that powers the PW. For an unmagnetized PW, R_0 is approximately equal to

the distance of the CD apex ahead of the pulsar, $R_{\text{cd}} \approx R_0$ (van der Swaluw et al. 2004). The characteristic angular separation between the pulsar and the sky projection of the CD surface is

$$\theta_0 \approx R_0/d = 0''.89 d_{1.0}^{-1} \dot{E}_{w,35}^{1/2} n_b^{-1/2} (V_{\perp}/300 \text{ km s}^{-1})^{-1} \sin i, \quad (4)$$

where $d = 1.0 d_{1.0}$ kpc is the distance¹, i is the angle between the line of sight and the pulsar velocity², and $V_{\perp} = V_{\text{psr}} \sin i$. The small value of θ_0 implies that subarcsecond resolution (provided only by *Chandra* among the currently active X-ray observatories) is required to resolve the PWN head from the pulsar even for nearby pulsars.

The unshocked PW consists of relativistic particles (likely electrons and positrons) and a magnetic field. The magnetization parameter σ , defined as the ratio of the Poynting flux, $B^2 c / (4\pi)$, to the particle enthalpy flux, is unknown. Pulsar models predict $\sigma \gg 1$ immediately outside the pulsar magnetosphere, while PWN models require $\sigma \lesssim 1$ (or even $\sigma \ll 1$; Kennel and Coroniti 1984a) just upstream of the TS. The decrease of σ with distance from the pulsar could be due to transfer of the magnetic field energy to the particles, e.g., by magnetic field reconnection in the striped PW (see Kirk et al. 2009, and references therein). For a given magnetization, the magnetic field upstream of the TS at the stagnation point can be estimated as

$$B \sim \left[\frac{\dot{E}_w \sigma}{c R_0^2 (\sigma + 1)} \right]^{1/2} = \left(\frac{4\pi p_{\text{ram}} \sigma}{\sigma + 1} \right)^{1/2} \approx 140 \left(\frac{n_b \sigma}{\sigma + 1} \right)^{1/2} \frac{V_{\text{psr}}}{300 \text{ km s}^{-1}} \mu\text{G}. \quad (5)$$

The magnetic field can be somewhat higher in the shocked PW, up to a factor of 3 immediately downstream of TS, at $\sigma \ll 1$ (Kennel and Coroniti 1984a). Thus, characteristic PWN magnetic field values are expected to be of the order of 10–100 μG .

Typical energies of synchrotron photons emitted in such fields can be estimated as

$$E = \zeta \frac{h e B_{\perp} \gamma^2}{2\pi m_e c} = 1.16 \zeta B_{-5} \gamma_8^2 \text{ keV} = 4.43 \eta B_{-5} (E_e/100 \text{ TeV})^2 \text{ keV} \quad (6)$$

where $B_{\perp} = 10^{-5} B_{-5}$ G is the magnetic field component perpendicular to the electron velocity, $\gamma = E_e/(m_e c^2) = 10^8 \gamma_8$ is the electron Lorentz factor, and $\zeta \sim 1$ is a numerical factor. The synchrotron emission spectrum is determined by the electron spectrum, which depends on the still poorly understood acceleration mechanism. The commonly considered Fermi acceleration mechanism at fronts of relativistic shocks (e.g. the TS) gives a power-law (PL) electron spectrum, $dN_e/d\gamma \propto \gamma^{-p}$ in the range $\gamma_{\text{min}} < \gamma < \gamma_{\text{max}}$, with $p \gtrsim 2$ (see, e.g., Chapter 6 of the review by Bykov et al. 2012). Such an electron spectrum produces a PL photon spectrum, $dN/dE \propto E^{-\Gamma}$ in the $E_{\text{min}} < E < E_{\text{max}}$ range, with the photon index $\Gamma = (p + 1)/2 \gtrsim 1.5$. The maximum Lorentz factor of accelerated electrons³, $\gamma_{\text{max}} \lesssim (e/m_e c^2) [\dot{E} \sigma / c (\sigma + 1)]^{1/2} \approx 1.1 \times 10^9 \dot{E}_{35}^{1/2} [\sigma / (\sigma + 1)]^{1/2}$, can be estimated from the condition $R_g < R_0$, where $R_g = \gamma m_e c^2 / (eB) = 1.7 \times 10^{16} \gamma_8 B_{-5}^{-1} \text{ cm}$ is the gyration radius. This corresponds to the maximum synchrotron photon energy

$$E_{\text{max}} \lesssim 130 \zeta \dot{E}_{35} B_{-5} \sigma / (\sigma + 1) \text{ keV}. \quad (7)$$

¹In this Section the subscript of d means the scaling distance in kpc.

²Equation 4 is applicable at not too small $\sin i$; see Romani et al. (2010).

³Note that $\gamma_{\text{max}} m_e c^2 \sim e \Phi \sigma / (\sigma + 1)$, where $\Phi = B_{\text{LC}} R_{\text{LC}} \sim B_{\text{NS}} R_{\text{NS}}^3 \Omega^2 / c^2$ is the potential drop across the pulsar's polar cap, $R_{\text{LC}} = c/\Omega$ is the light cylinder radius, $\Omega = 2\pi/P$, B_{LC} and B_{NS} are the magnetic field values at the light cylinder and the neutron star surface. The maximum electron energies in other acceleration models (e.g., Romanova et al. 2005) are also fractions of $e\Phi$.

This equation shows that one should not expect X-ray PWNe from very old, low-power pulsars, but head-tail PWNe could be expected at UV-optical-IR wavelengths.

The qualitative head-tail PWN picture is generally confirmed by analytical estimates (e.g., Romanova et al. 2005) and numerical simulations. For instance, Bucciantini et al. (2005) presented relativistic MHD axisymmetric simulations for $\mathcal{M} = 30$ and three values of the PW magnetization σ upstream of the TS. Figure 1 of that paper shows that for an isotropic PW with a toroidal magnetic field the TS, CD and FS apices are at distances of $\approx R_0$, $1.3R_0$ and $1.7R_0$, respectively, at $\sigma = 0.002$, while the radius of the cylindrical tail (confined by the CD surface behind the pulsar) is $r_{\text{cd}} \approx 4R_0$, almost independent of magnetization. The bulk flow velocity in the tail reaches $0.8\text{--}0.9c$ at its periphery (closer to the CD), being $0.1\text{--}0.3c$ in the central channel (behind the TS bullet). Simulated maps of synchrotron brightness (Figures 4 and 5 in Bucciantini et al. 2005) show that the brightness is maximal at the PWN head, gradually decreasing with distance from the pulsar in the PWN tail.

The inner and outer channels of the tail flow should mix with each other at larger distances from the pulsar due to shear instability. At even larger distances the flow should slow down due to mass-loading of the ambient matter, which leads to additional tail broadening (e.g., Morlino et al. 2015).

As the outflowing electrons lose their energy to synchrotron radiation, we can expect spectral softening with increasing distance from the pulsar, which means the observed tail's length should increase with decreasing photon energy (e.g., it should be larger in the radio than in the X-rays). The length scale of the tail at photon energy E (in keV) can be estimated as

$$l_{\text{tail}} \sim V_{\text{flow}} \tau_{\text{syn}} \sim 18(V_{\text{flow}}/10,000 \text{ km s}^{-1}) \zeta^{1/2} E^{-1/2} B_{-5}^{-3/2} \text{ pc} \quad (8)$$

where V_{flow} is a typical flow velocity and $\tau_{\text{syn}} = 1.6\gamma_8^{-1} B_{-5}^{-2} \text{ kyr} \sim 1.7\zeta^{1/2} E^{-1/2} B_{-5}^{-3/2} \text{ kyr}$ is the synchrotron cooling time. We should note that such an estimate is very crude because both the flow velocity and the magnetic field vary with the distance from the pulsar.

The simulations by Bucciantini et al. (2005) were done for an isotropic PW. We, however, know that at least in some young pulsars the PW is mostly concentrated around the equatorial plane, perpendicular to the spin axis, and the PWN has equatorial and polar components (e.g., the torus and jets in the Crab pulsar; Weisskopf et al. 2000). In this case the ram pressure of the unshocked PW becomes anisotropic, which changes not only the distance to the stagnation point but also the overall PWN appearance. In particular, the PWN shape strongly depends on the angle between the pulsar's velocity and spin vectors, as well as on the angle between the spin vector and the line of sight. Three-dimensional simulations for several cases of anisotropic PW were presented by Vigelius et al. (2007), assuming nonrelativistic, unmagnetized flows (see also Wilkin 2000 and Romani et al. 2010 for analytical approximations). The PW anisotropy should strongly affect the shape of the PWN head, which may become substantially different from the bullet-like one. On the other hand, the shape of tail should not be so strongly affected, especially at large distances behind the pulsar.

In addition to synchrotron (and inverse Compton – see Section 4) emission from the shocked PW, one can expect emission from the shocked ISM between the FS and the CD. While passing through the FS, it is compressed and heated up to temperatures

$$T \approx (3/16)(\mu m_p/k)V_{\text{psr}}^2 = 1.2 \times 10^6 (\mu/0.6)(V_{\text{psr}}/300 \text{ km s}^{-1})^2 \text{ K}, \quad (9)$$

where μm_p is the mean mass per particle (including electrons; see Bykov et al. 2008 for details). The shocked ISM emits in both continuum and spectral lines in the optical, UV, and even soft X-ray ranges. If there are neutral hydrogen atoms in the ambient medium ahead

of the pulsar, they can be excited at the FS and emit spectral lines in the course of radiative de-excitation.

Thus, a rotation-powered pulsar that has left its parent SNR should be accompanied by a nebula that consists of a head-tail synchrotron component, emitting in a broad energy range, perhaps from the radio to soft γ -rays, enveloped by a (forward) bow-shock component observable in the optical-UV (particularly, in the Balmer lines). Below we will see, however, that observational results do not always coincide with the predictions of the current simple models.

3.2 Observational results

Although most of the known rotation-powered pulsars have left their SNRs and are moving with supersonic velocities, their spin-down powers (and the PWN luminosities) have significantly decreased with age. Therefore, the number of detected head-tail (bow-shock) PWNe is relatively small. Among over 70 PWNe and PWN candidates detected in X-rays (Kargaltsev et al. 2013), only about 15 PWNe are certainly created by old (and/or fast) enough pulsars that have left their parent SNRs. These have spin-down powers $0.01 \lesssim \dot{E}_{35} \lesssim 30$ and characteristic (spin-down) pulsar ages $\tau_{\text{sd}} \gtrsim 20$ kyr. Of the remainder, about 25 – 30 are still inside SNRs, and the rest are ambiguous, or not yet confirmed as PWNe. An even smaller number of head-tail PWNe were observed with exposures deep enough to accurately measure the X-ray PWN properties. Below we present a few examples of such observations.

3.2.1 *The Mouse: A textbook example?*

The Mouse PWN was discovered in a radio survey of the Galactic center region (Yusef-Zadeh and Bally 1987). The VLA image showed a bright compact head (“snout”), a bulbous $\sim 2'$ long “body”, and a remarkably long, $\sim 12'$, narrow “tail” (see the right panels in Figure 24). Camilo et al. (2002) discovered a 98 ms pulsar, J1747–2958, within the Mouse’s head, with a spin-down power $\dot{E} = 2.5 \times 10^{36} \text{ erg s}^{-1}$ and a characteristic age $\tau_{\text{sd}} = 25$ kyr. Hales et al. (2009) measured the proper motion of the radio PWN head⁴, $\mu = 12.9 \pm 1.8 \text{ mas yr}^{-1}$, which corresponds to a transverse velocity $V_{\perp} = (306 \pm 43)d_5 \text{ km s}^{-1}$, where $d_5 = d/5 \text{ kpc}$. Based on the projected tail length, $\sim 17d_5 \text{ pc}$, and the lack of an SNR that could possibly be associated with the pulsar (see, however, Yusef-Zadeh and Gaensler 2005), Hales et al. (2009) argue that the true age of the pulsar is $\gtrsim 160$ kyr.

The Mouse PWN was observed with *Chandra* by Gaensler et al. (2004) and Klingler et al. (2017, in preparation), with 36 ks and 120 ks exposures, respectively. These observations have shown an X-ray nebula with a compact bright head and a tail of $\sim 45''$ length, a factor of 16 shorter than the radio tail (see Figure 23). The X-ray luminosity of the PWN, $L_{0.5-8\text{keV}} \approx 3.3 \times 10^{34} d_5^2 \text{ erg s}^{-1}$, is about $0.013 d_5^2$ of the pulsar’s spin-down power, unusually high compared to other PWNe (Kargaltsev and Pavlov 2008). The distance from the pulsar to the projected leading edge of the head, $\theta_0 \approx 1''$, corresponds to $n_b \sim 0.8 \xi_w d_5^{-4} \sin^2 i \text{ cm}^{-3}$ (see Equation 4), typical for a warm phase of the ISM (e.g., Bykov et al. 2008). For a sound speed of $\sim 10 \text{ km s}^{-1}$, expected for this phase, the pulsar’s Mach number can be estimated as $\mathcal{M} \sim 30 d_5 / \sin i$. The spatially-resolved X-ray spectrum showed a significant increase of the photon index with increasing distance from the pulsar, from $\Gamma \approx 1.6$ in the

⁴It can differ from the pulsar’s proper motion if the pulsar moves in a non-uniform ambient medium, but we will neglect this difference here.

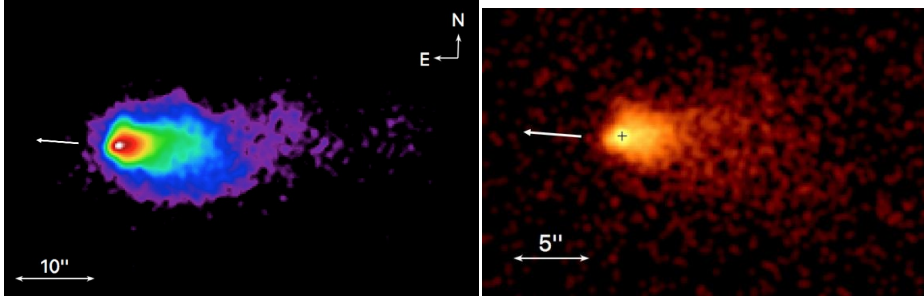


Fig. 23 Left: Merged image from 5 *Chandra* ACIS observations of the Mouse (0.5–8 keV, 154 ks exposure). Right: *Chandra* HRC image of the Mouse (58 ks exposure). The cross in the right image marks the pulsar position; the arrows show the direction of proper motion.

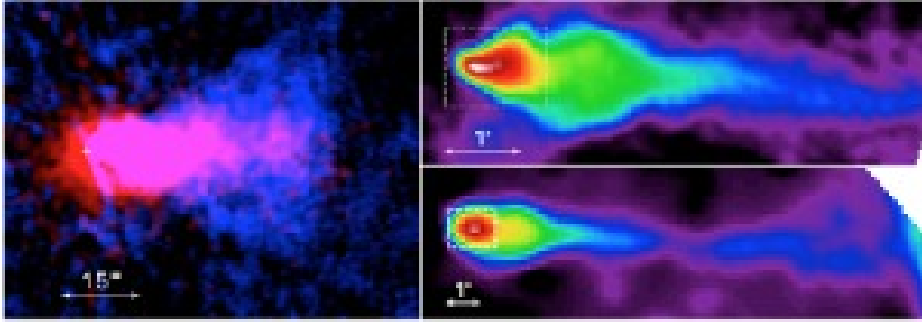


Fig. 24 Left: Composite X-ray (red; ACIS) and radio (blue; VLA, 1''.07 beam) image of the Mouse PWN. The pulsar position is shown by the white cross. Right: VLA radio images (top: 11'' beam, bottom: 32'' beam) showing the extended tail of the Mouse. The field of view of the left image is shown by the dashed white box in the lower right panel. The radio images were obtained from the NRAO VLA Archive.

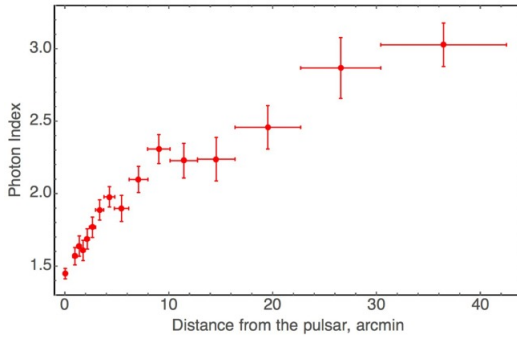


Fig. 25 Photon index Γ as a function of distance from the pulsar along the tail of the Mouse (Klingler et al. 2017, in preparation).

immediate vicinity of the pulsar to $\Gamma \approx 3.0$ at $\sim 40''$ from the pulsar (see Figure 25). The spectral softening could be caused by synchrotron cooling. Assuming equipartition between the magnetic field energy and the kinetic energy of relativistic electrons, the magnetic field strength estimated from the observed X-ray emission is a few hundred μG , substantially

higher than in other head-tail PWNe⁵. For such a magnetic field the projected length of the X-ray tail, $l_{\text{tail}} \sim 1 d_5$ kpc, corresponds to a flow velocity $V_{\text{flow}} \sim 20,000 B_{-4}^{3/2} d_5 / \sin i \text{ km s}^{-1}$, much higher than V_{psr} but significantly lower than the mildly relativistic speeds predicted by Bucciantini et al. (2005). Moreover, the comparison of the X-ray and high-resolution radio images (see the left panel of Figure 24) suggests that the flow is faster in the middle of the tail, contrary to the model predictions.

The radio tail of the Mouse is longer than in any other known PWN. Just behind the pulsar, the radio image looks like a cone with an $\approx 25^\circ$ half-opening angle (much broader than the Mach cone at the above-estimated $\mathcal{M} \sim 30$) and a vertex at the pulsar position. The cone abruptly narrows at $\sim 1'$ from the pulsar. Such behavior is not explained by the current PWN models. The Mouse is one of the few PWNe with a mapped radio polarization. Polarization measurements by Yusef-Zadeh and Gaensler (2005) suggest that the magnetic field wraps around the bow shock structure near the apex of the system, but runs parallel to the direction of the pulsar's motion in the tail behind the pulsar. Such a magnetic field distribution is different from the toroidal one assumed in the models by Bucciantini et al. (2005). Thus, the Mouse has a few features consistent with the model predictions, but the models do not fully agree with the observations, particularly in the radio.

3.2.2 Geminga: An odd “three-tail” PWN

The X-ray PWN created by the radio-quiet γ -ray pulsar Geminga ($P = 237$ ms, $\dot{E} = 3.3 \times 10^{34} \text{ erg s}^{-1}$, $\tau_{\text{sd}} = 340$ kyr, $d = 0.25_{-0.08}^{+0.23}$ kpc) looks quite different from the Mouse⁶ and from the predictions of PWN models. The proper motion of this pulsar, $\mu = 178.2 \pm 1.8 \text{ mas yr}^{-1}$ (Faherty et al. 2007), corresponds to the transverse velocity $V_{\perp} = (211 \pm 2) d_{0.25} \text{ km s}^{-1}$. Observations with *XMM-Newton* revealed two bent “tails” behind the pulsar, on both sides of its sky trajectory (Caraveo et al. 2003), while *Chandra* observations with higher spatial resolution showed a shorter third tail between the two lateral tails (Pavlov et al. 2006; Pavlov et al. 2010). The most detailed data on the Geminga PWN were provided by a series of 12 *Chandra* observations carried out in 2012–2013, with a total exposure of about 580 ks (Posselt et al. 2016). Figure 26 shows a summed image from these observations, where we see two lateral tails of $\sim 3'$ ($0.2 d_{0.25}$ pc) length and one $\sim 0.45''$ ($0.05 d_{0.25}$ pc) long central tail. Surprisingly, there is only a hint of bow-like emission ahead of the pulsar and no bright, filled ‘bullet’ predicted by the PWN models assuming an isotropic PW. The 0.3–8 keV luminosities of the northern and southern lateral tails, and the central tail are 1.6, 2.6, and $0.9 \times 10^{29} d_{0.25}^2 \text{ erg s}^{-1}$, respectively, i.e., the total PWN luminosity is a fraction of $1.5 \times 10^{-5} d_{0.25}^2$ of the pulsar's spin-down power, three orders of magnitude smaller than for the Mouse. Images from separate exposures show that the central tail is formed by isolated “blobs” seen at different distances from the pulsar in different observations (see Figure 27). However, there is no evidence of constant or decelerated motion of the blobs. The spectra of the lateral tails are very hard, $\Gamma \approx 0.7$ – 1.0 , much harder than the spectrum of the central tail, $\Gamma \approx 1.6$, and they do not show significant changes with increasing distance from the pulsar.

The nature of the three tails is not certain yet. One could assume that the lateral tails represent a limb-brightened paraboloid shell of shocked PW downstream of the TS and

⁵We should note, however, that such estimates assume that the magnetic field strength is about the same throughout the emitting volume, which may be far from reality.

⁶One should bear in mind, however, that much smaller spatial scales can be probed in the nearby Geminga PWN than in the Mouse.

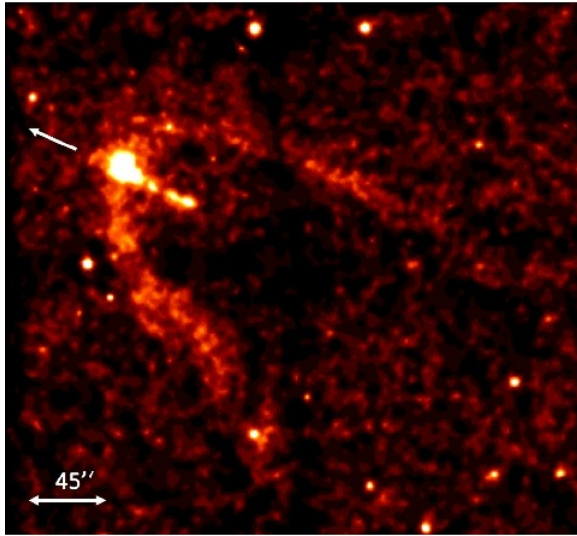


Fig. 26 Combined *Chandra* ACIS image of the Geminga PWN (0.5–8 keV, 540 ks). The arrow shows the direction of the pulsar's proper motion.

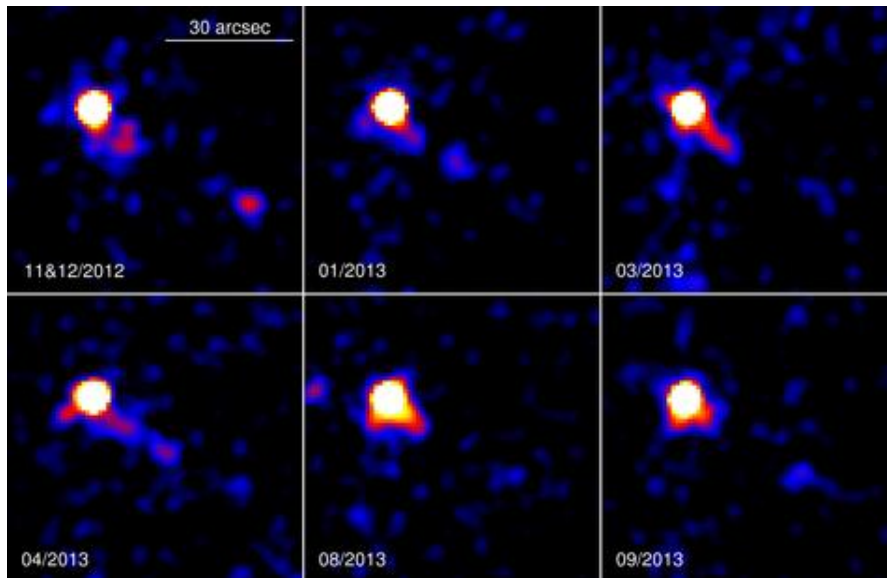


Fig. 27 Images of the central tail of the Geminga PWN in separate *Chandra* observations, in the 0.5–8 keV band.

their unusually hard spectrum is emitted by electrons accelerated by the Fermi mechanism at the shocks that form in two colliding flows (in the reference frame of CD) – the PW and the oncoming ambient medium. However, a lack of diffuse emission in between the lateral tails strongly suggests that the shell emissivity is not azimuthally symmetric with respect to the shell axis (i.e., the direction of motion). Such an asymmetry could be caused by a strong asymmetry of the PW (e.g., because the equatorial plane around the pulsar spin axis, where the PW is presumably concentrated, is strongly misaligned with the direction of motion) or an azimuthally asymmetric magnetic field in the shell (see Posselt et al. 2016

for details). Alternatively, the lateral tails could be interpreted as strongly collimated polar outflows (jets) bent by the ram pressure of the oncoming ambient medium. The blobs in the central tail could be short-lived plasmoids formed by magnetic field reconnection in the relativistic plasma behind the moving pulsar, resembling the magnetotails of the Solar system planets. Observations at different wavelengths could clarify the PWN nature, but the Geminga PWN was not detected in the radio or $H\alpha$. For any interpretation, we can conclude that the Geminga's PW is strongly anisotropic, and new models are required to explain the morphologies and spectra of such PWNe.

3.2.3 The Guitar: First example of a misaligned outflow

The Guitar nebula is produced by the relatively old, low-power pulsar B2224+65 ($P = 683$ ms, $\dot{E} = 1.2 \times 10^{33}$ erg s $^{-1}$, $\tau_{\text{sd}} = 1.12$ Myr). The pulsar is among the highest velocity neutron stars known; its proper motion, $\mu = 182 \pm 3$ mas yr $^{-1}$, corresponds to the transverse velocity $V_{\perp} = 860\text{--}1730$ km s $^{-1}$ (the uncertainty is caused by the uncertain distance, $d = 1\text{--}2$ kpc). The guitar-shaped $H\alpha$ nebula was discovered by Cordes et al. (1993) and further studied in several papers (see Dolch et al. 2016 and references therein). One could expect a head-tail X-ray PWN within the $H\alpha$ bow shock, but a high-resolution observation with *Chandra* showed instead a straight $2'$ ($0.3d_1$ pc) long feature inclined by 118° to the direction of the pulsar's proper motion (Wong et al. 2003; Hui and Becker 2007; see Figures 28 and 29). A second *Chandra* observation 6 years later showed that the sharp leading edge of the jet-like feature had the same proper motion as the pulsar, and it provided evidence for the presence of a counter-feature, albeit substantially shorter and fainter than the main one (Johnson and Wang 2010). The feature shows a power-law spectrum with $\Gamma \approx 1.6$, comparable to that of the point-like source (the pulsar plus an unresolved PWN?). The luminosity of the feature, $L_{0.3\text{--}7\text{keV}} \sim 7 \times 10^{30} d_1^2$ erg s $^{-1}$, exceeds that of the point-like source by a factor of 3–4, and is a fraction of $\sim 6 \times 10^{-3} d_1^2$ of the pulsar's spin-down power.

The lack of a resolved X-ray head-tail PWN could be explained by the very high pulsar velocity and low spin-down power. Indeed, according to Equation 3, the characteristic PWN size ahead of the pulsar, $R_0 \sim 5 \times 10^{14} \xi_w^{1/2} n_b^{-1/2} d_1^{-1}$ cm, corresponds to the angular distance⁷ as small as $\theta_0 \sim 0''.03 (\xi_w/n_b)^{1/2} d_1^{-2}$, much smaller than the angular resolution of *Chandra*. The lack (shortness) of the X-ray tail could be due to a high magnetic field (hence fast synchrotron cooling) in the shocked PW associated with the small stand-off distance (see Equation 5). Another reason could be a low maximum energy of accelerated electrons at the low spin-down power of B2224+65 (see Equation 7).

The nature of the elongated feature remains unclear. It might be a pulsar jet, but such a jet should be bent by the ram pressure of the oncoming ambient medium while no bending is observed. Bandiera (2008) suggested that the feature is produced by synchrotron radiation of highest energy electrons ($\gamma \sim 10^8$) accelerated at the TS and leaked into the ISM along its magnetic field. This scenario, however, requires a rather high ambient magnetic field ($\sim 45 \mu\text{G}$, according to Bandiera 2008) and it remains unclear why the counter-feature is so much fainter than the main one. Since the true nature of the feature is not certain yet, we will call it simply a *misaligned outflow*. It should be emphasized that, most likely, the misaligned outflow is not a (magneto)hydrodynamical flow but rather a stream of high-energy particles not interacting with each other and with the ISM gas.

⁷Chatterjee and Cordes (2002) estimated $\theta_0 = 0''.06 \pm 0''.02$ from modeling an $H\alpha$ image obtained with the *Hubble Space Telescope*.

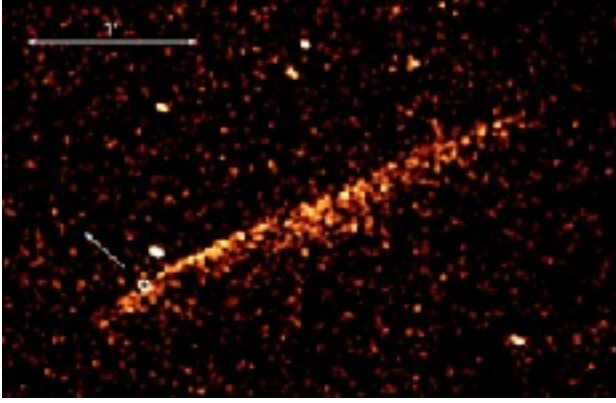


Fig. 28 Combined *Chandra* ACIS image (0.5–8 keV, 195 ks total exposure) of PSR B2224+65 and its misaligned outflow, in a coordinate frame moving with the pulsar. The image is a combination of two images separated by an interval of 6 years, during which the pulsar moved $1''$ on the sky.

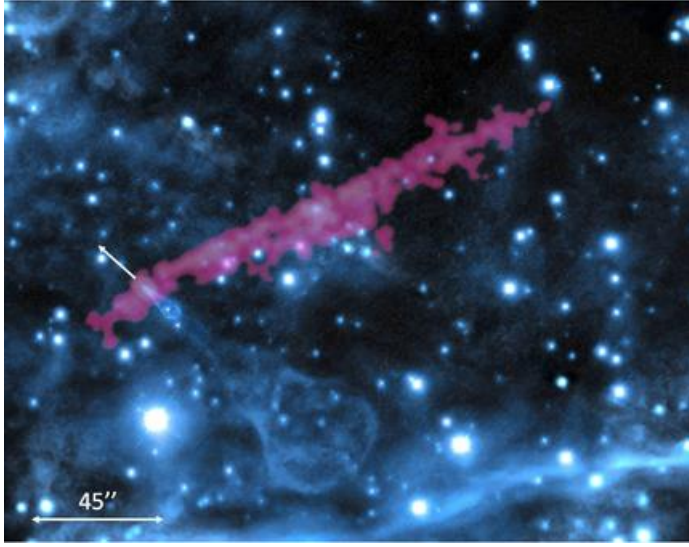


Fig. 29 Smoothed X-ray image from Figure 28 overlaid onto the $H\alpha$ image showing the Guitar. The $H\alpha$ image is taken from <http://chandra.harvard.edu/photo/2015/archives/>.

3.2.4 J1509–5850: Another misaligned outflow, a “three-tail” compact nebula, and a long tail

PSR J1509–5850 is a middle-aged ($\tau_{\text{sd}} = 154$ kyr) pulsar with $P = 89$ ms, $\dot{E} = 5.1 \times 10^{35}$ erg s $^{-1}$, and a dispersion-measure distance $d \approx 3.8$ kpc. Its X-ray PWN, consisting of a compact “head” and a long “tail” southwest of the pulsar, was discovered in a *Chandra* observation by Kargaltsev et al. (2008). Deep follow-up *Chandra* observations (374 ks total exposure) are described by Klingler et al. (2016a). In addition to the previously detected southwest tail extending up to $7'$ ($7.7d_{3.8}$ pc), these observations revealed similarly long (but fainter) diffuse emission stretched toward the north and the fine structure of the PWN

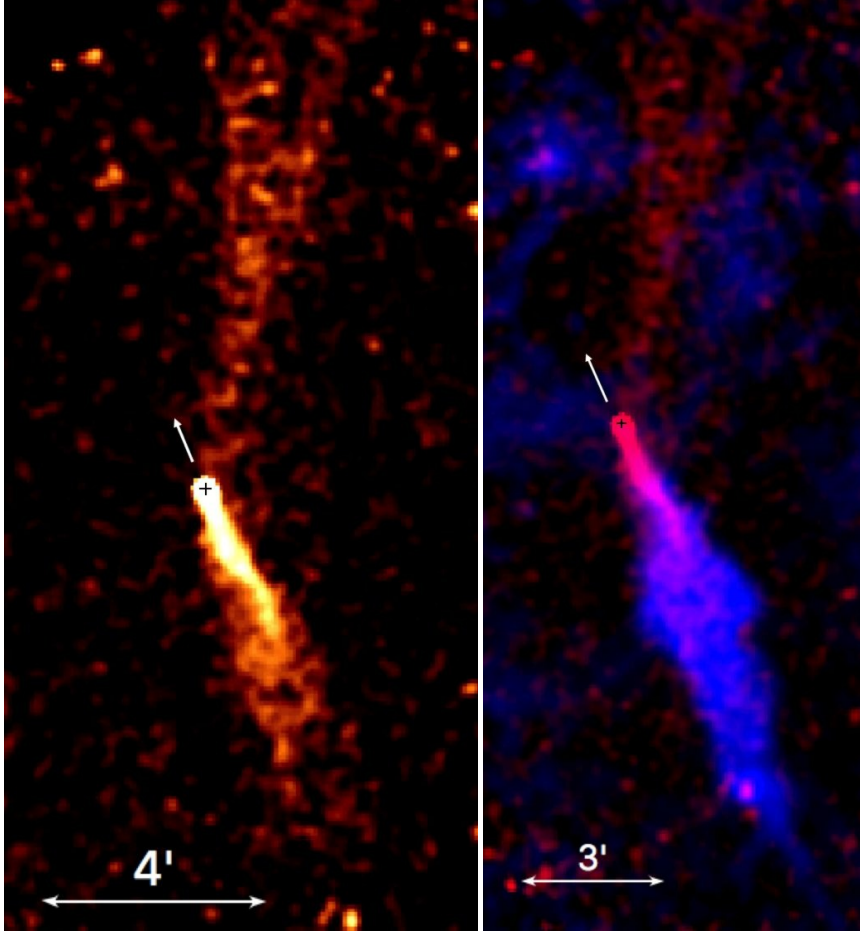


Fig. 30 Left: *Chandra* ACIS image of the J1509–5850 PWN (0.5–8 keV, 374 ks) showing the southwest tail and the misaligned outflow toward the north. Right: Combined *Chandra* ACIS (red) and VLA (blue) image of the same PWN. The arrows show an assumed direction of proper motion.

“head” (see Figure 30). The “head” (dubbed the Compact Nebula [CN] by Klingler et al. 2016a) is resolved into two lateral tails and one short central tail (Figure 31), remarkably similar to the Geminga PWN. Although the pulsar’s proper motion has not been measured, the overall CN and southwest tail morphology provides strong evidence that the pulsar is moving northeast. In this case the northern structure is another example of a misaligned outflow.

Klingler et al. (2016a) estimated upper and lower limits for the transverse velocity, $V_{\perp} \lesssim 640 d_{3.8} \text{ km s}^{-1}$ and $V_{\perp} \gtrsim 160 n_b^{-1/2} d_{3.8}^{-1} \text{ km s}^{-1}$, using upper limits on the pulsar’s proper motion and stand-off distance (the latter estimate assumes an isotropic PW). Being morphologically similar to the Geminga PWN, the CN of J1509–5850 is a factor of ~ 200 more luminous (e.g., $L_{0.5-8\text{keV}} \approx 7.5 \times 10^{31} d_{3.8}^2 \text{ erg s}^{-1}$ for the CN lateral tails) and a factor of ~ 10 more X-ray efficient ($\eta_{0.5-8\text{keV}} \equiv L_{0.5-8\text{keV}}/\dot{E} \approx 1.5 \times 10^{-4} d_{3.8}^2$ vs. $1.5 \times 10^{-5} d_{0.25}^2$ for Geminga). In addition, the spectra of the lateral tails are much softer in the CN than in

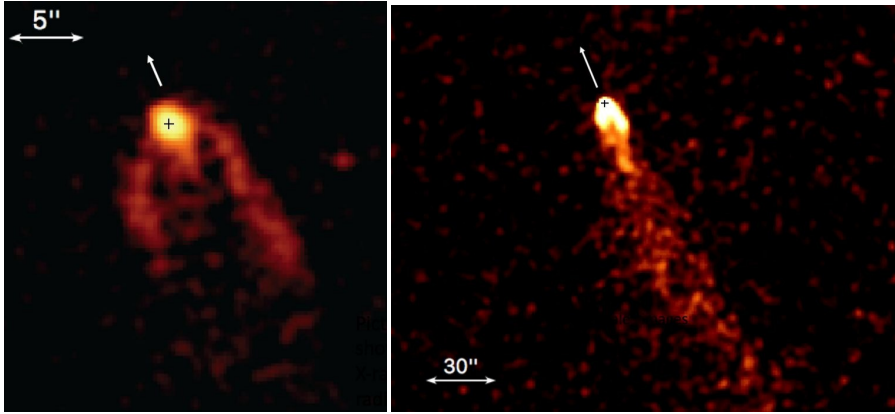


Fig. 31 Left: Compact X-ray nebula in the vicinity of PSR J1509–5850. Right: ACIS image demonstrating the transition from the compact nebula to the southwest tail.

the Geminga PWN ($\Gamma \approx 1.8$ vs. $\Gamma \approx 1$, respectively). The reason of these differences is currently unclear.

Being aligned with the CN symmetry axis, the extended tail southwest of the pulsar is obviously composed of a shocked PW collimated by ram pressure. Its luminosity is $L_{0.5-8\text{keV}} \approx 1 \times 10^{33} d_{3.8}^2 \text{ erg s}^{-1}$, and its spectral slope, $\Gamma \approx 1.9$, does not show any increase (rather a hint of decrease) with increasing distance from the pulsar. The lack of spectral softening suggests a very high speed of the outflowing matter. Alternatively, there could be some “reheating” due to in situ conversion of magnetic field energy into particle energy, e.g., via turbulent processes and accompanying reconnection, which might explain the hint of spectral hardening at large distances from the pulsar. The tail is also seen in radio up to about $10'$ from the pulsar (Ng et al. 2010). Surprisingly, the radio emission brightens with distance from the pulsar (contrary to the Mouse tail), becomes broader than the X-ray emission beyond $\approx 3'$, and then narrows again beyond $\approx 5'$ (see Figure 30). Another difference from the Mouse tail is the predominant magnetic field orientation, stretched along the tail in the Mouse and helical, with the helix axis parallel to the pulsar’s direction of motion, in the J1509 tail. The different magnetic field geometries possibly reflect different spin-velocity alignments of the parent pulsars.

The median of the $7'$ long wedge-like northern structure is inclined to the CN symmetry axis (alleged direction of proper motion) by $\approx 33^\circ$. Its luminosity, $L_{0.5-8\text{keV}} \approx 4 \times 10^{32} d_{3.8}^2$, is a factor of 2.5 lower than that of the southwest tail, while the spectral slope is about the same, with a slight hint of softening with increasing distance from the pulsar.

3.2.5 The complex PWN created by PSR B0355+54

PSR B0355+54, located at a parallax distance of $d = 1.0 \pm 0.2 \text{ kpc}$, is a middle-aged radio pulsar ($\tau_{\text{sd}} = 560 \text{ kyr}$) with a spin-down power $\dot{E} = 4.5 \times 10^{34} \text{ erg s}^{-1}$ and a period $P = 156 \text{ ms}$. Its transverse velocity, $V_{\perp} = 61_{-9}^{+12} d_1 \text{ km s}^{-1}$ towards the northeast, is among the lowest observed. Observations with *Chandra* and *XMM-Newton* revealed the presence of a PWN (dubbed the Mushroom by Kargaltsev and Pavlov 2008) consisting of a compact “cap” and a dimmer “stem”, with a hint of extended emission visible up to $\sim 7'$ (2 pc) southwest of the pulsar (McGowan et al. 2006). A series of 8 *Chandra* observations, performed over an

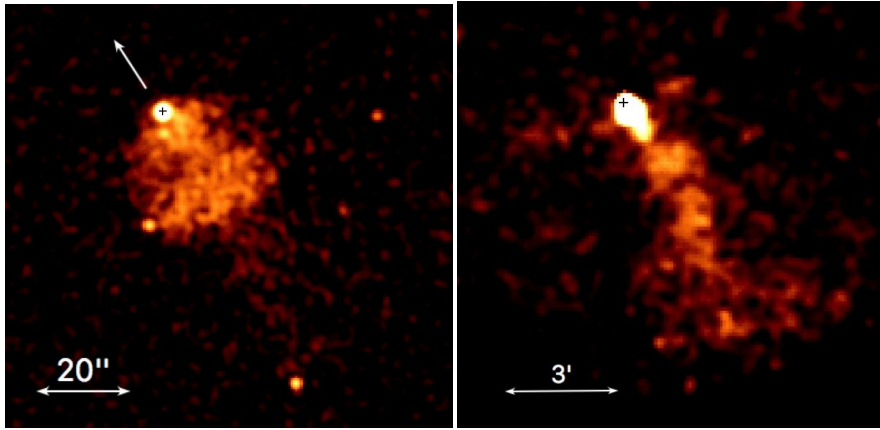


Fig. 32 *Chandra* ACIS images of the B0355+54 PWN (0.5–8 keV, 395 ks). Left: The compact PWN in the pulsar vicinity (the Mushroom). Right: The large-scale PWN, including the diffuse tail and the “whiskers”. The arrows show the direction of the proper motion.

8-month period in 2012–2013 (total exposure of 395 ks) revealed the detailed structure of the B0355+54 PWN (see Figure 32) and allowed us to measure the spectra of its elements (Klingler et al. 2016b). In particular, they showed a “filled” morphology of the cap, in contrast with the “hollow” morphologies of the Geminga PWN and the CN of the J1509–5850 PWN. The cap has a sharp trailing edge behind the pulsar and is brightened along the axis; its spectral slope is $\Gamma \approx 1.5$, a typical value for a PWN head. The stem is split into two structures that apparently originate from the pulsar and slightly diverge from each other further away. Klingler et al. (2016b) speculate that these structures could be pulsar’s jets swept back by the ram pressure, which could also explain the brightening along the cap’s axis. Overall, the “mushroom” morphology suggests a small angle between the pulsar’s spin axis and our line of sight, in agreement with the lack of γ -ray pulsations. The cap and stem luminosities are 1.8×10^{31} and 2.6×10^{30} erg s $^{-1}$, respectively.

A long diffuse tail behind the “mushroom” is likely due to synchrotron emission of the shocked PW behind the pulsar. Its luminosity is about 3.8×10^{31} erg s $^{-1}$, more than a half of the total PWN luminosity, $L_{0.5-8\text{keV}} \approx 6.4 \times 10^{31}$ erg s $^{-1}$ that corresponds to a total PWN efficiency $\eta_{0.5-8\text{keV}} \approx 1.4 \times 10^{-3}$. The spectrum of the tail, with a slope $\Gamma \sim 1.7$ –1.8, shows only a slight hint of cooling with increasing distance from the pulsar. This implies either a fast flow speed (or a very low magnetic field), or particle re-acceleration within the tail.

The deep observation also allowed Klingler et al. (2016b) to detect two additional very faint, extended features (dubbed “whiskers”) on either side of the compact nebula, likely another example of a misaligned outflow.

Thus, the B0355+54 PWN shows a particularly rich structure, which remains to be explained by PWN models. Radio and H α observations could shed light on its nature, but the PWN has not been detected at these wavelengths.

3.2.6 J1741–2054: Another tail behind a nearby middle-aged pulsar

Another example of a tail-like structure behind a moving pulsar is shown in Figure 33. This PWN was discovered by Romani et al. (2010) and investigated in detail by Auchettl et al. (2015) using results from 6 *Chandra* observations carried out in 2013 (282 ks total exposure).

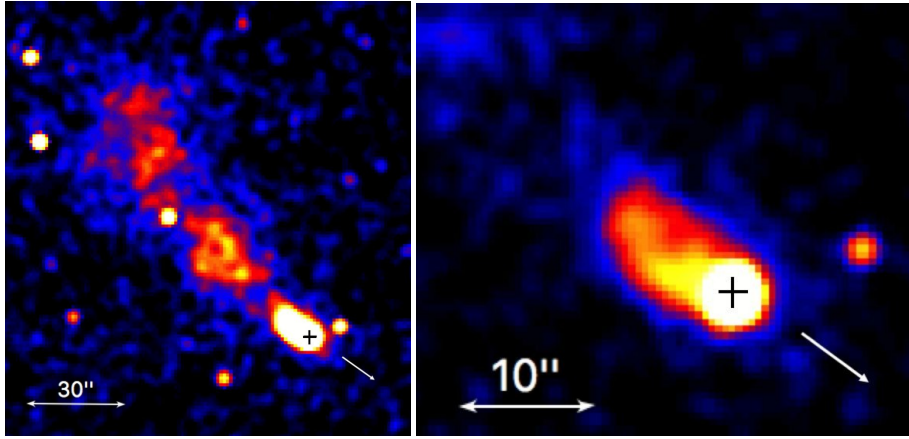


Fig. 33 Summed 0.3–6 keV *Chandra* ACIS images of the entire J1741–2054 PWN (left) and the leading bright component (right) from 5 observations in 2013 (282 ks total exposure). Black crosses show the pulsar position, white arrows show the direction of proper motion.

It is created by the nearby ($d \sim 0.38$ kpc) middle-aged ($\tau_{\text{sd}} = 390$ kyr) pulsar J1741–2044 ($P = 413$ ms, $\dot{E} = 9.5 \times 10^{33}$). The pulsar’s proper motion $\mu = 109 \pm 10$ mas yr $^{-1}$, measured by Auchettl et al. (2015) from the X-ray images, corresponds to the transverse velocity $V_{\perp} = (196 \pm 18)d_{0.38}$ km s $^{-1}$. In Figure 33 we can see a tail-like structure in the direction opposite to that of the proper motion. The structure consists of a compact elongated nebula of $\sim 15''$ length and a fainter diffuse tail seen up to $\sim 1'.7$ ($\sim 0.2d_{0.38}$ pc) from the pulsar. The tail is slightly bent and apparently consists of two “lobes”. No small-scale structure (PWN head) is resolved around the pulsar. The 0.5–10 keV luminosities of the compact nebula and the entire PWN, about 5×10^{29} and 3×10^{30} erg s $^{-1}$ at $d = 0.38$ kpc, are $\sim 5 \times 10^{-5}$ and $\sim 3 \times 10^{-4}$ of the pulsar’s spin-down power. The spectra of the PWN elements are described by a PL model with $\Gamma \approx 1.5$ – 1.7 , with only a hint of spectral softening with increasing distance from the pulsar.

For an isotropic PW, one could expect a PWN head with a leading edge at an angular distance $\theta_0 \approx 1'' d_{0.38}^{-2} n_b^{-1/2} \sin i$ ahead of the pulsar, too small to resolve separately from the pulsar’s PSF. The actual distance to the stagnation point is likely even smaller, as seen from the H α image (see Figure 34). The flat front of the H α bow shock allows one to assume that the wind of this pulsar is originally concentrated in the plane perpendicular to the pulsar’s velocity, presumably the equatorial plane, which implies that the pulsar’s rotational axis is parallel to the velocity vector. Being deflected by the ram pressure, the shocked PW forms the tail seen as a brighter compact component (Figure 33, right). The matter flowing in the tail is likely decelerated by the ISM entrainment, which leads to the broadening seen in the diffuse longer tail. To confirm this interpretation, flow velocities in the compact and extended tail components should be measured, but it was not possible with the data available.

3.2.7 J0357+3205: A tail detached from the pulsar

An interesting X-ray nebula created by a radio-quiet γ -ray pulsar J0357+3205 ($P = 444$ ms, $\tau_{\text{sd}} = 540$ kyr, $\dot{E} = 5.9 \times 10^{33}$ erg s $^{-1}$) is shown in Figure 35 (De Luca et al. 2011). The pulsar’s proper motion is $\mu = 164 \pm 20$ mas yr $^{-1}$ (De Luca et al. 2013), but the distance is unknown. For an assumed $d = 0.5$ kpc, its transverse velocity is $V_{\perp} = (389 \pm 47)d_{0.5}$

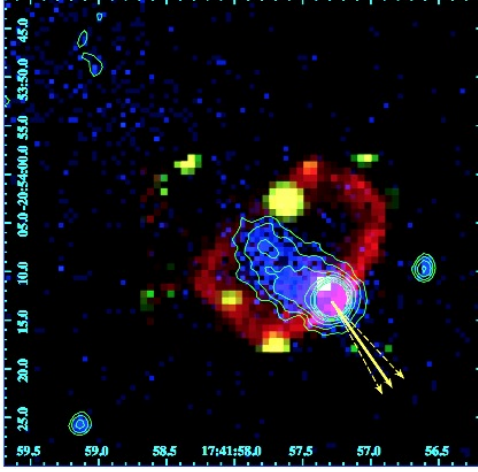


Fig. 34 The $H\alpha$ nebula (red) and the leading tail component of the X-ray PWN created by PSR J1741-2051 (Auchettl et al. 2015)

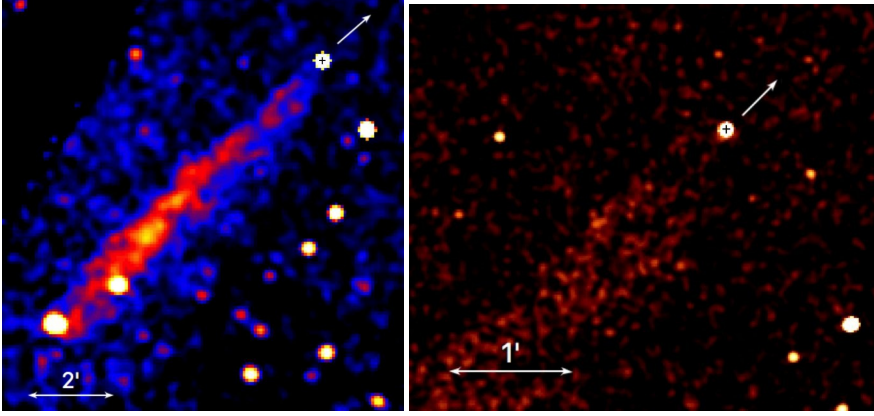


Fig. 35 Left: Merged *Chandra* ACIS image of the tail behind PSR J0357+3205 (0.5–6 keV, 4 observations, 136 ks total exposure). Right: Zoomed-in part of the same image showing the lack of tail emission in the pulsar vicinity.

km s^{-1} . The *Chandra* and *XMM-Newton* images show a $9'$ ($1.3d_{0.5}$ pc) long, relatively straight tail behind the pulsar, but no PWN head is seen. Moreover, the tail is detached from the pulsar (not seen up to $50''$), and its brightness increases with increasing distance from the pulsar, reaching a maximum at about $4'$. Another unusual property of the tail is the asymmetric brightness profile across the tail, with a sharp northeastern edge, resembling the “misaligned outflow” in the Gutar nebula. The tail’s luminosity, $L_{0.5-10\text{keV}} \approx 8.8 \times 10^{30} d_{0.5}^2 \text{ erg s}^{-1}$, is a fraction of $\sim 1.5 \times 10^{-3}$ of the pulsar’s spin-down power.

The tail’s spectrum fits a PL model with a photon index $\Gamma \approx 2$, without a significant dependence on the distance from the pulsar. Such a spectrum is consistent with the synchrotron emission from relativistic electrons in a shocked PW, but the lack of a PWN head is challenging for such an interpretation. Another potential problem is the relatively low value for the maximum synchrotron photon energy, $E_{\text{max}} \lesssim 30\eta\sigma B_{-5} \text{ keV}$ (see Equation 7), which is below 1 keV if $\eta\sigma B_{-5} \lesssim 0.03$. To circumvent these problems, Marelli et al. (2013) suggest

that the tail's emission is in fact thermal bremsstrahlung from the shocked ISM material with a temperature of about 4 keV. To heat the ISM up to such a high temperature, a very high pulsar velocity, $V_{\text{psr}} \sim 1900 \text{ km s}^{-1}$, is required (see Equation 9), larger than observed for any other pulsar, which would also imply a small angle, $i < 20^\circ$, between the velocity vector and the line of sight. The lack of diffuse emission at small distances from the pulsar could then be caused by the considerable time required for the energy transfer from ions, heated by the shock, to radiating electrons. If this scenario is confirmed by future observations, the J0357+3205 nebula would be the first example of a new class of thermally emitting nebulae associated with high-velocity pulsars.

3.2.8 Unexpectedly faint X-ray PWNe

From the above examples one could expect that any sufficiently powerful pulsar that has left its parent SNR produces a head-tail PWN, possibly with some misaligned outflows. However, observations of several nearby pulsars show either very faint extended emission around the pulsar or no extended emission at all. The most convincing examples of very faint (or undetected) PWNe were provided by observations of nearby pulsars B1055–52 and B0656+14.

PSR B1055–52 ($P = 197 \text{ ms}$, $\dot{E} = 3.0 \times 10^{34} \text{ erg s}^{-1}$, $\tau_{\text{sd}} = 535 \text{ kyr}$) is a bright γ -ray pulsar at an estimated distance of $\sim 350 \text{ pc}$ (Mignani et al. 2010). Its proper motion, $\mu = 42 \pm 5 \text{ mas yr}^{-1}$, corresponds to the transverse pulsar velocity $V_{\perp} \approx 70d_{0.35} \text{ km s}^{-1}$. A dedicated 56 ks *Chandra* ACIS observation by Posselt et al. (2015) showed some enhancement (with respect to the model PSF) in radial count distribution from $2''$ to $20''$, better seen in the soft X-ray band (0.3–1 keV), corresponding to the luminosity of $1\text{--}2 \times 10^{29} d_{0.35}^2 \text{ erg s}^{-1}$, which is $(3\text{--}6) \times 10^{-6} d_{0.35}^3$ of the pulsar's spindown power. The alleged extended emission showed only a hint of azimuthal asymmetry (an excess in the quadrant that includes the proper motion direction), at a 3σ level. This extended emission (if real) could be, at least partly, a dust scattering halo, but a very faint X-ray PWN cannot be excluded. Posselt et al. (2015) speculate that such a faint, nearly round PWN could be produced if the pulsar is moving away from us almost along the line of sight, i.e., $V_{\text{psr}} \gg V_{\perp}$. It, however, remains unclear whether this interpretation is correct.

Very similar results were obtained by Bîrzan et al. (2016) for PSR B0656+14 ($P = 385 \text{ ms}$, $\dot{E} = 3.8 \times 10^{34} \text{ erg s}^{-1}$, $\tau_{\text{sd}} = 111 \text{ kyr}$, and $d = 0.29 \pm 0.03 \text{ kpc}$ from parallax measurements). This pulsar also has a low transverse velocity, $V_{\perp} = (60 \pm 7)d_{0.29} \text{ km s}^{-1}$. From the analysis of archival *Chandra* ACIS and HRC data, Bîrzan et al. (2016) found a slight enhancement over the model PSF in an annulus of about $3''\text{--}15''$ around the pulsar, with a luminosity of $\sim 8 \times 10^{28} d_{0.29}^2 \text{ erg s}^{-1}$. This luminosity is $\sim 2 \times 10^{-6} d_{0.29}^2$ of the pulsar's spindown power, a factor of ~ 7 lower than the X-ray efficiency of the PWN of Geminga that has a similar (slightly higher) spindown power and is a factor of 3 older than PSR B0656+14. No azimuthal asymmetry was detected in the images. The spectrum of the enhancement is apparently very soft, $\Gamma \sim 8$, but its uncertainty is very large because the imaging ACIS observation was very short, about 5 ks. As in the case of B1055–52, the extended emission (if real) could be a combination of a dust scattering halo and a PWN created by the pulsar moving almost along the line of sight. The PWN and halo contributions could be disentangled from a longer ACIS observation.

Thus, a plausible explanation for the lack of the expected head-tail morphology and a very low PWN luminosity might be due to smallness of the angle between the pulsar velocity direction and the line of sight, which is also indicated by the small values of V_{\perp} .

However, the transverse velocity of PSR B0355+54 is similarly low, but that pulsar is accompanied by a PWN with a rich structure (see Figure 32). Moreover, the spindown power of PSR B0355+54 is similar to those of B1055–52 and B0656+14, but its PWN luminosity is at least a factor of 300 higher. Obviously, there must be some other factors that affect the X-ray efficiency and appearance of PWNe created by pulsars moving in the ISM. A possible reason for these differences could be different orientations of the pulsar rotational axes (hence the equatorial planes) with respect to their velocities. Another parameter on which the PWN properties should depend is the angle between the spin and magnetic axes, which affects the conversion of the PW magnetic energy into kinetic energy and particle acceleration. In particular, the very low efficiencies of some PWNe could be associated with nearly aligned spin and magnetic axes. To check these hypotheses, it would be useful to look for a correlation between the PWN properties and multiwavelength pulsations.

3.2.9 General overview of the X-ray PWNe created by supersonically moving pulsars

About 15 X-ray PWNe created by pulsars moving through the ISM have been detected. The spindown powers \dot{E} of these pulsars are in the range from 1.2×10^{33} erg s^{−1} (PSR B2224+65, the Guitar PWN) to 2.5×10^{36} erg s^{−1} (PSR J1747–2958, the Mouse PWN). Electrons/positrons of PWs of less powerful pulsars, which constitute the majority of rotation-powered pulsars, apparently cannot be accelerated to energies high enough to emit X-ray synchrotron radiation, and even if the energy is sufficient, the PWN luminosity may be too low to detect it, even from nearby sources.

The examples presented here show that most supersonically moving pulsars are accompanied by tails, with typical lengths of a few parsecs. However, the appearances of PWN heads vary considerably in different sources. Some of the well-resolved PWNe have a filled PWN head morphology (e.g., the Mouse, B0355+54, J1741–2044) while others show “hollow” morphologies (Geminga, J1509–5850). Moreover, there is at least one example, J0357+3205, which shows a long tail but no resolved PWN head around the pulsar. The diversity of PWN heads suggests that PWs of old pulsars are anisotropic, perhaps concentrated around the equatorial plane (as in the Crab and some other young pulsars) in many cases. The different appearances of the compact PWN components could be due to different orientations of the pulsar’s spin axis with respect to the velocity direction and the line of sight. A particularly puzzling morphology is seen in the Geminga PWN, with its three “tails”, which can be considered as a hollow-morphology compact PWN component observed from a close distance (it might have a much longer tail that is perhaps too faint to be detected by the current instruments).

Quite unexpected was the discovery of “misaligned outflows” in X-ray observations of several pulsars: B2224+65 (the Guitar), J1509–5850, B0355+54, described above, and likely the spectacular Lighthouse nebula created by PSR J1101–6101 (Pavan et al. 2016 and references therein; see Figure 36). Their nature still remains puzzling. A hypothesis was suggested by Bandiera (2008) that these features are produced by synchrotron radiation of very high energy particles leaked from the TSs into the ambient ISM along the ISM magnetic field, but this interpretation remains to be confirmed by quantitative modeling.

Although the flow speeds along the tails or misaligned outflows have not been directly measured, they have been crudely estimated for some tails based on circumstantial arguments. These estimates show that flow speeds considerably exceed the pulsar speeds, but they are well below the mildly relativistic speeds predicted by the numerical simulations.

The X-ray efficiencies, $\eta_X = L_X/\dot{E}$, of the observed PWNe vary between $\lesssim 2 \times 10^{-6}$ (the alleged PWN around PSR B0656+14) and $\sim 10^{-2}$ (the Mouse). The reason for such

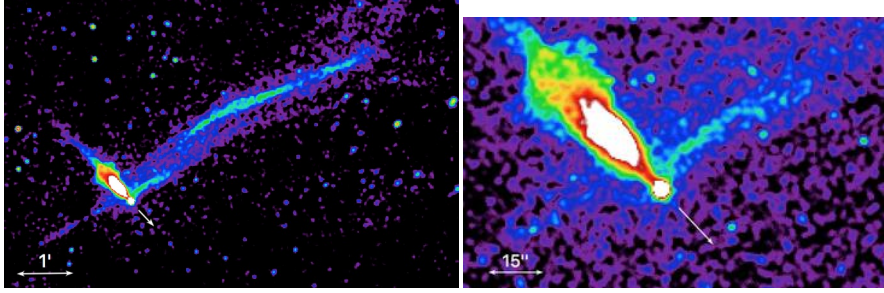


Fig. 36 *Chandra* ACIS image of the Lighthouse PWN (0.5–8 keV, 300 ks) created by PSR J1101–6101 ($\dot{E} = 1.4 \times 10^{36} \text{ erg s}^{-1}$, $\tau_{\text{sd}} = 116 \text{ kyr}$) moving from the SNR MSH 11–61A (Pavan et al. 2016). The image shows a bright tail behind the fast-moving pulsar ($V_{\perp} \sim 1000d_7 \text{ km s}^{-1}$) and an $11d_7$ pc long jet-like feature, possibly another example of a “misaligned outflow”.

a huge scatter remains unclear. At least partly, it can be due to different orientations of the pulsar equatorial planes, where the PWs are presumably concentrated, with respect to the pulsar velocities. It also may be that the fraction ξ_w of the spindown power lost to the PW is different in different pulsars (because the fraction of \dot{E} radiated from pulsar magnetospheres depends on pulsar parameters). Another likely reason for different PWN efficiencies is associated with conversion of the magnetic PW energy into the kinetic energy of particles, which should increase with increasing angle between the magnetic and spin axes.

The X-ray spectra of PWNe created by supersonically moving pulsars are usually well described by a PL model, which supports their synchrotron interpretation. Typical spectral slopes Γ in the compact nebula components (PWN heads) are in the range of 1.5–2.0, but the lateral tails of the Geminga PWN are much harder, $\Gamma \sim 0.7$ –1.0. Some of the PWN tails (e.g., in the Mouse and Lighthouse) show a substantial softening with increasing distance from the pulsar, up to $\Delta\Gamma \approx 1.0$ –1.5, while others show no softening at all, sometimes even a hint of hardening. The fast softening is an indication of a relatively high magnetic field (e.g., up to a few hundreds of μG in the Mouse, the highest value found so far, which is a factor of 10 higher than typical magnetic fields).

A few head-tail PWNe have been detected in the radio. The radio tails are usually longer than the X-ray ones, as expected from the synchrotron cooling. The additional radio data allow one to examine a broad-band PWN spectrum, which is usually harder in the radio than in the X-rays, and get an idea about the spectrum of emitting particles. Measuring the spatially resolved radio polarization makes it possible to map the directions of the magnetic field within the PWN, but the two PWNe for which such mapping was done (the Mouse and J1509–5850) show very different distributions.

The X-ray spectral slopes $\Gamma < 2$ suggest that the main contribution to the total synchrotron PWN luminosities are provided by photons with energies above the observed X-ray range, i.e., above $\sim 10 \text{ keV}$. However, none of the head-tail PWNe has been detected at hard X-rays or γ -rays, perhaps because the current detectors are not sensitive enough.

3.3 Open questions

Although many of the observed properties of PWNe produced by supersonically moving pulsars are qualitatively understood, there remain several problems that require further investigations, both observational and theoretical.

First of all, we should understand the reason(s) for the the *great diversity of PWN shapes*. Although elongated X-ray tails behind the moving pulsars have been observed in many of them, it is not quite clear which parameters determine the tail properties (shape, length, collimation and divergence, separation from the pulsar in some cases). Even less clear is the origin of the diversity of PWN heads (e.g., filled vs. hollow morphology). One of such parameters is obviously the angle between the velocity vector and the line of sight, but other parameters, such as the angle between the spin and magnetic axes, and between the spin axis and the pulsar velocity, can play an important role. It is also possible that the direction and strength of the ambient ISM magnetic field can affect the observed surface brightness distribution. To assess the contribution of the different factors, a study of correlation of the PWN shape with the shapes and phases of pulsar pulses at different wavelengths (e.g., radio and γ -rays), supplemented by PWN modeling in the case of anisotropic PW, would be particularly useful.

The most puzzling features among the recently discovered PWN components are the “*misaligned outflows*”, whose directions are strongly misaligned with respect to the pulsar velocities. It is tempting to interpret them as jets along the pulsar spin axes, similar to those observed in PWNe of young pulsars, but such jets are expected to be bent by the ram pressure on much smaller scales than the observed lengths of these nearly straight, elongated features. Only qualitative interpretations of such features have been suggested so far, which remain to be confirmed by quantitative modeling.

It remains unclear whether “ordinary” *jets along the spin axes* have been detected in old PWNe outside SNRs. May it be that the outflows along the spin axis are less powerful (at least, less luminous) in old pulsars than in young ones? To answer this question, we should obtain independent information on the spin axis directions, which could be done with the aid of multiwavelength polarimetry, in addition to the pulse analysis.

Since the X-ray PWN emission is synchrotron radiation from relativistic electrons and/or positrons, one should expect softening of the PWN spectrum with increasing distance from the pulsar due to synchrotron cooling. Such softening has indeed been observed in some of the tails, but other tails, as well as the misaligned outflows, show *no spectral softening* at all, but hints of hardening. What is the reason for such behavior? Is it an indication of an additional (re)acceleration (heating) along the tails? What is the acceleration mechanism? Is it the same mechanism that is responsible for the unusually hard spectra of the Geminga’s lateral tail? Why does it operate only in some tails? To answer these questions, deep high-resolution X-ray observations are required, which would allow spatially resolved spectral analysis to accurately measure the spectral changes. If the lack of softening (or even spectral hardening) is confirmed, possible acceleration mechanisms (e.g., the Fermi acceleration at fronts of oblique shocks or magnetic turbulence) should be studied.

Another puzzling problem is the *very low X-ray efficiency (or even the absence) of PWNe around some nearby pulsars* that are powerful enough to create an observable X-ray PWN. While it might be partly explained by closeness of the pulsar velocity direction to the line of sight, it is certainly not a full explanation. Are these PWNe so faint because the conversion of the PW magnetic energy into the particle energy (e.g., via magnetic field reconnection in the striped wind zone) is inefficient, as expected for pulsars with nearly aligned magnetic and spin axes? Are there other mechanisms that suppress the production and acceleration of the particle component of PWs? To understand the true reason, more nearby pulsars should be observed, and the absence or presence of PWNe should be confronted with the observed pulsar properties.

To conclude, significant progress in our understanding of PWNe of supersonically moving pulsars has been achieved, thanks to the high resolution and sensitivity of the *Chandra*

and *XMM-Newton* observatories, but there remain a number of open problems that could be resolved with further deep X-ray observations and more realistic modeling.

4 Gamma-ray observations of pulsar-wind nebulae

Gamma-ray astronomy has entered a golden age during the last decade thanks to the latest generation of space telescopes in the High-Energy (HE; $0.1 < E < 100$ GeV) domain (*Fermi*-LAT, *AGILE*), and ground-based instruments in the very-high energy (VHE; $0.1 < E < 100$ TeV) domain, in particular the Imaging Atmospheric Cherenkov Telescopes (IACTs) such as H.E.S.S., VERITAS and MAGIC, featuring unprecedented performance⁸. *Fermi*-LAT, with a large field-of-view of 2.4 sr, an angular resolution varying from $\sim 5^\circ$ at 100 MeV to $\lesssim 0.1^\circ$ above 50 GeV, and a point-source sensitivity at the level of $\sim 10^{-12}$ erg cm⁻² s⁻¹ in the GeV domain, has revealed more than 3000 (*3FGL*) sources in the 0.1-300 GeV band (Acero et al. 2015) and 360 (*2FHL*) sources above 50 GeV (Ackermann et al. 2016). IACTs have so far detected more than 170 VHE sources, two third of which being located in the Galaxy⁹. In particular, the H.E.S.S. experiment, exhibiting a 5 $^\circ$ -wide field-of-view, an angular resolution of $\sim 0.06^\circ$ and a point-source sensitivity of a few 10^{-12} erg cm⁻² s⁻¹ in the TeV domain, has surveyed the inner Galactic Plane during ten years, resulting in the detection of more than 70 sources¹⁰.

These GeV-TeV instruments offer for the first time the possibility to spatially resolve large enough sources such as middle-aged pulsar wind-nebulae (PWNe) and shell-type supernova remnants (SNRs), and to study source spectra over more than five decades in energy. Spectro-morphological studies are of prime importance as they allow one to pinpoint the origin of γ -ray emission from SNR systems in which the pulsar (PSR), the associated wind-nebula, and the host SNR shell, can contribute to the observed emission. In this regard, while *Fermi*-LAT has detected more than 200 PSRs in the HE domain¹¹, IACTs, and H.E.S.S. in particular, have revealed more than 30 TeV PWNe and PWN candidates associated with energetic PSRs (Klepser et al. 2013; Kargaltsev et al. 2013), a dozen of which being also detected at (multi-)GeV energies (Acero et al. 2013; Ackermann et al. 2016). Nevertheless, a large fraction of the HE/VHE sources in the Galaxy still remain unassociated due to the limitations of gamma-ray instruments to precisely characterize the source morphologies in most cases and to the difficulty for radio/X-ray telescopes to reveal structures at scales of the order of the typical VHE source sizes ($\sigma \sim 0.1$ - 0.3).

Gamma-ray emission from PWNe is usually interpreted in the so-called leptonic scenario¹², where the accelerated electron-positron pairs emit through inverse Compton (IC)

⁸In what follows, the angular resolutions are provided as the 68% containment radii. The *Fermi*-LAT sensitivity is given at TS = 25 in 10 y, for a source at $(\ell, b) = (0, 30)$ with Pass 8 data (https://www.slac.stanford.edu/exp/glast/groups/canda/lat_Performance.htm). The H.E.S.S. sensitivity is provided at 5σ in 25 h, for a source near zenith (<https://www.mpi-hd.mpg.de/hfm/HESS/pages/home/proposals/>). See also the dashed lines in Figure 38.

⁹See <http://tevcat.uchicago.edu/>

¹⁰From Abramowski et al. (H.E.S.S. Collaboration) 2016, in prep. See also <https://www.mpi-hd.mpg.de/hfm/HESS/pages/home/som/2016/01/>

¹¹<https://confluence.slac.stanford.edu/display/GLAMCOG/Public+List+of+LAT+Detected+Gamma-Ray+Pulsars>

¹²The possibility that a hadronic component could carry a significant fraction of the energy content in PWNe has been investigated in several works (see Di Palma et al. (2016) and references therein), but the observational evidence of the presence of accelerated ions in PWNe, through *e.g.* pion production in hadronic interactions and the subsequent emission of γ -rays and neutrinos, has been so far elusive.

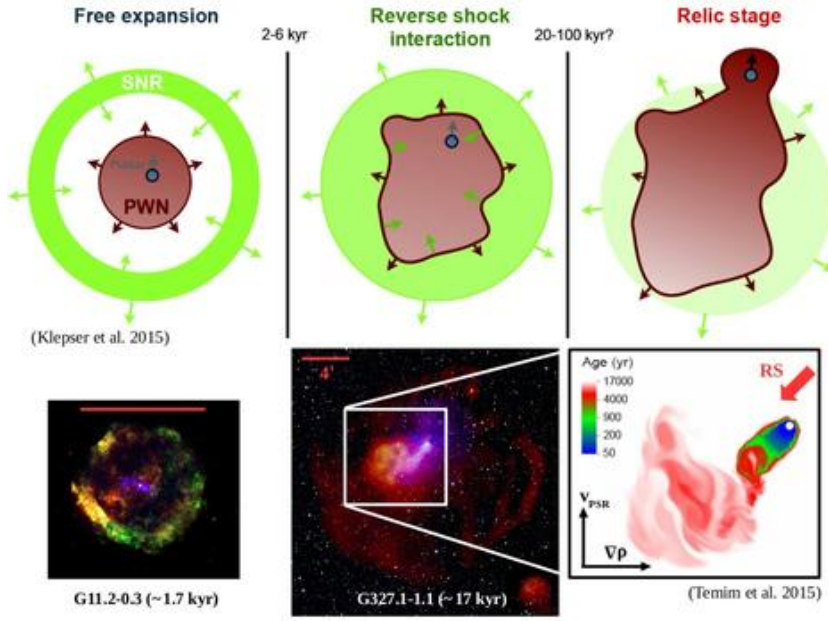


Fig. 37 PWN evolutionary phases. *Left*: young systems where the nebula lies at the center of the host shell-type SNR, as exemplified by G11.2-0.3 seen in X-rays. *Middle*: evolved nebulae, after the so-called crushing phase caused by the interaction with the asymmetric reverse shock (RS) due to an inhomogeneous ISM and/or a high PSR's proper motion, as illustrated by G327.1-1.1 observed in radio (red) and X-rays (blue). The inset image shows the age distribution of particles injected by the PSR some 17000 years ago, based on the hydrodynamical simulation of Temim et al. (2015) with the assumed ISM density gradient and PSR's velocity depicted by the two arrows. *Right*: bow-shock nebulae, when the pulsar motion through the SNR or the ISM becomes supersonic.

scattering off the ambient low-energy photons, from the CMB and the interstellar radiation fields (ISRFs) made of infrared emission from dust and optical/UV starlight. In this framework, HE/VHE observations allow one to derive the spectral distribution and energy content of the high-energy particles (provided the ISRFs are known), to reveal their spatial distribution, and to set important constraints on the particle acceleration and transport mechanisms. Furthermore, these measurements, when combined with radio/X-ray observations of the synchrotron (SC) component, provide estimates of the magnetic field strength and distribution in these sources, as we shall see below.

Two classes of γ -ray PWNe can be distinguished according to their evolutionary stages, as shown in Figure 37 (no clear evidence of γ -ray emission associated with a bow-shock nebula [see section 3] has been reported so far). First, *young* PWNe, such as the Crab nebula, MSH 15-52, G0.9+0.1, G21.5-0.9 and Kes 75 (discussed in section 4.1), are usually found at the center of their host shell-type SNRs and are seen as unresolved or compact γ -ray sources. HESS J1818-154, a compact TeV source located at the center of the radio SNR G15.4+0.1, is worth to be mentioned as being the first PWN discovered by TeV observations in a composite SNR (H.E.S.S. Collaboration et al. 2014). Second, *middle-aged* PWNe (with PSR characteristic ages of $\gtrsim 10^4$ yr), such as HESS J1356-645 (see Figure 38), HESS J1825-137 (section 4.2.1), and the peculiar Vela PWN (section 4.2.2), are usually resolved in the HE/VHE domains and are found to be significantly offset from the current position of the associated PSR, with large size ratios between the X-ray and γ -ray

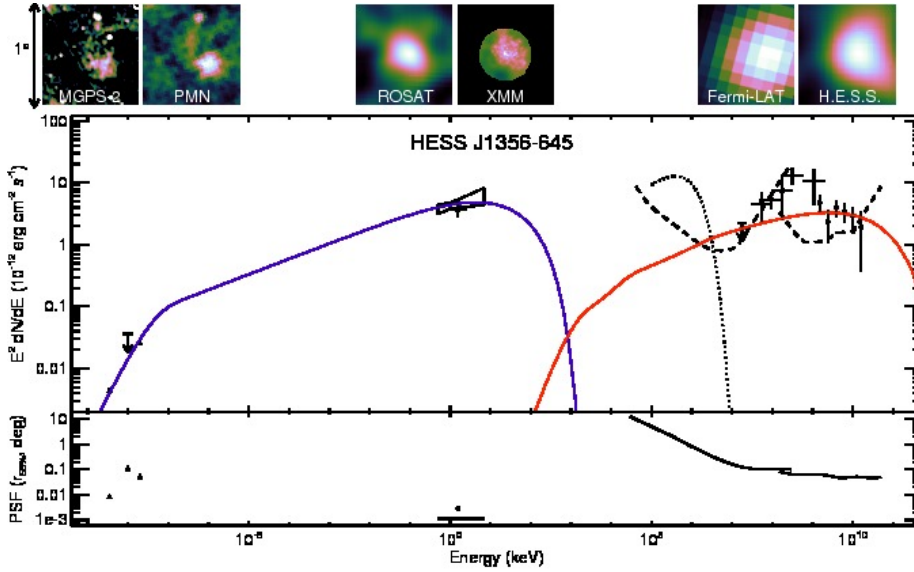


Fig. 38 Broadband spectrum of the PWN HESS J1356–645 (H.E.S.S. Collaboration et al. 2011; Ackermann et al. 2016). The blue and red solid curves give the SC and IC emission from a one-zone, time-independent, modeling performed in H.E.S.S. Collaboration et al. (2011). The dotted line represents the best-fit phase-averaged spectrum of PSR J1357–6429 as obtained in Lemoine-Goumard et al. (2011). The two dashed lines show the *Fermi*-LAT and H.E.S.S. point-source sensitivities (see text for more details). The 1-wide multi-wavelength images, as obtained in H.E.S.S. Collaboration et al. (2011); Ackermann et al. (2016), centered on the PSR position, are also shown. The lower panel presents the angular resolutions of the considered radio, X-ray and gamma-ray instruments.

emission regions. The evolution of the SNR into an inhomogeneous ISM, through the interaction with an asymmetric reverse shock (RS), and/or the high PSR’s velocity (Blondin et al. 2001; van der Swaluw et al. 2004; Temim et al. 2015) can lead to a displacement of the crushed PWN from the SNR center. Also, mean magnetic field strengths within these γ -ray PWNe as low as $\sim 3\text{--}5\ \mu\text{G}$ are required in order to prevent the TeV-emitting electrons from suffering from severe radiative losses, enabling the majority of them to survive from (and hence probe) early epochs of the PWN evolution (de Jager and Djannati-Ataï 2009). All these effects can thus explain the large-offset X-ray-faint long-lived γ -ray sources as being the relic nebulae from the past history of the pulsar wind inside its host SNR.

4.1 Young PWNe

Several time-dependent models of the radiative (sometimes coupled with the dynamical) evolution of PWNe have been developed in order to estimate, from the observed broadband non-thermal emission, the energy distribution and content of particles and the wind magnetization, and to constrain the particle acceleration mechanisms at work in these sources (Gelfand et al. 2009; Fang and Zhang 2010; Tanaka and Takahara 2010, 2011; Bucciantini et al. 2011; Martín et al. 2012; Vorster et al. 2013; Torres et al. 2014). Figure 39 shows the broadband spectra from G21.5-0.9 and Kes 75, two young PWNe respectively associated with the energetic pulsars PSR J1833-1034 and PSR J1846-0258 and detected in the VHE domain (Djannati-Ataï et al. 2008), together with the best-fit models from Torres et al.

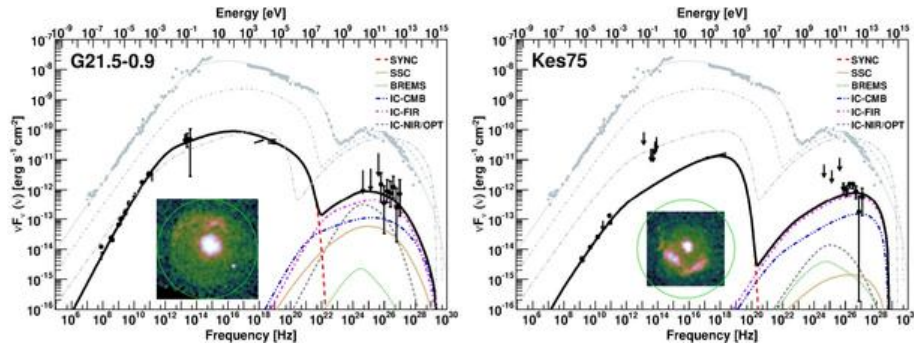


Fig. 39 Broadband spectra of G21.5-0.9 (left) and Kes 75 (right) with the best-fit models from Torres et al. (2014) shown as solid lines. The grey dots and lines correspond to the multi-wavelength data and the associated models (at different ages) for the Crab nebula. *Chandra* X-ray images of these two PWNe with the typical H.E.S.S. PSF depicted as a green circle are also shown.

(2014). The common findings of all the above-mentioned modelings are as follows: the particle energy distribution is well described by a broken power law with an intrinsic break¹³ (*i.e.* assumed to be of non-radiative origin) at a Lorentz factor of $\sim 10^{5-6}$, and almost all of the young PWNe considered in these studies are particle-dominated. This is translated into large pair multiplicities ($\kappa \gtrsim 10^4$) and magnetic fractions of \lesssim a few percent (*i.e.* with magnetic fields lower than the equipartition values), with TeV emission dominated by IC scattering off (far-)infrared photons (with energy densities generally larger than the Galactic large-scale ISRFs provided by Porter and Strong (2005)). Although these constraints are valuable to pinpoint the particle acceleration mechanisms (Amato 2015), it should be noted that these modelings assume a one-zone emission region (in the 1D approximation, known to face several issues such as the so-called σ problem, cf. a brief discussion in section 3.1), whereas the unresolved TeV emission from *e.g.* G21.5–0.9 and Kes 75 (see Figure 39) and the debated origin of the radio emission from these young PWNe could question this assumption. Also, relying on (or rescaling) the commonly used Galactic ISRFs as an estimate of the *local* fields from dust and stars is another major source of uncertainty which directly affects the predicted IC emission.

4.2 Middle-aged PWNe

As discussed above, middle-aged PWNe are observed in the HE/VHE domain as extended sources, offset from the PSR position. These two characteristics make them difficult to identify as such from γ -ray observations, and many of the so-called *dark* VHE sources, with no obvious radio/X-ray counterpart, could actually be such ancient nebulae (de Jager et al. 2009). Besides dedicated pulsars search (with *Fermi*-LAT in particular) within the VHE source extent, multi-wavelength investigation, as shown in Figure 38 in the case of HESS J1356–645, and energy-dependent γ -ray morphological analysis (as commonly done in X-rays) are the two means to unveil their nature.

¹³The modeling presented in Vorster et al. (2013) assumes that the particle spectrum has a discontinuity at the transition between the low- and high-energy components.

4.2.1 HESS J1825–137: energy-dependent morphology and particle transport mechanisms

HESS J1825–137 is the archetypal middle-aged PWN, discovered by H.E.S.S. (Aharonian et al. 2006a) as a bright, $\sim 1^\circ$ -large (*i.e.* ~ 70 pc at 4 kpc) source offset from the energetic radio pulsar PSR J1826–1334, and later detected with *Fermi*-LAT (Grondin et al. 2011). A detailed spectro-morphological analysis has revealed for the first time in the VHE domain a steepening of the energy spectrum with increasing distance from the pulsar, likely due to the cooling losses of electrons during their transport in the nebula. This is illustrated by the three-colour image in Figure 40 (left) revealing the shrinking of the nebula with increasing energy and hence the physical connection between the TeV PWN with PSR J1826–1334, also responsible for the compact hard-index X-ray nebula of size $\sim 30''$ embedded in a $\sim 10'$ -large softer structure (Pavlov et al. 2008; Van Etten and Romani 2011). These γ -ray measurements, when combined with X-ray observations, provide important constraints on the particle injection, transport and cooling within the nebula: a detailed 3D time-dependent multi-zone spectro-morphological modeling (Van Etten and Romani 2011) has shown a good agreement with the data by including radially decreasing advection velocity and magnetic field profiles and substantial particle diffusion in order to explain the presence of multi-TeV particles ~ 80 pc away from the pulsar. Such a rapid diffusion is at odds with the toroidal magnetic field structure effective at smaller scales in many PWNe leading to strong magnetic confinement of particles.

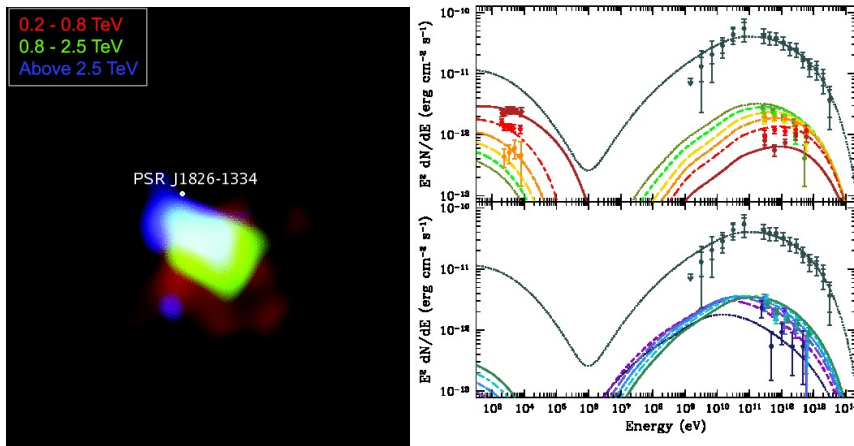


Fig. 40 *Left:* Three-color 3-large image of HESS J1825-137 as observed with H.E.S.S. in different energy bands (Funk et al. 2008) showing the shrinking of the nebula with increasing energy. *Right:* Broadband spectra from the whole PWN (slate data points and dotted line) and from different wedges in HESS J1825-137 with a color scale evolving from dark red (inner region) to green, blue and violet (outer region), as defined in Aharonian et al. (2006a). Lines represent the best-fit model presented in Van Etten and Romani (2011) (see text for more details).

4.2.2 Vela X: multi-wavelength picture and particle escape

The energetic Vela pulsar (PSR B0833–45, $\tau_c = 11$ kyr, $P = 89$ ms, $\dot{E} = 7 \times 10^{36}$ erg s $^{-1}$), embedded in the nearby 8-large Vela SNR located at $d \sim 290$ pc, is known to power sev-

eral manifestations of wind nebulae seen at different spatial scales: a compact X-ray nebula composed of two toroidal arcs at sub-arcmin scales and a $4'$ long collimated jet (Helfand et al. 2001; Pavlov et al. 2003), an extended hard X-ray emission ($E > 18$ keV) north of the pulsar (Mattana et al. 2011), a $45'$ elongated X-ray structure dubbed the *Vela cocoon*, also detected at TeV energies with H.E.S.S. (Aharonian et al. 2006b) and partially coincident with a bright radio filament (LaMassa et al. 2008), and the Vela X nebula (referred to as the *Vela halo*, encompassing the cocoon area), a large-scale 2×3 non-thermal radio region offset by $\sim 40'$ from the pulsar that is also detected at GeV energies with *Fermi*-LAT (Abdo et al. 2010). Two distinct lepton populations have been suggested to explain the different broadband spectra of the latter two emission regions: a young population producing the X-ray/VHE cocoon and a relic one responsible for the radio/HE halo (de Jager et al. 2009), with similar magnetic field strengths of $\sim 3\text{--}5 \mu\text{G}$ (Abdo et al. 2010). However, such an interpretation has been challenged by several new observational evidences: TeV emission beyond the cocoon, extended over much of the halo and featuring a similar VHE spectrum, has been detected with H.E.S.S. (Abramowski et al. 2012), and a detailed spectromorphological *Fermi*-LAT data analysis has revealed two new spatial HE features matching the so-called northern and southern wings of Vela X as seen with *WMAP* and *Planck*, with marginally different spectra (Grondin et al. 2013). Such a complex morphology, with several emission components at different scales, is highlighted in the multi-wavelength image shown in Figure 41 (left).

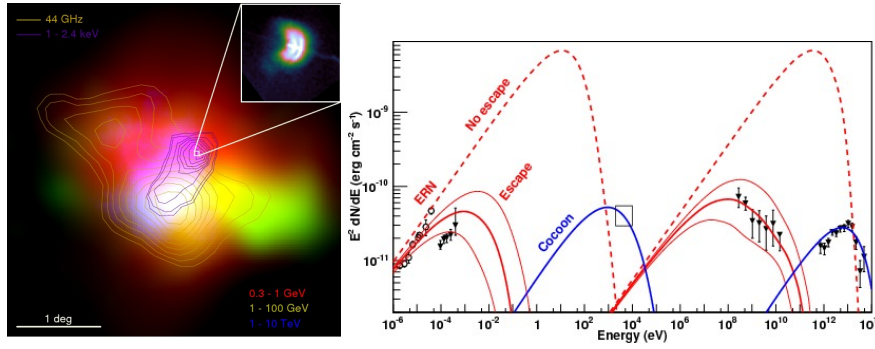


Fig. 41 *Left*: multi-wavelength picture of Vela PWN. The 4-wide three-color image (in Galactic coordinates) is composed of the 0.3-1 GeV (red) and 1-100 GeV (green) emission measured with *Fermi*-LAT (Grondin et al. 2013), and of the 1-10 TeV (blue) emission detected with H.E.S.S. (Abramowski et al. 2012). Contours represent the 44 GHz radio emission measured by *Planck* (Planck Collaboration et al. 2016) and the X-ray emission above 1 keV observed with *ROSAT* (in blue). The well-known X-ray compact nebula around the Vela PSR is shown in the inset on the upper right corner (*Chandra*/ACIS 0.3-10 keV image). *Right*: broadband spectrum of Vela PWN (ERN: Extended Radio Nebula) with (solid lines) and without (dashed lines) the assumption of particle escape throughout its evolution, according to Hinton et al. (2011).

These new γ -ray measurements provide direct evidence that high-energy leptons are present in the extended halo, ~ 10 pc away from the pulsar. In order to explain the steep spectra measured with *Fermi*-LAT, diffusive escape of particles from the radio nebula has been invoked by Hinton et al. (2011) (see Figure 41, right), as in the case of HESS J1825-137 discussed in section 4.2.1. While particle confinement is thought to be important during the early PWN evolution, the interaction with the SNR reverse shock could thus make the diffusion of particles out of the nebula possible. Such an energy-dependent escape in this

nearby PWN should produce a clear signature in the local CR lepton spectrum (Hinton et al. 2011; Della Torre et al. 2015). Latest measurements with AMS-02 (Aguilar et al. 2014a,b) have shown an increase of the positron fraction with increasing energy, which could be explained by the Galactic PSR population and in particular by a few nearby PSRs (Hooper et al. 2009; Di Mauro et al. 2014; Boudaud et al. 2015). Therefore, continuing HE/VHE observations of middle-aged and bow-shock PWNe are crucial to estimate the total energy content of high-energy particles residing inside these sources in order to assess the importance of escape mechanisms throughout their evolution, and hence their contribution to the Galactic CR lepton spectra observed at Earth.

5 Outflows in magnetars

Magnetars differ from the rotation-powered NS discussed in the previous sections because a strong magnetic field is the main energy source which ultimately powers their persistent and bursting/flaring emission (Mereghetti et al. 2015). Unlike ordinary pulsars, which show no or very little variability, magnetars are characterized by a variety of transient phenomena on timescales from a few milliseconds to years and involving flux changes as large as several orders of magnitude. There are many indications that their magnetosphere is highly dynamic and characterized by a complex non-dipolar geometry. It is thus expected that magnetars might also be able to accelerate charged particles and produce outflows which, in principle, can lead to the formation of diffuse nebulae.

Owing to their long spin periods (>2 s), magnetars have rotational energy losses much smaller than those of the energetic pulsars typically associated with PWNe. The magnetar with the highest spin-down rate, 1E 1547.0–5408, has $\dot{E}_{ROT} = 2.1 \times 10^{35}$ erg s $^{-1}$, but more typical values are in the range $\sim 10^{32} - 10^{34}$ erg s $^{-1}$. While the ratio L_{PWN}/\dot{E}_{ROT} is a useful description of the efficiency of classical PWNe, the analogous quantity for magnetars, L_{MWN}/\dot{E}_{ROT} is less relevant, because their nebulae might be powered, at least in part, by magnetic energy. In fact, the observation of time-variable radio and hard X-ray emission after giant flares, as well as the presence of long-lived nebulae around some magnetars, provide evidence that these neutron stars can emit relativistic particle outflows.

In this section we discuss two kinds of observational results which give evidence for relativistic outflows from magnetars: (a) the detection of time-variable emission associated to the occurrence of giant flares, and (b) the presence of persistent diffuse emission at radio and/or X-ray energies around some magnetars.

5.1 Outflows during Giant Flares

Giant flares are the most extreme manifestations of magnetars, involving radiated energies up to about 10^{46} erg (assuming isotropic emission). They are rare events: only three have been observed in more than 40 years (each one from a different source, in a sample now totalling at least two dozen magnetars (Olausen and Kaspi 2014)). The famous giant flare of 1979 March 5, from the Large Magellanic Cloud source SGR 0526–66, was crucial for our understanding of magnetars, but due to its large distance and unexpected occurrence, it could not be studied in much detail.

More data could be obtained for the giant flare emitted on 1998 August 27 from the Galactic magnetar SGR 1900+14. Observations carried out with the VLA about one week after the outburst revealed a faint (~ 0.3 mJy), unresolved radio source (angular diameter

$\theta < 0.8''$), which became undetectable after a few days (Frail et al. 1999). A power law index $\alpha = 0.74 \pm 0.15$ was derived from the fluxes at 1.43 and 4.86 GHz. This radio emission was interpreted as a cloud of synchrotron emitting relativistic particles ejected during the giant flare (or in the phase of intense bursting activity which preceded it). Simple equipartition arguments led to an estimate for the nebula minimum energy of $1.6 \times 10^{43} (d/10 \text{ kpc})^{17/7} (\theta/0.4'')^{9/7} \text{ erg}$.

The event of 2004 December 27 from SGR 1806–20 was by far the most energetic and best studied giant flare, with an isotropic energy release in hard X-rays and γ -rays of more than $5 \times 10^{45} (d/10 \text{ kpc})^2 \text{ erg}$. The expanding radio nebula detected after this flare could be observed for more than one year (Gaensler et al. 2005; Cameron et al. 2005; Granot et al. 2006). It had a peak flux of $\sim 170 \text{ mJy}$ at 1.4 GHz in the first observation, carried out about one week after the giant flare. The flux then decreased as a steep power law of time, $F(t) \propto t^{-\delta}$ with $\delta \sim 3$, and, after a brief rebrightening at ~ 25 days after the flare, it followed a shallower power law decay with $\delta \sim 1.1$. The radio source was spatially resolved and featured an elliptical shape; it expanded from $\sim 60 \text{ mas}$ to $\sim 400 \text{ mas}$ in a couple of months, while at the same time its centroid moved by about 200 mas, along the direction of the elongation. The power-law spectrum and linear polarization indicate that the radio emission is synchrotron radiation. The minimum energy in the radio nebula was of the order of a few 10^{43} erg . This is much larger than the energy available in the electron/positron pairs escaping the initial fireball (Nakar et al. 2005), implying that the relativistic flow powering the nebula was loaded by baryons or Poynting flux. Indeed, the observed properties of the expanding nebula are well explained by an asymmetric ejection of few 10^{24} g of mildly relativistic baryons, $v/c \sim 0.3 (d/10 \text{ kpc})$, which interact with a pre-existing shell of matter surrounding the magnetar (Gelfand et al. 2005; Granot et al. 2006).

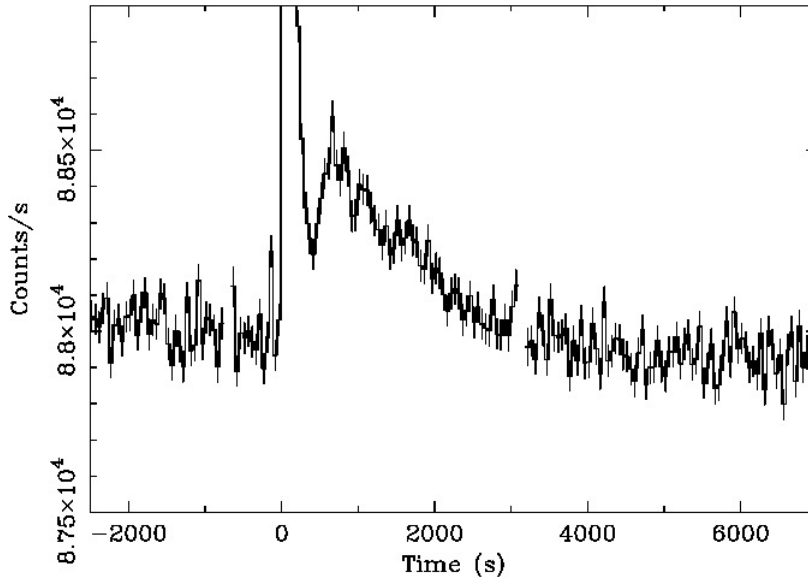


Fig. 42 High-energy ($>80 \text{ keV}$) light curve of the 27 December 2004 giant flare of SGR 1806–20 measured with the INTEGRAL satellite (from Mereghetti et al. (2005)). After the bright flare truncated in the plot (reaching $> 2 \times 10^6 \text{ counts s}^{-1}$) a long tail of hard X-ray emission, which peaks at $t \sim 500 \text{ s}$ and lasts more than one hour is clearly visible.

High-energy data obtained immediately after the SGR 1806–20 giant flare provided additional evidence for the ejection of relativistic matter. The *INTEGRAL* satellite revealed emission at energy above ~ 80 keV, which peaked about 11 minutes after the start of the flare and then decreased approximately as $F(t) \propto t^{-0.85}$ (Fig. 42). Evidence for this long-lasting high-energy emission was later found also in the *Konus/WIND* and *RHESSI* data (Frederiks et al. 2007; Boggs et al. 2007), which indicated a duration of at least 10^4 s and a hard spectrum (power-law photon index $\Gamma \sim 1.6$). No pulsations at the NS rotation period of 7.56 s were seen in this component, consistent with an origin far from the star surface and/or magnetosphere. This long-lasting emission can be interpreted as a hard X-ray afterglow produced by the fireball ejected in the initial spike of the giant flare (Mereghetti et al. 2005).

5.2 Magnetar wind nebulae

The identification and study of “magnetar wind nebulae” (MWNe) is complicated by the fact that most magnetars lie in crowded and highly absorbed regions of the Galactic plane and can be surrounded by diffuse emission of different origins, such as supernova remnants, molecular clouds, and H II regions. For example, SGR 1806–20 was initially associated with a variable radio nebula (Frail et al. 1997), but, when a better localization of this magnetar was obtained, it became apparent that a different object¹⁴ is powering the radio emission. Other magnetars are located inside radio-emitting supernova remnants, but no signs of enhanced radio emission directly connected with the neutron star has been found. Therefore, there is no evidence up to now for diffuse emission produced by magnetars in the radio band, besides that of the transient nebulae associated to giant flares described above.

In the X-ray range, where diffuse emission has been seen around several magnetars, a further complication results from the effect of interstellar dust scattering. Remarkable

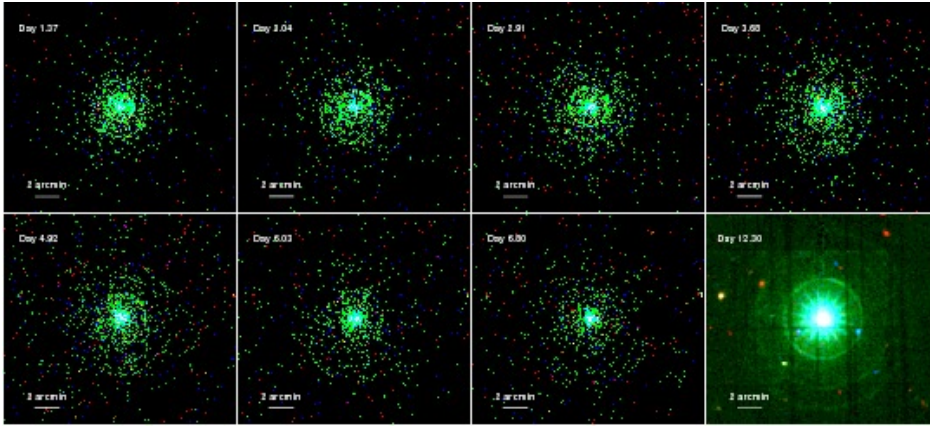


Fig. 43 Images of the expanding X-ray rings caused by interstellar dust scattering around the transient magnetar 1E 1547.0–5408 (from Tiengo et al. (2010b)). The seven *Swift* observations and the *XMM-Newton* observation (bottom right panel) were obtained from one to 12 days after a very bright burst that occurred on 2009 January 22. The apparent angular expansion of the three rings is due to the longer pathlength of the burst radiation scattered by three layers of dust along the line of sight.

¹⁴the luminous blue variable star LBV 1806–20 (Figer et al. 2004).

evidence for the importance of this effect was demonstrated by the expanding X-ray rings (Fig. 43) seen around 1E 1547.0–5408 after its January 2009 outburst (Tiengo et al. 2010a).

Excess X-ray emission over the *XMM-Newton* PSF was detected at radii from $\sim 10''$ up to $\sim 2'$ around the transient SGR 1833–0832 (Esposito et al. 2011). Its spectrum was softer than that of the central source, as expected for a halo caused by interstellar dust, due to the E^{-2} dependence of the scattering cross section. Given the high absorption of SGR 1833–0832 ($N_H = 10^{23} \text{ cm}^{-2}$), a large amount of dust is likely present along its line of sight. Thus, the diffuse X-ray emission around this source, as well as that reported for other highly absorbed sources like SGR 1900+14 (Kouveliotou et al. 2001) and SGR 1806–20 (Kaplan et al. 2002; Viganò et al. 2014), is probably due to dust scattering. Recently, diffuse X-rays with a steep power-law spectrum have been detected around SGR J1935+2154, on an angular scale of about one arcmin with *XMM-Newton* (Israel et al. 2016; Younes et al. 2017). This could be a dust scattering halo, but a possible contribution from a wind nebula cannot be excluded.

To date, the best evidence for a MWN is provided by the case of Swift J1834.9–0846. This magnetar is surrounded by extended X-ray features with different spatial scales (Fig. 44). The X-ray emission within a radius of $\sim 40''$, resolved in *Chandra* images (Kargaltsev et al. 2012), is most likely due to dust scattering of the outburst emission of this transient. Its flux varied in correlation with that of the central source, as expected for such small angles in case of dust scattering (Esposito et al. 2013). The more extended X-ray emission, with an elongated shape ($\sim 2' \times 1'$) and a constant flux detected with *XMM-Newton* in 2005, 2011 and 2014, is instead best explained as a MWN (Younes et al. 2012, 2016). In favour of this interpretation are the relatively hard spectrum of the nebula, which is well fit by a power law with photon index $\Gamma=2.2$, and the apparent lack of variability. For a distance of 4 kpc, sug-

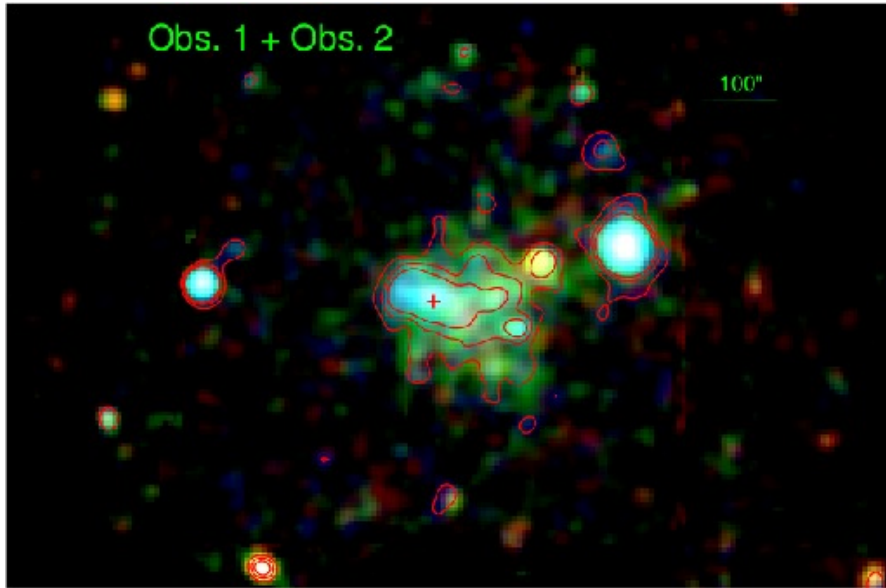


Fig. 44 X-ray image of the region of Swift J1834.9–0846 obtained with the *XMM-Newton* satellite (from Younes et al. (2016)). The cross indicates the position of the magnetar. The colors code the X-ray energy (red 2–3 keV, green 3–4.5 keV, 4.5–10 keV blue). The contours are at the 2.5, 3.0, and 3.5 σ level. For a distance of 4 kpc, 100'' correspond to ~ 2 pc (horizontal bar).

gested by the possible association of Swift J1834.9–0846 with the supernova remnant W41, the nebula has an X-ray luminosity of $\sim 3 \times 10^{33} \text{ erg s}^{-1}$. This luminosity, which might be underestimated if the source is at a larger distance, represents a considerable fraction of the the spin-down power, $\dot{E}_{\text{ROT}} = 2.1 \times 10^{34} \text{ erg s}^{-1}$, of Swift J1834.9–0846.

We presented above the evidence for relativistic ejections during the giant flares, but, according to the magnetar model, the acceleration of particles in the magnetosphere is not restricted to these extremely energetic events. The normal bursting activity is expected to produce particle outflows, and Alfvén waves can drive a steady wind also during “quiescent” periods (Thompson and Duncan 1996; Harding et al. 1999). In this respect, it is more meaningful to compare L_{MWN} with the total reservoir of magnetic energy. For example, if we assume for Swift J1834.9–0846 the age of $\sim 10^5 \text{ yr}$ estimated for the W41 supernova remnant (Tian et al. 2007), the total energy radiated in X-rays in the nebula (a few 10^{38} erg) is a very small fraction of the magnetic energy $\sim R^2 \Delta R B^2 \sim 10^{45} B_{14}^2 \text{ erg}$, if the field is in a crustal depth of $\Delta R \sim 1 \text{ km}$ (although probably only a small part of such energy may be available for powering a nebula).

Indeed, several authors recently proposed models in which the nebula of Swift J1834.9–0846 is magnetically-powered (Tong 2016; Granot et al. 2017). Considering the few observational data available up to now for this alleged MWN, there is considerable degeneracy in the numerous involved parameters and it is not surprising that such models led to rather different estimates for the PWN and magnetar properties. For example, the wind braking scenario of Tong (2016) invokes a flow of particles with luminosity between 10^{36} and $10^{38} \text{ erg s}^{-1}$ and requires a rather high magnetic field in the nebula, $\sim 10^{-4} \text{ G}$, while Granot et al. (2017) estimate a likely upper limit of $\sim 30 \mu\text{G}$. An alternative interpretation, in which the Swift J1834.9–0846 nebula is powered by rotational energy, like normal PWNe, has been proposed by Torres (2016). This is energetically possible if one considers the rotationally-powered wind injected over the whole lifetime of the magnetar and the reverberation effect due to the location in a particularly dense ambient medium.

6 Gamma-ray binaries: pulsar winds interacting with a massive companion

The last decade has revealed a new group of gamma-ray emitters, composed of a fast-rotating pulsar and a massive star. The emission, which peaks in the MeV band, arises from the shocked region between the stellar wind and the pulsar wind. The binary interaction typically takes place around one AU from the pulsar, about 5 orders of magnitude closer than for pulsars interacting with the ISM. Although only a handful of these systems have been discovered, theoretical work benefits from the well-constrained environment created by the binary companion and the wealth of information provided by orbital variability. As such, gamma-ray binaries have opened a new window on pulsar wind physics. This subject is reviewed fully elsewhere.

7 Conclusions

The phenomenology of pulsar winds and their impact on their environments is a rich one, documented from radio to TeV photon energies. These objects pose various problems of particle acceleration and propagation, magnetic-field evolution, and neutron-star physics. Here we have summarized the spectra and morphology (primarily at X-ray and gamma-ray energies) of PWNe still in their natal shell supernova remnants, young PWNe which for some

reason lack shells, PWNe from much older pulsars, interacting directly with the interstellar medium; and magnetars, with tantalizing but not yet definitive evidence for magnetar wind nebulae (MWNe).

Young PWNe exhibit their pulsars at near-birth properties, generally with high spin-down luminosities. The PWNe interact with expanding ejecta in SNR interiors, tending to produce fairly symmetric objects, at least compared to morphologies observed for much older objects. These objects radiate synchrotron radiation from radio through hard X-rays, whose SED contains important information on particle acceleration and propagation. The flat radio spectrum of these PWNe is still unexplained; the few anomalous PWNe with steep radio spectra have very unusual properties, such as very large ratios of radio to X-ray sizes. The spectra steepen in the mm–IR region of the spectrum, generally by larger amounts than can be accounted for by the simplest models.

NuSTAR observations above 10 keV have provided important new information on the X-ray properties of young PWNe. PWN sizes decrease with increasing photon energy; that energy-dependence encodes information on electron propagation (advective, diffusive, or a combination). It is still not clear if intrinsic spectral structure is required to explain the observations, or whether synchrotron losses in inhomogeneous sources with some combination of advection and diffusion can explain the observed size decrease and spectral steepening with increasing distance from the pulsar. *NuSTAR* observations also show unexpected slight steepening of X-ray spectra in the interiors of the Crab Nebula and G21.5–0.9. This effect may be a clue to some feature of particle energization near the pulsar-wind shock not yet explored.

The spatial resolution of *NuSTAR* allows the determination of anisotropic morphological changes with increasing photon energy that support strong asymmetry in the pulsar outflows beyond the termination shock. In the Crab Nebula, the energy-dependence of the torus radius is about what is predicted in the Kennel-Coroniti spherically symmetric model, while the NW counterjet length drops much more steeply with increasing energy, at a rate comparable to that seen in both MSH 15-52 and G21.5–0.9. This resemblance suggests a commonality of origin not yet explained. MHD models of young PWNe will need to have more accurate treatment of the spatial and temporal evolution of relativistic-particle distributions in order to confront these data effectively.

Pulsars that have left their host SNRs move in the ISM with supersonic velocities, which drastically changes PWN morphologies. In particular, long tails, with a typical length of a few parsecs, form behind the fast-moving pulsars. These tails, collimated by the ram pressure of the oncoming ISM, are fast outflows of the shocked PW emitting synchrotron radiation from radio to hard X-rays. In addition, PWN “heads” in the pulsar vicinity are seen in deep high-resolution X-ray images. The appearance of PWN heads, very different in different objects, depends on the direction of the pulsar velocity with respect to the line of sight, as well as on the inclinations of the velocity vector and the magnetic axis to the spin axis. The observed shapes of the heads differ significantly from the current PWN models. The main reason for these differences is likely the unrealistic model assumption that the unshocked PW is isotropic.

In addition to the PWN tails and heads, deep X-ray observations have revealed “misaligned outflows” in some PWNe, at large angles to the pulsar velocities. Such outflows are not predicted by the current PWN models, and their true nature remains puzzling.

The X-ray spectra of the head-tail PWNe are usually well described by power-law models, with typical photon indices $\Gamma \sim 1.5\text{--}2.0$ in the pulsar vicinity. This implies power-law spectral energy distributions of the X-ray emitting relativistic electrons/positrons, $dN_e/d\gamma \propto \gamma^{-p}$, with $p \sim 2\text{--}3$. Some PWNe show spectral softening with increasing distance from the

pulsar, with $\Delta\Gamma \approx 1.0\text{--}1.5$, which can be due to synchrotron cooling. However, no softening is seen in other PWNe, which remains unexplained. Moreover, the lateral tails of the Geminga PWN have unusually hard spectra, $\Gamma \sim 0.7\text{--}1.0$, without measurable spectral softening, which might suggest an unusual acceleration mechanism for the radiating electrons.

Typical equipartition magnetic fields in head-tail PWNe are $\sim 10\text{--}100\ \mu\text{G}$. Interpreting the spectral softening observed in some tails as caused by synchrotron cooling, one can crudely estimate flow speeds $V_{\text{flow}} \sim 10^4\ \text{km s}^{-1}$, much faster than the pulsar speed but much slower than the mildly relativistic speeds predicted by some models.

Head-tail PWNe have been detected in X-rays only for sufficiently powerful pulsars, $\dot{E} \gtrsim 10^{33}\ \text{erg s}^{-1}$, likely because electrons cannot be accelerated to high enough energies in less powerful pulsars. Unexpectedly, the X-ray efficiency, $\eta_X = L_X/\dot{E}$, of head-tail PWNe shows a huge scatter, up to 4 orders of magnitude. Moreover, several nearby pulsars with $\dot{E} > 10^{34}\ \text{erg s}^{-1}$ show either very faint PWNe or no PWN at all. This might be associated with small angles between the spin and magnetic axes, but the true reason remains unclear. To explain this and other puzzling properties of the X-ray PWNe created by supersonically moving pulsars, more such objects should be observed in X-rays and other spectral domains, with long exposures and high spatial resolution, and new, more realistic models should be developed.

Gamma-ray observations of PWNe have provided important insights on several aspects such as the spatial and spectral distributions of the high-energy particles, their total energy content and the wind magnetization. From a theoretical point of view, 3D time-dependent multi-zone spectro-morphological models [*e.g.* Van Etten and Romani (2011)] are required in order to grasp the processes of particle acceleration, transport and escape in these nebulae. From an observational point of view, the identification of these HE/VHE PWNe requires extensive multi-wavelength investigation and/or detailed spectro-morphological studies, only feasible for bright and resolved sources. In most cases, the association of a γ -ray source with counterparts at other wavelengths is uncertain¹⁵. In this regard, thanks to a factor ~ 10 improvement in sensitivity above 100 GeV, with substantially better angular and spectral resolutions and wider field-of-view than the current IACTs, the Cherenkov Telescope Array (CTA; Acharya et al. (2013)), currently in its pre-production phase, will have the potential to reveal hundreds of sources through a uniform Galactic Plane survey (Dubus et al. 2013). This will undoubtedly trigger detailed morphological and spectral investigations towards a large number of PWNe and meaningful population studies de Oña-Wilhelmi et al. (2013).

Acknowledgements SPR thanks the *NuSTAR* team for their outstanding work and permission to present their PWN results. GGP, OK, and NK are grateful to Andrei Bykov and Maxim Lyutikov for helpful discussions, and to Blagoy Rangelov and Bettina Posselt for their help in data analysis. Support for their work was provided by the National Aeronautics and Space Administration through *Chandra* Awards G03-14082 and G03-14057 issued by the *Chandra* X-ray Observatory Center, which is operated by the Smithsonian Astrophysical Observatory for and on behalf of the National Aeronautics Space Administration under contract NAS8-03060. The work was also partly supported by NASA grant NNX08AD71G. MR is grateful to Jamie Cohen and Marco Ajello for providing the *Fermi*-LAT 2FHL image towards HESS J1356-645 and to Marie-Hélène Grondin for the *Fermi*-LAT images of Vela X.

All of us warmly thank the organizers for the invitation to participate in this very stimulating ISSI workshop on *Jets and Winds in Pulsar Wind Nebulae, Gamma-ray Bursts and Blazars: Physics of Extreme Energy Release*, and the International Space Science Institute (ISSI) for support.

¹⁵ As illustrated by HESS J1640-645 Abramowski et al. (2014) coincident with the radio SNR G338.3-0.0 hosting one compact and one extended X-ray source in its center which turned out to be an energetic pulsar (PSR J1640-4631, Gotthelf et al. (2014)) and its wind nebula.

References

- A.A. Abdo, M. Ackermann, M. Ajello, A. Allafort, L. Baldini, J. Ballet, G. Barbiellini, D. Bastieri, K. Bechtol, R. Bellazzini, B. Berenji, R.D. Blandford, E.D. Bloom, E. Bonamente, A.W. Borgland, A. Bouvier, J. Bregeon, A. Brez, M. Brigida, P. Bruel, T.H. Burnett, S. Buson, G.A. Caliandro, R.A. Cameron, P.A. Caraveo, S. Carrigan, J.M. Casandjian, C. Cecchi, Ö. Çelik, A. Chekhtman, C.C. Chung, J. Chiang, S. Ciprini, R. Claus, J. Cohen-Tanugi, J. Conrad, A. de Angelis, F. de Palma, M. Dormody, E.d.C.e. Silva, P.S. Drell, R. Dubois, D. Dumora, C. Farnier, C. Favuzzi, S.J. Fegan, W.B. Focke, P. Fortin, M. Frailis, Y. Fukazawa, S. Funk, P. Fusco, F. Gargano, N. Gehrels, S. Germani, G. Giavitto, N. Giglietto, F. Giordano, T. Glanzman, G. Godfrey, I.A. Grenier, M.-H. Grondin, J.E. Grove, L. Guillemot, S. Guiriec, A.K. Harding, M. Hayashida, E. Hays, D. Horan, R.E. Hughes, M.S. Jackson, G. Jóhannesson, A.S. Johnson, T.J. Johnson, W.N. Johnson, S. Johnston, T. Kamae, H. Katagiri, J. Kataoka, N. Kawai, M. Kerr, J. Knödseder, M. Kuss, J. Lande, L. Latronico, S.-H. Lee, M. Lemoine-Goumard, M. Llena Garde, F. Longo, F. Loparco, B. Lott, M.N. Lovellette, P. Lubrano, A. Makeev, M. Marelli, M.N. Mazziotta, J.E. McEnery, C. Meurer, P.F. Michelson, W. Mitthumsiri, T. Mizuno, A.A. Moiseev, C. Monte, M.E. Monzani, A. Morselli, I.V. Moskalenko, S. Murgia, T. Nakamori, P.L. Nolan, J.P. Norris, A. Noutsos, E. Nuss, T. Ohsugi, N. Omodei, E. Orlando, J.F. Ormes, M. Ozaki, D. Paneque, J.H. Panetta, D. Parent, V. Pelassa, M. Pepe, M. Pesce-Rollins, M. Pierbattista, F. Piron, T.A. Porter, S. Rainò, R. Rando, P.S. Ray, N. Rea, A. Reimer, O. Reimer, T. Reposeur, S. Ritz, A.Y. Rodriguez, R.W. Romani, M. Roth, F. Ryde, H.F.-W. Sadrozinski, D. Sanchez, A. Sander, P.M. Saz Parkinson, J.D. Scargle, C. Sgrò, E.J. Siskind, D.A. Smith, P.D. Smith, G. Spandre, P. Spinelli, M.S. Strickman, D.J. Suson, H. Tajima, H. Takahashi, T. Takahashi, T. Tanaka, J.B. Thayer, J.G. Thayer, D.J. Thompson, L. Tibaldo, D.F. Torres, G. Tosti, A. Tramacere, Y. Uchiyama, T.L. Usher, A. Van Etten, V. Vasileiou, C. Venter, N. Vilchez, V. Vitale, A.P. Waite, P. Wang, P. Weltevrede, B.L. Winer, K.S. Wood, T. Ylinen, M. Ziegler, Fermi Large Area Telescope Observations of the Vela-X Pulsar Wind Nebula. *ApJ* **713**, 146–153 (2010). doi:10.1088/0004-637X/713/1/146
- A. Abramowski, F. Acero, F. Aharonian, A.G. Akhperjanian, G. Anton, S. Balenderan, A. Balzer, A. Barnacka, Y. Becherini, J. Becker Tjus, K. Bernlöhr, E. Birsin, J. Biteau, A. Bochow, C. Boisson, J. Bolmont, P. Bordas, J. Brucker, F. Brun, P. Brun, T. Bulik, S. Carrigan, S. Casanova, M. Cerruti, P.M. Chadwick, A. Charbonnier, R.C.G. Chaves, A. Cheesebrough, G. Cologne, J. Conrad, C. Couturier, M. Dalton, M.K. Daniel, I.D. Davids, B. Degrange, C. Deil, P. deWilt, H.J. Dickinson, A. Djannati-Ataï, W. Domainko, L.O. Drury, F. Dubois, G. Dubus, K. Dutton, J. Dyks, M. Dyrda, K. Egberts, P. Eger, P. Espigat, L. Fallon, C. Farnier, S. Fegan, F. Feinstein, M.V. Fernandes, D. Fernandez, A. Fiasson, G. Fontaine, A. Förster, M. Füßling, M. Gajdus, Y.A. Gallant, T. Garrigoux, H. Gast, B. Giebels, J.F. Glicenstein, B. Glück, D. Göring, M.-H. Grondin, S. Häffner, J.D. Hague, J. Hahn, D. Hampf, J. Harris, S. Heinz, G. Heinzelmann, G. Henri, G. Hermann, A. Hillert, J.A. Hinton, W. Hofmann, P. Hofverberg, M. Holler, D. Horns, A. Jacholkowska, C. Jahn, M. Jamroz, I. Jung, M.A. Kastendieck, K. Katarzyński, U. Katz, S. Kaufmann, B. Khélifi, D. Klochkov, W. Kluzniak, T. Kneiske, N. Komin, K. Kosack, R. Kossakowski, F. Krayzel, P.P. Krüger, H. Laffon, G. Lamanna, J.-P. Lenain, D. Lennarz, T. Lohse, A. Lopatin, C.-C. Lu, V. Marandon, A. Marcowith, J. Masbou, G. Maurin, N. Mated, M. Mayer, T.J.L. McComb, M.C. Medina, J. Méhault, U. Menzler, R. Moderski, M. Mohamed, E. Moulin, C.L. Naumann, M. Naumann-Godo, M. de Naurois, D. Nedbal, N. Nguyen, J. Niemiec, S.J. Nolan, S. Ohm, E. de Oña Wilhelmi, B. Opitz, M. Ostrowski, I. Oya, M. Panter, D. Parsons, M. Paz Arribas, N.W. Pekeur, G. Pelletier, J. Perez, P.-O. Petrucci, B. Peyaud, S. Pita, G. Pühlhofer, M. Punch, A. Quirrenbach, M. Raue, A. Reimer, O. Reimer, M. Renaud, R. de los Reyes, F. Rieger, J. Ripken, L. Rob, S. Rosier-Lees, G. Rowell, B. Rudak, C.B. Rulten, V. Sahakian, D.A. Sanchez, A. Santangelo, R. Schlickeiser, A. Schulz, U. Schwanke, S. Schwarzburg, S. Schwemmer, F. Sheidaei, J.L. Skilton, H. Sol, G. Spengler, L. Stawarz, R. Steenkamp, C. Stegmann, F. Stinzing, K. Stycz, I. Sushch, A. Szostek, J.-P. Tavernet, R. Terrier, M. Tluczykont, C. Trichard, K. Valerius, C. van Eldik, G. Vasileiadis, C. Venter, A. Viana, P. Vincent, H.J. Völk, F. Volpe, S. Vorobiov, M. Vorster, S.J. Wagner, M. Ward, R. White, A. Wierchowska, D. Wouters, M. Zacharias, A. Zajczyk, A.A. Zdziarski, A. Zech, H.-S. Zechlin, Probing the extent of the non-thermal emission from the Vela X region at TeV energies with H.E.S.S. *A&A* **548**, 38 (2012). doi:10.1051/0004-6361/201219919
- A. Abramowski, F. Aharonian, F.A. Benkhali, A.G. Akhperjanian, E. Angüner, G. Anton, S. Balenderan, A. Balzer, A. Barnacka, Y. Becherini, et al., HESS J1640-465 - an exceptionally luminous TeV γ -ray supernova remnant. *MNRAS* **439**, 2828–2836 (2014). doi:10.1093/mnras/stu139
- F. Acero, M. Ackermann, M. Ajello, A. Allafort, L. Baldini, J. Ballet, G. Barbiellini, D. Bastieri, K. Bechtol, R. Bellazzini, R.D. Blandford, E.D. Bloom, E. Bonamente, E. Bottacini, T.J. Brandt, J. Bregeon, M. Brigida, P. Bruel, R. Buehler, S. Buson, G.A. Caliandro, R.A. Cameron, P.A. Caraveo, C. Cecchi, E. Charles, R.C.G. Chaves, A. Chekhtman, J. Chiaro, G. Chiaro, S. Ciprini, R. Claus, J. Cohen-Tanugi, J. Conrad, S. Cutini, M. Dalton, F. D’Ammando, F. de Palma, C.D. Dermer, L. Di Venere, E.d.C.e. Silva, P.S. Drell, A. Drlica-Wagner, L. Falletti, C. Favuzzi, S.J. Fegan, E.C. Ferrara, W.B. Focke, A.

- Franckowiak, Y. Fukazawa, S. Funk, P. Fusco, F. Gargano, D. Gasparrini, N. Giglietto, F. Giordano, M. Giroletti, T. Glanzman, G. Godfrey, T. Grégoire, I.A. Grenier, M.-H. Grondin, J.E. Grove, S. Guiriec, D. Hadasch, Y. Hanabata, A.K. Harding, M. Hayashida, K. Hayashi, E. Hays, J. Hewitt, A.B. Hill, D. Horan, X. Hou, R.E. Hughes, Y. Inoue, M.S. Jackson, T. Jogler, G. Jóhannesson, A.S. Johnson, T. Kamae, T. Kawano, M. Kerr, J. Knödlseider, M. Kuss, J. Lande, S. Larsson, L. Latronico, M. Lemoine-Goumard, F. Longo, F. Loparco, M.N. Lovellette, P. Lubrano, M. Marelli, F. Massaro, M. Mayer, M.N. Mazziotta, J.E. McEnery, J. Mehault, P.F. Michelson, W. Mitthumsiri, T. Mizuno, C. Monte, M.E. Monzani, A. Morselli, I.V. Moskalenko, S. Murgia, T. Nakamori, R. Nemmen, E. Nuss, T. Ohsugi, A. Okumura, M. Orienti, E. Orlando, J.F. Ormes, D. Paneque, J.H. Panetta, J.S. Perkins, M. Pesce-Rollins, F. Piron, G. Pivato, T.A. Porter, S. Rainò, R. Rando, M. Razzano, A. Reimer, O. Reimer, T. Reposeur, S. Ritz, M. Roth, R. Rousseau, P.M. Saz Parkinson, A. Schulz, C. Sgrò, E.J. Siskind, D.A. Smith, G. Spandre, P. Spinelli, D.J. Suson, H. Takahashi, Y. Takeuchi, J.G. Thayer, J.B. Thayer, D.J. Thompson, L. Tibaldo, O. Tibolla, M. Tinivella, D.F. Torres, G. Tosti, E. Troja, Y. Uchiyama, J. Vandenbroucke, V. Vasileiou, G. Vianello, V. Vitale, M. Werner, B.L. Winer, K.S. Wood, Z. Yang, Constraints on the Galactic Population of TeV Pulsar Wind Nebulae Using Fermi Large Area Telescope Observations. *ApJ* **773**, 77 (2013). doi:10.1088/0004-637X/773/1/77
- F. Acero, M. Ackermann, M. Ajello, A. Albert, W.B. Atwood, M. Axelsson, L. Baldini, J. Ballet, G. Barbiellini, D. Bastieri, A. Belfiore, R. Bellazzini, E. Bissaldi, R.D. Blandford, E.D. Bloom, J.R. Bogart, R. Bonino, E. Bottacini, J. Bregeon, R.J. Britto, P. Bruel, R. Buehler, T.H. Burnett, S. Buson, G.A. Caliandro, R.A. Cameron, R. Caputo, M. Caragiulo, P.A. Caraveo, J.M. Casandjian, E. Cavazzuti, E. Charles, R.C.G. Chaves, A. Chekhtman, C.C. Cheung, J. Chiang, G. Chiaro, S. Ciprini, R. Claus, J. Cohen-Tanugi, L.R. Cominsky, J. Conrad, S. Cutini, F. D'Ammando, A. de Angelis, M. DeKlotz, F. de Palma, R. Desiante, S.W. Digel, L. Di Venere, P.S. Drell, R. Dubois, D. Dumora, C. Favuzzi, S.J. Fegan, E.C. Ferrara, J. Finke, A. Franckowiak, Y. Fukazawa, S. Funk, P. Fusco, F. Gargano, D. Gasparrini, B. Giebels, N. Giglietto, P. Giommi, F. Giordano, M. Giroletti, T. Glanzman, G. Godfrey, I.A. Grenier, M.-H. Grondin, J.E. Grove, L. Guillemot, S. Guiriec, D. Hadasch, A.K. Harding, E. Hays, J.W. Hewitt, A.B. Hill, D. Horan, G. Iafate, T. Jogler, G. Jóhannesson, R.P. Johnson, A.S. Johnson, T.J. Johnson, W.N. Johnson, T. Kamae, J. Kataoka, J. Katsuta, M. Kuss, G. La Mura, D. Landriu, S. Larsson, L. Latronico, M. Lemoine-Goumard, J. Li, L. Li, F. Longo, F. Loparco, B. Lott, M.N. Lovellette, P. Lubrano, G.M. Madejski, F. Massaro, M. Mayer, M.N. Mazziotta, J.E. McEnery, P.F. Michelson, N. Mirabal, T. Mizuno, A.A. Moiseev, M. Mongelli, M.E. Monzani, A. Morselli, I.V. Moskalenko, S. Murgia, E. Nuss, M. Ohno, T. Ohsugi, N. Omodei, M. Orienti, E. Orlando, J.F. Ormes, D. Paneque, J.H. Panetta, J.S. Perkins, M. Pesce-Rollins, F. Piron, G. Pivato, T.A. Porter, J.L. Racusin, R. Rando, M. Razzano, S. Razzaque, A. Reimer, O. Reimer, T. Reposeur, L.S. Rochester, R.W. Romani, D. Salvetti, M. Sánchez-Conde, P.M. Saz Parkinson, A. Schulz, E.J. Siskind, D.A. Smith, F. Spada, G. Spandre, P. Spinelli, T.E. Stephens, A.W. Strong, D.J. Suson, H. Takahashi, T. Tanaka, J.G. Thayer, J.B. Thayer, D.J. Thompson, L. Tibaldo, O. Tibolla, D.F. Torres, E. Torresi, G. Tosti, E. Troja, B. Van Klaveren, G. Vianello, B.L. Winer, K.S. Wood, M. Wood, S. Zimmer, Fermi-LAT Collaboration, Fermi Large Area Telescope Third Source Catalog. *ApJS* **218**, 23 (2015). doi:10.1088/0067-0049/218/2/23
- B.S. Acharya, M. Actis, T. Aghajani, G. Agnetta, J. Aguilar, F. Aharonian, M. Ajello, A. Akhperjanian, M. Alcobierre, J. Aleksić, et al., Introducing the CTA concept. *Astropart.Phys.* **43**, 3–18 (2013). doi:10.1016/j.astropartphys.2013.01.007
- M. Ackermann, M. Ajello, W.B. Atwood, L. Baldini, J. Ballet, G. Barbiellini, D. Bastieri, J. Becerra Gonzalez, R. Bellazzini, E. Bissaldi, R.D. Blandford, E.D. Bloom, R. Bonino, E. Bottacini, T.J. Brandt, J. Bregeon, P. Bruel, R. Buehler, S. Buson, G.A. Caliandro, R.A. Cameron, R. Caputo, M. Caragiulo, P.A. Caraveo, E. Cavazzuti, C. Cecchi, E. Charles, A. Chekhtman, C.C. Cheung, J. Chiang, G. Chiaro, S. Ciprini, J.M. Cohen, J. Cohen-Tanugi, L.R. Cominsky, J. Conrad, A. Cuoco, S. Cutini, F. D'Ammando, A. de Angelis, F. de Palma, R. Desiante, M. Di Mauro, L. Di Venere, A. Domínguez, P.S. Drell, C. Favuzzi, S.J. Fegan, E.C. Ferrara, W.B. Focke, P. Fortin, A. Franckowiak, Y. Fukazawa, S. Funk, A.K. Furniss, P. Fusco, F. Gargano, D. Gasparrini, N. Giglietto, P. Giommi, F. Giordano, M. Giroletti, T. Glanzman, G. Godfrey, I.A. Grenier, M.-H. Grondin, L. Guillemot, S. Guiriec, A.K. Harding, E. Hays, J.W. Hewitt, A.B. Hill, D. Horan, G. Iafate, D. Hartmann, T. Jogler, G. Jóhannesson, A.S. Johnson, T. Kamae, J. Kataoka, J. Knödlseider, M. Kuss, G. La Mura, S. Larsson, L. Latronico, M. Lemoine-Goumard, J. Li, L. Li, F. Longo, F. Loparco, B. Lott, M.N. Lovellette, P. Lubrano, G.M. Madejski, S. Maldera, A. Manfreda, M. Mayer, M.N. Mazziotta, P.F. Michelson, N. Mirabal, W. Mitthumsiri, T. Mizuno, A.A. Moiseev, M.E. Monzani, A. Morselli, I.V. Moskalenko, S. Murgia, E. Nuss, T. Ohsugi, N. Omodei, M. Orienti, E. Orlando, J.F. Ormes, D. Paneque, J.S. Perkins, M. Pesce-Rollins, V. Petrosian, F. Piron, G. Pivato, T.A. Porter, S. Rainò, R. Rando, M. Razzano, S. Razzaque, A. Reimer, O. Reimer, T. Reposeur, R.W. Romani, M. Sánchez-Conde, P.M. Saz Parkinson, J. Schmid, A. Schulz, C. Sgrò, E.J. Siskind, F. Spada, G. Spandre, P. Spinelli, D.J. Suson, H. Tajima, H. Takahashi, M. Takahashi, T.

- Takahashi, J.B. Thayer, D.J. Thompson, L. Tibaldo, D.F. Torres, G. Tosti, E. Troja, G. Vianello, K.S. Wood, M. Wood, M. Yassine, G. Zaharijas, S. Zimmer, 2FHL: The Second Catalog of Hard Fermi-LAT Sources. *ApJS* **222**, 5 (2016). doi:10.3847/0067-0049/222/1/5
- M. Aguilar, D. Aisa, A. Alvino, G. Ambrosi, K. Andeen, L. Arruda, N. Attig, P. Azzarello, A. Bachlechner, F. Barao, et al., Electron and Positron Fluxes in Primary Cosmic Rays Measured with the Alpha Magnetic Spectrometer on the International Space Station. *PRL* **113**(12), 121102 (2014a). doi:10.1103/PhysRevLett.113.121102
- M. Aguilar, D. Aisa, B. Alpat, A. Alvino, G. Ambrosi, K. Andeen, L. Arruda, N. Attig, P. Azzarello, A. Bachlechner, et al., Precision Measurement of the ($e^+ + e^-$) Flux in Primary Cosmic Rays from 0.5 GeV to 1 TeV with the Alpha Magnetic Spectrometer on the International Space Station. *PRL* **113**(22), 221102 (2014b). doi:10.1103/PhysRevLett.113.221102
- F. Aharonian, A.G. Akhperjanian, K.-M. Aye, A.R. Bazer-Bachi, M. Beilicke, W. Benbow, D. Berge, P. Berghaus, K. Bernlöhr, C. Boisson, O. Bolz, I. Braun, F. Breitling, A.M. Brown, J. Bussons Gordo, P.M. Chadwick, L.-M. Chounet, R. Cornils, L. Costamante, B. Degrange, A. Djannati-Ataï, L. O'C. Drury, G. Dubus, D. Emmanoulopoulos, P. Espigat, F. Feinstein, P. Fleury, G. Fontaine, Y. Fuchs, S. Funk, Y.A. Gallant, B. Giebels, S. Gillessen, J.F. Glicenstein, P. Goret, C. Hadjichristidis, M. Hauser, G. Heinzelmann, G. Henri, G. Hermann, J.A. Hinton, W. Hofmann, M. Holleran, D. Horns, O.C. de Jager, B. Khélifi, N. Komin, A. Konopelko, I.J. Latham, R. Le Gallou, A. Lemièrre, M. Lemoine-Goumard, N. Leroy, T. Lohse, O. Martineau-Huynh, A. Marcowith, C. Masterson, T.J.L. McComb, M. de Naurois, S.J. Nolan, A. Noutsos, K.J. Orford, J.L. Osborne, M. Ouchrif, M. Panter, G. Pelletier, S. Pita, G. Pühlhofer, M. Punch, B.C. Raubenheimer, M. Raue, J. Raux, S.M. Rayner, I. Redondo, A. Reimer, O. Reimer, J. Ripken, L. Rob, L. Rolland, G. Rowell, V. Sahakian, L. Saugé, S. Schlenker, R. Schlickeiser, C. Schuster, U. Schwanke, M. Siewert, H. Sol, R. Steenkamp, C. Stegmann, J.-P. Tavernet, R. Terrier, C.G. Théoret, M. Tluczykont, G. Vasileiadis, C. Venter, P. Vincent, H.J. Völk, S.J. Wagner, Discovery of extended VHE gamma-ray emission from the asymmetric pulsar wind nebula in MSH 15-52 with HESS. *A&A* **435**, 17–20 (2005). doi:10.1051/0004-6361:200500105
- F. Aharonian, A.G. Akhperjanian, A.R. Bazer-Bachi, M. Beilicke, W. Benbow, D. Berge, K. Bernlöhr, C. Boisson, O. Bolz, V. Borrel, I. Braun, A.M. Brown, R. Bühler, I. Büsching, S. Carrigan, P.M. Chadwick, L.-M. Chounet, R. Cornils, L. Costamante, B. Degrange, H.J. Dickinson, A. Djannati-Ataï, L. O'C. Drury, G. Dubus, K. Egberts, D. Emmanoulopoulos, P. Espigat, F. Feinstein, E. Ferrero, A. Fiasson, G. Fontaine, S. Funk, S. Funk, M. Füßling, Y.A. Gallant, B. Giebels, J.F. Glicenstein, P. Goret, C. Hadjichristidis, D. Hauser, M. Hauser, G. Heinzelmann, G. Henri, G. Hermann, J.A. Hinton, A. Hoffmann, W. Hofmann, M. Holleran, D. Horns, A. Jacholkowska, O.C. de Jager, E. Kendziorra, B. Khélifi, N. Komin, A. Konopelko, K. Kosack, I.J. Latham, R. Le Gallou, A. Lemièrre, M. Lemoine-Goumard, T. Lohse, J.M. Martin, O. Martineau-Huynh, A. Marcowith, C. Masterson, G. Maurin, T.J.L. McComb, E. Moulin, M. de Naurois, D. Nedbal, S.J. Nolan, A. Noutsos, K.J. Orford, J.L. Osborne, M. Ouchrif, M. Panter, G. Pelletier, S. Pita, G. Pühlhofer, M. Punch, B.C. Raubenheimer, M. Raue, S.M. Rayner, A. Reimer, O. Reimer, J. Ripken, L. Rob, L. Rolland, G. Rowell, V. Sahakian, A. Santangelo, L. Saugé, S. Schlenker, R. Schlickeiser, R. Schröder, U. Schwanke, S. Schwarzburg, A. Shalchi, H. Sol, D. Spangler, F. Spanier, R. Steenkamp, C. Stegmann, G. Superina, J.-P. Tavernet, R. Terrier, C.G. Théoret, M. Tluczykont, C. van Eldik, G. Vasileiadis, C. Venter, P. Vincent, H.J. Völk, S.J. Wagner, M. Ward, Energy dependent γ -ray morphology in the pulsar wind nebula HESS J1825-137. *A&A* **460**, 365–374 (2006a). doi:10.1051/0004-6361:20065546
- F. Aharonian, A.G. Akhperjanian, A.R. Bazer-Bachi, M. Beilicke, W. Benbow, D. Berge, K. Bernlöhr, C. Boisson, O. Bolz, V. Borrel, I. Braun, F. Breitling, A.M. Brown, R. Bühler, I. Büsching, S. Carrigan, P.M. Chadwick, L.-M. Chounet, R. Cornils, L. Costamante, B. Degrange, H.J. Dickinson, A. Djannati-Ataï, L. O'C. Drury, G. Dubus, K. Egberts, D. Emmanoulopoulos, B. Epinat, P. Espigat, F. Feinstein, E. Ferrero, G. Fontaine, S. Funk, S. Funk, Y.A. Gallant, B. Giebels, J.F. Glicenstein, P. Goret, C. Hadjichristidis, D. Hauser, M. Hauser, G. Heinzelmann, G. Henri, G. Hermann, J.A. Hinton, W. Hofmann, M. Holleran, D. Horns, A. Jacholkowska, O.C. de Jager, B. Khélifi, N. Komin, A. Konopelko, I.J. Latham, R. Le Gallou, A. Lemièrre, M. Lemoine-Goumard, T. Lohse, J.M. Martin, O. Martineau-Huynh, A. Marcowith, C. Masterson, T.J.L. McComb, M. de Naurois, D. Nedbal, S.J. Nolan, A. Noutsos, K.J. Orford, J.L. Osborne, M. Ouchrif, M. Panter, G. Pelletier, S. Pita, G. Pühlhofer, M. Punch, B.C. Raubenheimer, M. Raue, S.M. Rayner, A. Reimer, O. Reimer, J. Ripken, L. Rob, L. Rolland, G. Rowell, V. Sahakian, L. Saugé, S. Schlenker, R. Schlickeiser, U. Schwanke, H. Sol, D. Spangler, F. Spanier, R. Steenkamp, C. Stegmann, G. Superina, J.-P. Tavernet, R. Terrier, C.G. Théoret, M. Tluczykont, C. van Eldik, G. Vasileiadis, C. Venter, P. Vincent, H.J. Völk, S.J. Wagner, M. Ward, First detection of a VHE gamma-ray spectral maximum from a cosmic source: HESS discovery of the Vela X nebula. *A&A* **448**, 43–47 (2006b). doi:10.1051/0004-6361:200600014
- E. Amato, Particle acceleration and radiation in Pulsar Wind Nebulae. *ArXiv e-prints* (2015)

- H. An, K.K. Madsen, S.P. Reynolds, V.M. Kaspi, F.A. Harrison, S.E. Boggs, F.E. Christensen, W.W. Craig, C.L. Fryer, B.W. Grefenstette, C.J. Hailey, K. Mori, D. Stern, W.W. Zhang, High-energy X-Ray Imaging of the Pulsar Wind Nebula MSH 15-52: Constraints on Particle Acceleration and Transport. *ApJ* **793**, 90 (2014). doi:10.1088/0004-637X/793/2/90
- Z. Arzoumanian, D.F. Chernoff, J.M. Cordes, The Velocity Distribution of Isolated Radio Pulsars. *ApJ* **568**, 289–301 (2002). doi:10.1086/338805
- Z. Arzoumanian, E.V. Gotthelf, S.M. Ransom, S. Safi-Harb, R. Kothes, T.L. Landecker, Discovery of an Energetic Pulsar Associated with SNR G76.9+1.0. *ApJ* **739**, 39 (2011). doi:10.1088/0004-637X/739/1/39
- K. Auchettl, P. Slane, R.W. Romani, B. Posselt, G.G. Pavlov, O. Kargaltsev, C.-Y. Ng, T. Temim, M.C. Weisskopf, A. Bykov, D.A. Swartz, X-Ray Analysis of the Proper Motion and Pulsar Wind Nebula for PSR J1741-2054. *ApJ* **802**, 68 (2015). doi:10.1088/0004-637X/802/1/68
- R. Bandiera, On the X-ray feature associated with the Guitar nebula. *A&A* **490**, 3–6 (2008). doi:10.1051/0004-6361:200810666
- R. Bandiera, F. Bocchino, The X-ray halo of G21.5 - 0.9. *Adv.Space Res.* **33**, 398–402 (2004). doi:10.1016/j.asr.2003.04.025
- M.F. Bietenholz, N. Bartel, The expansion and radio spectral index of G21.5-0.9: is PSR J1833-1034 the youngest pulsar? *MNRAS* **386**, 1411–1416 (2008). doi:10.1111/j.1365-2966.2008.13058.x
- L. Bîrzan, G.G. Pavlov, O. Kargaltsev, Chandra Observations of the Elusive Pulsar Wind Nebula around PSR B0656+14. *ApJ* **817**, 129 (2016). doi:10.3847/0004-637X/817/2/129
- E.L. Blanton, D.J. Helfand, ASCA Observations of the Composite Supernova Remnant G29.7-0.3. *ApJ* **470**, 961 (1996). doi:10.1086/177922
- J.M. Blondin, R.A. Chevalier, D.M. Frierson, Pulsar Wind Nebulae in Evolved Supernova Remnants. *ApJ* **563**, 806–815 (2001). doi:10.1086/324042
- F. Bocchino, Detection of thermal X-ray emission in the halo of the plerionic supernova remnant G21.5-0.9. *Adv.Space Res.* **35**, 1003–1006 (2005). doi:10.1016/j.asr.2005.01.045
- F. Bocchino, A.M. Bykov, The plerion nebula in IC 443: The XMM-Newton view. *A&A* **376**, 248–253 (2001). doi:10.1051/0004-6361:20010882
- S.E. Boggs, A. Zoglauer, E. Bellm, K. Hurley, R.P. Lin, D.M. Smith, C. Wigger, W. Hajdas, The Giant Flare of 2004 December 27 from SGR 1806-20. *ApJ* **661**, 458–467 (2007)
- M. Boudaud, S. Aupetit, S. Caroff, A. Putze, G. Belanger, Y. Genolini, C. Goy, V. Poireau, V. Poulin, S. Rosier, P. Salati, L. Tao, M. Vecchi, A new look at the cosmic ray positron fraction. *A&A* **575**, 67 (2015). doi:10.1051/0004-6361/201425197
- N. Bucciantini, E. Amato, L. Del Zanna, Relativistic MHD simulations of pulsar bow-shock nebulae. *A&A* **434**, 189–199 (2005). doi:10.1051/0004-6361:20042205
- N. Bucciantini, J. Arons, E. Amato, Modelling spectral evolution of pulsar wind nebulae inside supernova remnants. *MNRAS* **410**, 381–398 (2011). doi:10.1111/j.1365-2966.2010.17449.x
- A.M. Bykov, F.B.S. Paerels, V. Petrosian, Equilibration Processes in the Warm-Hot Intergalactic Medium. *SSR* **134**, 141–153 (2008). doi:10.1007/s11214-008-9309-4
- A. Bykov, N. Gehrels, H. Krawczynski, M. Lemoine, G. Pelletier, M. Pohl, Particle Acceleration in Relativistic Outflows. *SpSciRev* **173**, 309–339 (2012). doi:10.1007/s11214-012-9896-y
- P.B. Cameron, P. Chandra, A. Ray, S.R. Kulkarni, D.A. Frail, M.H. Wieringa, E. Nakar, E.S. Phinney, A. Miyazaki, M. Tsuboi, S. Okumura, N. Kawai, K.M. Menten, F. Bertoldi, Detection of a radio counterpart to the 27 December 2004 giant flare from SGR 1806 - 20. *Nature* **434**, 1112–1115 (2005). doi:10.1038/nature03605
- F. Camilo, R.N. Manchester, B.M. Gaensler, D.R. Lorimer, Heartbeat of the Mouse: A Young Radio Pulsar Associated with the Axisymmetric Nebula G359.23-0.82. *ApJ* **579**, 25–28 (2002). doi:10.1086/344832
- P.A. Caraveo, G.F. Bignami, A. De Luca, S. Mereghetti, A. Pellizzoni, R. Mignani, A. Tur, W. Becker, Geminga's Tails: A Pulsar Bow Shock Probing the Interstellar Medium. *Science* **301**, 1345–1348 (2003). doi:10.1126/science.1086973
- S. Chatterjee, J.M. Cordes, Bow Shocks from Neutron Stars: Scaling Laws and Hubble Space Telescope Observations of the Guitar Nebula. *ApJ* **575**, 407–418 (2002). doi:10.1086/341139
- J.M. Cordes, R.W. Romani, S.C. Lundgren, The Guitar nebula - A bow shock from a slow-spin, high-velocity neutron star. *Nature* **362**, 133–135 (1993). doi:10.1038/362133a0
- O.C. de Jager, A. Djannati-Ataï, Implications of HESS Observations of Pulsar Wind Nebulae **357**, 451 (2009). doi:10.1007/978-3-540-76965-1-17
- O.C. de Jager, S.E.S. Ferreira, A. Djannati-Ataï, M. Dalton, C. Deil, K. Kosack, M. Renaud, U. Schwanke, O. Tibolla, Unidentified Gamma-Ray Sources as Ancient Pulsar Wind Nebulae. *ArXiv e-prints* (2009)
- A. De Luca, M. Marelli, R.P. Mignani, P.A. Caraveo, W. Hummel, S. Collins, A. Shearer, P.M. Saz Parkinson, A. Belfiore, G.F. Bignami, Discovery of a Faint X-Ray Counterpart and a Parsec-long X-Ray Tail for the Middle-aged, γ -Ray-only Pulsar PSR J0357+3205. *ApJ* **733**, 104 (2011). doi:10.1088/0004-

- 637X/733/2/104
- A. De Luca, R.P. Mignani, M. Marelli, D. Salvetti, N. Sartore, A. Belfiore, P. Saz Parkinson, P.A. Caraveo, G.F. Bignami, PSR J0357+3205: A Fast-moving Pulsar with a Very Unusual X-Ray Trail. *ApJl* **765**, 19 (2013). doi:10.1088/2041-8205/765/1/L19
- E. de Oña-Wilhelmi, B. Rudak, J.A. Barrio, J.L. Contreras, Y. Gallant, D. Hadasch, T. Hassan, M. Lopez, D. Mazin, N. Mirabal, G. Pedalletti, M. Renaud, R. de los Reyes, D.F. Torres, CTA Consortium, Prospects for observations of pulsars and pulsar wind nebulae with CTA. *Astropart.Phys.* **43**, 287–300 (2013). doi:10.1016/j.astropartphys.2012.08.009
- A. de Rosa, P. Ubertini, R. Campana, A. Bazzano, A.J. Dean, L. Bassani, Hard X-ray observations of PSR J1833-1034 and its associated pulsar wind nebula. *MNRAS* **393**, 527–530 (2009). doi:10.1111/j.1365-2966.2008.14160.x
- L. Del Zanna, E. Amato, N. Bucciantini, Axially symmetric relativistic MHD simulations of Pulsar Wind Nebulae in Supernova Remnants. On the origin of torus and jet-like features. *A&A* **421**, 1063–1073 (2004). doi:10.1051/0004-6361:20035936
- S. Della Torre, M. Gervasi, P.G. Rancoita, D. Rozza, A. Treves, Pulsar Wind Nebulae as a source of the observed electron and positron excess at high energy: The case of Vela-X. *JHEAp* **8**, 27–34 (2015). doi:10.1016/j.jheap.2015.08.001
- M. Di Mauro, F. Donato, N. Fornengo, R. Lineros, A. Vittino, Interpretation of AMS-02 electrons and positrons data. *JCAP* **4**, 006 (2014). doi:10.1088/1475-7516/2014/04/006
- I. Di Palma, D. Guetta, E. Amato, Revised predictions of neutrino fluxes from Pulsar Wind Nebulae. *ArXiv e-prints* (2016)
- A. Djannati-Ataï, O.C. deJager, R. Terrier, Y.A. Gallant, S. Hoppe, New Companions for the lonely Crab? VHE emission from young pulsar wind nebulae revealed by H.E.S.S. *ICRC* **2**, 823–826 (2008)
- T. Dolch, S. Chatterjee, D.P. Clemens, J.M. Cordes, L.R. Cashmen, B.W. Taylor, Recent H-alpha Results on Pulsar B2224+65's Bow-Shock Nebula, the "Guitar". *Journal of Astronomy and Space Sciences* **33**, 167–172 (2016). doi:10.5140/JASS.2016.33.3.167
- G. Dubus, J.L. Contreras, S. Funk, Y. Gallant, T. Hassan, J. Hinton, Y. Inoue, J. Knödlseider, P. Martin, N. Mirabal, M. de Naurois, M. Renaud, CTA Consortium, Surveys with the Cherenkov Telescope Array. *Astropart.Phys.* **43**, 317–330 (2013). doi:10.1016/j.astropartphys.2012.05.020
- P. Esposito, G.L. Israel, R. Turolla, F. Mattana, A. Tiengo, A. Possenti, S. Zane, N. Rea, M. Burgay, D. Götz, S. Mereghetti, L. Stella, M.H. Wieringa, J.M. Sarkissian, T. Enoto, P. Romano, T. Sakamoto, Y.E. Nakagawa, K. Makishima, K. Nakazawa, H. Nishioka, C. François-Martin, Long-term spectral and timing properties of the soft gamma-ray repeater SGR 1833-0832 and detection of extended X-ray emission around the radio pulsar PSR B1830-08. *MNRAS* **416**, 205–215 (2011). doi:10.1111/j.1365-2966.2011.19022.x
- P. Esposito, A. Tiengo, N. Rea, R. Turolla, A. Fenzi, A. Giuliani, G.L. Israel, S. Zane, S. Mereghetti, A. Possenti, M. Burgay, L. Stella, D. Götz, R. Perna, R.P. Mignani, P. Romano, X-ray and radio observations of the magnetar Swift J1834.9-0846 and its dust-scattering halo. *MNRAS* **429**, 3123–3132 (2013). doi:10.1093/mnras/sts569
- J. Faherty, F.M. Walter, J. Anderson, The trigonometric parallax of the neutron star Geminga. *ApSpSci* **308**, 225–230 (2007). doi:10.1007/s10509-007-9368-0
- J. Fang, L. Zhang, Multiband emission from pulsar wind nebulae: a possible injection spectrum. *A&A* **515**, 20 (2010). doi:10.1051/0004-6361/200913615
- D.F. Figer, F. Najarro, R.P. Kudritzki, The Double-lined Spectrum of LBV 1806-20. *ApJl* **610**, 109–112 (2004). doi:10.1086/423306
- D.A. Frail, S.R. Kulkarni, J.S. Bloom, An outburst of relativistic particles from the soft γ -ray repeater SGR1900+14. *Nature* **398**, 127–129 (1999). doi:10.1038/18163
- D.A. Frail, G. Vasisht, S.R. Kulkarni, The Changing Structure of the Radio Nebula around the Soft Gamma-Ray Repeater SGR 1806-20. *ApJl* **480**, 129–132 (1997). doi:10.1086/310635
- D.D. Frederiks, S.V. Golenetskii, V.D. Palshin, R.L. Aptekar, V.N. Ilyinskii, F.P. Oleinik, E.P. Mazets, T.L. Cline, Giant flare in SGR 1806-20 and its Compton reflection from the Moon. *Astronomy Letters* **33**, 1–18 (2007). doi:10.1134/S106377370701001X
- E. Fuerst, T. Handa, K. Morita, P. Reich, W. Reich, Y. Sofue, Detection of axisymmetric filaments in the filled-center supernova remnant G21.5-0.9. *PASJ* **40**, 347–356 (1988)
- S. Funk, J.A. Hinton, O.C. De Jager, Energy Dependent Morphology in the PWN candidate HESS J1825-137. *ICRC* **2**, 605–608 (2008)
- B.M. Gaensler, P.O. Slane, The Evolution and Structure of Pulsar Wind Nebulae. *ARA&A* **44**, 17–47 (2006). doi:10.1146/annurev.astro.44.051905.092528
- B.M. Gaensler, B.J. Wallace, A Multifrequency Radio Study of Supernova Remnant G292.0+1.8 and Its Pulsar Wind Nebula. *ApJ* **594**, 326–339 (2003). doi:10.1086/376861

- B.M. Gaensler, K.T.S. Brazier, R.N. Manchester, S. Johnston, A.J. Green, SNR G320.4-01.2 and PSR B1509-58: new radio observations of a complex interacting system. *MNRAS* **305**, 724–736 (1999). doi:10.1046/j.1365-8711.1999.02500.x
- B.M. Gaensler, J. Arons, V.M. Kaspi, M.J. Pivovarov, N. Kawai, K. Tamura, Chandra Imaging of the X-Ray Nebula Powered by Pulsar B1509-58. *ApJ* **569**, 878–893 (2002). doi:10.1086/339354
- B.M. Gaensler, E. van der Swaluw, F. Camilo, V.M. Kaspi, F.K. Bagano, F. Yusef-Zadeh, R.N. Manchester, The Mouse that Soared: High-Resolution X-Ray Imaging of the Pulsar-powered Bow Shock G359.23-0.82. *ApJ* **616**, 383–402 (2004). doi:10.1086/424906
- B.M. Gaensler, C. Kouveliotou, J.D. Gelfand, G.B. Taylor, D. Eichler, R.A.M.J. Wijers, J. Granot, E. Ramirez-Ruiz, Y.E. Lyubarsky, R.W. Hunstead, D. Campbell-Wilson, A.J. van der Horst, M.A. McLaughlin, R.P. Fender, M.A. Garrett, K.J. Newton-McGee, D.M. Palmer, N. Gehrels, P.M. Woods, An expanding radio nebula produced by a giant flare from the magnetar SGR 1806-20. *Nature* **434**, 1104–1106 (2005). doi:10.1038/nature03498
- F.P. Gavril, M.E. Gonzalez, E.V. Gotthelf, V.M. Kaspi, M.A. Livingstone, P.M. Woods, Magnetar-Like Emission from the Young Pulsar in Kes 75. *Science* **319**, 1802 (2008). doi:10.1126/science.1153465
- J.D. Gelfand, P.O. Slane, W. Zhang, A Dynamical Model for the Evolution of a Pulsar Wind Nebula Inside a Nonradiative Supernova Remnant. *ApJ* **703**, 2051–2067 (2009). doi:10.1088/0004-637X/703/2/2051
- J.D. Gelfand, Y.E. Lyubarsky, D. Eichler, B.M. Gaensler, G.B. Taylor, J. Granot, K.J. Newton-McGee, E. Ramirez-Ruiz, C. Kouveliotou, R.A.M.J. Wijers, A Rebrightening of the Radio Nebula Associated with the 2004 December 27 Giant Flare from SGR 1806-20. *ApJL* **634**, 89–92 (2005). doi:10.1086/498643
- E.V. Gotthelf, J.A. Tomsick, J.P. Halpern, J.D. Gelfand, F.A. Harrison, S.E. Boggs, F.E. Christensen, W.W. Craig, J.C. Hailey, V.M. Kaspi, D.K. Stern, W.W. Zhang, NuSTAR Discovery of a Young, Energetic Pulsar Associated with the Luminous Gamma-Ray Source HESS J1640-465. *ApJ* **788**, 155 (2014). doi:10.1088/0004-637X/788/2/155
- J. Granot, E. Ramirez-Ruiz, G.B. Taylor, D. Eichler, Y.E. Lyubarsky, R.A.M.J. Wijers, B.M. Gaensler, J.D. Gelfand, C. Kouveliotou, Diagnosing the Outflow from the SGR 1806-20 Giant Flare with Radio Observations. *ApJ* **638**, 391–396 (2006). doi:10.1086/497680
- J. Granot, R. Gill, G. Younes, J. Gelfand, A. Harding, C. Kouveliotou, M.G. Baring, Learning about the magnetar Swift J1834.9-0846 from its wind nebula. *MNRAS* **464**, 4895–4926 (2017). doi:10.1093/mnras/stw2554
- L. Gratton, Source Models with Electron Diffusion. *Ap&SS* **16**, 81–100 (1972). doi:10.1007/BF00643094
- D.A. Green, A revised Galactic supernova remnant catalogue. *Bulletin of the Astronomical Society of India* **37**, 45–61 (2009)
- D.A. Green, P.A.G. Scheuer, Upper limits on the infrared flux density of the ‘filled-centre’ supernova remnant 3C58. *MNRAS* **258**, 833–840 (1992). doi:10.1093/mnras/258.4.833
- M.-H. Grondin, S. Funk, M. Lemoine-Goumard, A. Van Etten, J.A. Hinton, F. Camilo, I. Cognard, C.M. Espinoza, P.C.C. Freire, J.E. Grove, L. Guillemot, S. Johnston, M. Kramer, J. Lande, P. Michelson, A. Posenti, R.W. Romani, J.L. Skilton, G. Theureau, P. Weltevrede, Detection of the Pulsar Wind Nebula HESS J1825-137 with the Fermi Large Area Telescope. *ApJ* **738**, 42 (2011). doi:10.1088/0004-637X/738/1/42
- M.-H. Grondin, R.W. Romani, M. Lemoine-Goumard, L. Guillemot, A.K. Harding, T. Reposeur, The Vela-X Pulsar Wind Nebula Revisited with Four Years of Fermi Large Area Telescope Observations. *ApJ* **774**, 110 (2013). doi:10.1088/0004-637X/774/2/110
- C.A. Hales, B.M. Gaensler, S. Chatterjee, E. van der Swaluw, F. Camilo, A Proper Motion for the Pulsar Wind Nebula G359.23-0.82, the “Mouse,” Associated with the Energetic Radio Pulsar J1747-2958. *ApJ* **706**, 1316–1322 (2009). doi:10.1088/0004-637X/706/2/1316
- A.K. Harding, I. Contopoulos, D. Kazanas, Magnetar Spin-Down. *ApJL* **525**, 125–128 (1999). doi:10.1086/312339
- F.A. Harrison, W.W. Craig, F.E. Christensen, C.J. Hailey, W.W. Zhang, S.E. Boggs, D. Stern, W.R. Cook, K. Forster, P. Giommi, B.W. Grefenstette, Y. Kim, T. Kitaguchi, J.E. Koglin, K.K. Madsen, P.H. Mao, H. Miyasaka, K. Mori, M. Perri, M.J. Pivovarov, S. Puccetti, V.R. Rana, N.J. Westergaard, J. Willis, A. Zoglauer, H. An, M. Bachetti, N.M. Barrière, E.C. Bellm, V. Bhalerao, N.F. Brejnholt, F. Fuerst, C.C. Liebe, C.B. Markwardt, M. Nynka, J.K. Vogel, D.J. Walton, D.R. Wik, D.M. Alexander, L.R. Cominsky, A.E. Hornschemeier, A. Hornstrup, V.M. Kaspi, G.M. Madejski, G. Matt, S. Molendi, D.M. Smith, J.A. Tomsick, M. Ajello, D.R. Ballantyne, M. Baloković, D. Barret, F.E. Bauer, R.D. Blandford, W.N. Brandt, L.W. Brenneman, J. Chiang, D. Chakrabarty, J. Chenevez, A. Comastri, F. Dufour, M. Elvis, A.C. Fabian, D. Farrah, C.L. Fryer, E.V. Gotthelf, J.E. Grindlay, D.J. Helfand, R. Krivonos, D.L. Meier, J.M. Miller, L. Natalucci, P. Ogle, E.O. Ofek, A. Ptak, S.P. Reynolds, J.R. Rigby, G. Tagliaferri, S.E. Thorsett, E. Treister, C.M. Urry, The Nuclear Spectroscopic Telescope Array (NuSTAR) High-energy X-Ray Mission. *ApJ* **770**, 103 (2013). doi:10.1088/0004-637X/770/2/103
- D.J. Helfand, E.V. Gotthelf, J.P. Halpern, Vela Pulsar and Its Synchrotron Nebula. *ApJ* **556**, 380–391 (2001).

doi:10.1086/321533

- H.E.S.S. Collaboration, A. Abramowski, F. Acero, F. Aharonian, A.G. Akhperjanian, G. Anton, A. Balzer, A. Barnacka, U. Barres de Almeida, Y. Becherini, J. Becker, B. Behera, K. Bernlöhr, A. Bochow, C. Boisson, J. Bolmont, P. Bordas, J. Brucker, F. Brun, P. Brun, T. Bulik, I. Büsching, S. Carrigan, S. Casanova, M. Cerruti, P.M. Chadwick, A. Charbonnier, R.C.G. Chaves, A. Cheesebrough, L.-M. Chounet, A.C. Clapson, G. Coignet, G. Cologna, J. Conrad, M. Dalton, M.K. Daniel, I.D. Davids, B. Degrange, C. Deil, H.J. Dickinson, A. Djannati-Ataï, W. Domainko, L. O'C. Drury, F. Dubois, G. Dubus, K. Dutton, J. Dyks, M. Dyrdra, K. Egberts, P. Eger, P. Espigat, L. Fallon, C. Farnier, S. Fegan, F. Feinstein, M.V. Fernandes, A. Fiasson, G. Fontaine, A. Förster, M. Füssling, Y.A. Gallant, H. Gast, L. Gérard, D. Gerbig, B. Giebels, J.F. Glicenstein, B. Glück, P. Goret, D. Göring, S. Häffner, J.D. Hague, D. Hampf, M. Hauser, S. Heinz, G. Heinzlmann, G. Henri, G. Hermann, J.A. Hinton, A. Hoffmann, W. Hofmann, P. Hofverberg, M. Holler, D. Horns, A. Jacholkowska, O.C. de Jager, C. Jahn, M. Jamroz, I. Jung, M.A. Kastendieck, K. Katarzynski, U. Katz, S. Kaufmann, D. Keogh, D. Khangulyan, B. Khélifi, D. Klockov, W. Kluzniak, T. Kneiske, N. Komin, K. Kosack, R. Kossakowski, H. Laffon, G. Lamanna, D. Lennarz, T. Lohse, A. Lopatin, C.-C. Lu, V. Marandon, A. Marcowith, J. Masbou, D. Maurin, N. Maxted, M. Mayer, T.J.L. McComb, M.C. Medina, J. Méhault, R. Moderski, E. Moulin, C.L. Naumann, M. Naumann-Godo, M. de Naurois, D. Nedbal, D. Nekrassov, N. Nguyen, B. Nicholas, J. Niemiec, S.J. Nolan, S. Ohm, E. de Ona Wilhelmi, B. Opitz, M. Ostrowski, I. Oya, M. Panter, M. Paz Arribas, G. Pedalletti, G. Pelletier, P.-O. Petrucci, S. Pita, G. Pühlhofer, M. Punch, A. Quirrenbach, M. Raue, S.M. Rayner, A. Reimer, O. Reimer, M. Renaud, R. de Los Reyes, F. Rieger, J. Ripken, L. Rob, S. Rosier-Lees, G. Rowell, B. Rudak, C.B. Rulten, J. Ruppel, V. Sahakian, D. Sanchez, A. Santangelo, R. Schlickeiser, F.M. Schöck, A. Schulz, U. Schwanke, S. Schwarzburg, S. Schwemmer, M. Sikora, J.L. Skilton, H. Sol, G. Spengler, L. Stawarz, R. Steenkamp, C. Stegmann, F. Stinzing, K. Stycz, I. Sushch, A. Szostek, J.-P. Tavernier, R. Terrier, M. Tluczykont, K. Valerius, C. van Eldik, G. Vasileiadis, C. Venter, J.P. Vialle, A. Viana, P. Vincent, H.J. Völk, F. Volpe, S. Vorobiov, M. Vorster, S.J. Wagner, M. Ward, R. White, A. Wierchowska, M. Zacharias, A. Zajczyk, A.A. Zdziarski, A. Zech, H.-S. Zechlin, Discovery of the source HESS J1356-645 associated with the young and energetic PSR J1357-6429. *A&A* **533**, 103 (2011). doi:10.1051/0004-6361/201117445
- H.E.S.S. Collaboration, A. Abramowski, F. Aharonian, F. Ait Benkhali, A.G. Akhperjanian, E. Angüner, G. Anton, S. Balenderan, A. Balzer, A. Barnacka, et al., HESS J1818-154, a new composite supernova remnant discovered in TeV gamma rays and X-rays. *A&A* **562**, 40 (2014). doi:10.1051/0004-6361/201322914
- J.A. Hinton, S. Funk, R.D. Parsons, S. Ohm, Escape from Vela X. *ApJL* **743**, 7 (2011). doi:10.1088/2041-8205/743/1/L7
- D. Hooper, P. Blasi, P. Dario Serpico, Pulsars as the sources of high energy cosmic ray positrons. *JCAP* **1**, 025 (2009). doi:10.1088/1475-7516/2009/01/025
- C.Y. Hui, W. Becker, X-ray emission properties of the old pulsar PSR B2224+65. *A&A* **467**, 1209–1214 (2007). doi:10.1051/0004-6361:20066562
- G.L. Israel, P. Esposito, N. Rea, F. Coti Zelati, A. Tiengo, S. Campana, S. Mereghetti, G.A. Rodriguez Castillo, D. Götz, M. Burgay, A. Possenti, S. Zane, R. Turolla, R. Perna, G. Cannizzaro, J. Pons, The discovery, monitoring and environment of SGR J1935+2154. *MNRAS* **457**, 3448–3456 (2016). doi:10.1093/mnras/stw008
- S.P. Johnson, Q.D. Wang, The pulsar B2224+65 and its jets: a two epoch X-ray analysis. *MNRAS* **408**, 1216–1224 (2010). doi:10.1111/j.1365-2966.2010.17200.x
- P. Kaaret, H.L. Marshall, T.L. Aldcroft, D.E. Graessle, M. Karovska, S.S. Murray, A.H. Rots, N.S. Schulz, F.D. Seward, Chandra Observations of the Young Pulsar PSR B0540-69. *ApJ* **546**, 1159–1167 (2001). doi:10.1086/318287
- D.L. Kaplan, D.W. Fox, S.R. Kulkarni, E.V. Gotthelf, G. Vasisht, D.A. Frail, Precise Chandra Localization of the Soft Gamma-Ray Repeater SGR 1806-20. *ApJ* **564**, 935–940 (2002). doi:10.1086/324339
- N.S. Kardashev, Nonstationarity of Spectra of Young Sources of Nonthermal Radio Emission. *Sov.Astron.* **6**, 317 (1962)
- O. Kargaltsev, G.G. Pavlov, Pulsar Wind Nebulae in the Chandra Era, in *40 Years of Pulsars: Millisecond Pulsars, Magnetars and More*, ed. by C. Bassa, Z. Wang, A. Cumming, V.M. Kaspi American Institute of Physics Conference Series, vol. 983, 2008, pp. 171–185. doi:10.1063/1.2900138
- O. Kargaltsev, B. Rangelov, G.G. Pavlov, Gamma-ray and X-ray Properties of Pulsar Wind Nebulae and Unidentified Galactic TeV Sources. *ArXiv e-prints* (2013)
- O. Kargaltsev, Z. Misanovic, G.G. Pavlov, J.A. Wong, G.P. Garmire, X-Ray Observations of Parsec-scale Tails behind Two Middle-Aged Pulsars. *ApJ* **684**, 542–557 (2008). doi:10.1086/589145
- O. Kargaltsev, C. Kouveliotou, G.G. Pavlov, E. Göğüş, L. Lin, S. Wachter, R.L. Griffith, Y. Kaneko, G. Younes, X-Ray Observations of the New Unusual Magnetar Swift J1834.9-0846. *ApJ* **748**, 26 (2012).

- doi:10.1088/0004-637X/748/1/26
- C.F. Kennel, F.V. Coroniti, Confinement of the Crab pulsar's wind by its supernova remnant. *ApJ* **283**, 694–709 (1984a). doi:10.1086/162356
- C.F. Kennel, F.V. Coroniti, Magnetohydrodynamic model of Crab nebula radiation. *ApJ* **283**, 710–730 (1984b). doi:10.1086/162357
- H.L. Kestenbaum, W. Ku, R. Novick, R.S. Wolff, Measurement of the Spatial Structure of the X-Ray Source in the Crab Nebula. II. Observation of the 1974 December 28 Lunar Occultation. *ApJL* **202**, 21 (1975). doi:10.1086/181971
- J.G. Kirk, Y. Lyubarsky, J. Petri, The Theory of Pulsar Winds and Nebulae, in *Astrophysics and Space Science Library*, ed. by W. Becker Astrophysics and Space Science Library, vol. 357, 2009, p. 421. doi:10.1007/978-3-540-76965-1_16
- S. Klepser, S. Carrigan, E. de Oña Wilhelmi, C. Deil, A. Förster, V. Marandon, M. Mayer, K. Stycz, K. Valerius for the H. E. S. S. collaboration, A Population of Teraelectronvolt Pulsar Wind Nebulae in the H.E.S.S. Galactic Plane Survey. *ArXiv e-prints* (2013)
- N. Klingler, O. Kargaltsev, B. Rangelov, G.G. Pavlov, B. Posselt, C.-Y. Ng, Chandra Observations of Outflows from PSR J1509-5850. *ApJ* **828**, 70 (2016a). doi:10.3847/0004-637X/828/2/70
- N. Klingler, B. Rangelov, O. Kargaltsev, G.G. Pavlov, R.W. Romani, B. Posselt, P. Slane, T. Temim, C.-Y. Ng, N. Bucciantini, A. Bykov, D.A. Swartz, R. Buehler, Deep Chandra Observations of the Pulsar Wind Nebula Created by PSR B0355+54. *ApJ* **833**, 253 (2016b). doi:10.3847/1538-4357/833/2/253
- S.S. Komissarov, Y.E. Lyubarsky, Synchrotron nebulae created by anisotropic magnetized pulsar winds. *MNRAS* **349**, 779–792 (2004). doi:10.1111/j.1365-2966.2004.07597.x
- B.-C. Koo, C.F. McKee, K.-W. Suh, D.-S. Moon, T. Onaka, M.G. Burton, M. Hiramatsu, M.S. Bessell, B.M. Gaensler, H.-J. Kim, J.-J. Lee, W.-S. Jeong, H.-G. Lee, M. Im, K. Tatematsu, K. Kohno, R. Kawabe, H. Ezawa, G. Wilson, M.S. Yun, D.H. Hughes, IRAS 15099-5856: Remarkable Mid-infrared Source with Prominent Crystalline Silicate Emission Embedded in the Supernova Remnant MSH15-52. *ApJ* **732**, 6 (2011). doi:10.1088/0004-637X/732/1/6
- R. Kothés, T.L. Landecker, W. Reich, S. Safi-Harb, Z. Arzoumanian, DA 495: An Aging Pulsar Wind Nebula. *ApJ* **687**, 516–531 (2008). doi:10.1086/591653
- R. Kothés, X.H. Sun, W. Reich, T.J. Foster, G141.2+5.0, a New Pulsar Wind Nebula Discovered in the Cygnus Arm of the Milky Way. *ApJL* **784**, 26 (2014). doi:10.1088/2041-8205/784/2/L26
- C. Kouveliotou, A. Tennant, P.M. Woods, M.C. Weisskopf, K. Hurley, R.P. Fender, S.T. Garrington, S.K. Patel, E. Göğüş, Multiwavelength Observations of the Soft Gamma Repeater SGR 1900+14 during Its 2001 April Activation. *ApJ* **558**, 47–50 (2001). doi:10.1086/323496
- W. Ku, H.L. Kestenbaum, R. Novick, R.S. Wolff, Energy dependence of the size of the X-ray source in the Crab Nebula. *ApJL* **204**, 77–81 (1976). doi:10.1086/182058
- S.M. LaMassa, P.O. Slane, O.C. de Jager, Probing the Nature of the Vela X Cocoon. *ApJL* **689**, 121 (2008). doi:10.1086/595958
- T.L. Landecker, L.A. Higgs, H.J. Wendker, G76.9+1.0, A Supernova Remnant and Unusual Properties. *A&A* **276**, 522 (1993)
- C.C. Lang, Q.D. Wang, F. Lu, K.I. Clubb, The Radio Properties and Magnetic Field Configuration in the Crab-Like Pulsar Wind Nebula G54.1+0.3. *ApJ* **709**, 1125–1137 (2010). doi:10.1088/0004-637X/709/2/1125
- M. Lemoine-Goumard, V.E. Zavlin, M.-H. Grondin, R. Shannon, D.A. Smith, M. Burgay, F. Camilo, J. Cohen-Tanugi, P.C.C. Freire, J.E. Grove, L. Guillemot, S. Johnston, M. Keith, M. Kramer, R.N. Manchester, P.F. Michelson, D. Parent, A. Possenti, P.S. Ray, M. Renaud, S.E. Thorsett, P. Weltevrede, M.T. Wolff, Discovery of gamma- and X-ray pulsations from the young and energetic PSR J1357-6429 with Fermi and XMM-Newton. *A&A* **533**, 102 (2011). doi:10.1051/0004-6361/201117413
- F.J. Lu, Q.D. Wang, B. Aschenbach, P. Durouchoux, L.M. Song, Chandra Observation of Supernova Remnant G54.1+0.3: A Close Cousin of the Crab Nebula. *ApJL* **568**, 49–52 (2002). doi:10.1086/340137
- M. Lyutikov, Mass-loading of pulsar winds. *MNRAS* **339**, 623–632 (2003). doi:10.1046/j.1365-8711.2003.06141.x
- K.K. Madsen, S. Reynolds, F. Harrison, H. An, S. Boggs, F.E. Christensen, W.W. Craig, C.L. Fryer, B.W. Grefenstette, C.J. Hailey, C. Markwardt, M. Nynka, D. Stern, A. Zoglauer, W. Zhang, Broadband X-ray Imaging and Spectroscopy of the Crab Nebula and Pulsar with NuSTAR. *ApJ* **801**, 66 (2015). doi:10.1088/0004-637X/801/1/66
- R.N. Manchester, L. Staveley-Smith, M.J. Kesteven, The radio structure of supernova remnant 0540-693. *ApJ* **411**, 756–760 (1993). doi:10.1086/172877
- M. Marelli, A. De Luca, D. Salvetti, N. Sartore, A. Sartori, P. Caraveo, F. Pizzolato, P.M. Saz Parkinson, A. Belfiore, PSR J0357+3205: The Tail of the Turtle. *ApJ* **765**, 36 (2013). doi:10.1088/0004-637X/765/1/36
- J. Martín, D.F. Torres, N. Rea, Time-dependent modelling of pulsar wind nebulae: study on the impact of the diffusion-loss approximations. *MNRAS* **427**, 415–427 (2012). doi:10.1111/j.1365-2966.2012.22014.x

- H. Matheson, S. Safi-Harb, The plerionic supernova remnant G21.5-0.9: In and out. *Adv.Space Res.* **35**, 1099–1105 (2005). doi:10.1016/j.asr.2005.04.050
- H. Matheson, S. Safi-Harb, The Plerionic Supernova Remnant G21.5-0.9 Powered by PSR J1833-1034: New Spectroscopic and Imaging Results Revealed with the Chandra X-ray Observatory. *ApJ* **724**, 572–587 (2010). doi:10.1088/0004-637X/724/1/572
- F. Mattana, D. Götz, R. Terrier, L. Bouchet, G. Ponti, M. Falanga, M. Renaud, I. Caballero, S. Soldi, J.A. Zurita Heras, S. Schanne, Extended Hard X-Ray Emission from the Vela Pulsar Wind Nebula. *ApJL* **743**, 18 (2011). doi:10.1088/2041-8205/743/1/L18
- K.E. McGowan, W.T. Vestrand, J.A. Kennea, S. Zane, M. Cropper, F.A. Córdova, Probing the Pulsar Wind Nebula of PSR B0355+54. *ApJ* **647**, 1300–1308 (2006). doi:10.1086/505522
- S. Mereghetti, J.A. Pons, A. Melatos, Magnetars: Properties, Origin and Evolution. *SpSciRev* **191**, 315–338 (2015). doi:10.1007/s11214-015-0146-y
- S. Mereghetti, D. Götz, A. von Kienlin, A. Rau, G. Lichti, G. Weidenspointner, P. Jean, The First Giant Flare from SGR 1806-20: Observations Using the Anticoincidence Shield of the Spectrometer on INTEGRAL. *ApJL* **624**, 105–108 (2005). doi:10.1086/430669
- R.P. Mignani, G.G. Pavlov, O. Kargaltsev, Optical-Ultraviolet Spectrum and Proper Motion of the Middle-aged Pulsar B1055-52. *ApJ* **720**, 1635–1643 (2010). doi:10.1088/0004-637X/720/2/1635
- K. Mori, D.N. Burrows, J.J. Hester, G.G. Pavlov, S. Shibata, H. Tsunemi, Spatial Variation of the X-Ray Spectrum of the Crab Nebula. *ApJ* **609**, 186–193 (2004). doi:10.1086/421011
- G. Morlino, M. Lyutikov, M. Vorster, Mass loading of bow shock pulsar wind nebulae. *MNRAS* **454**, 3886–3901 (2015). doi:10.1093/mnras/stv2189
- E. Nakar, T. Piran, R. Sari, Pure and Loaded Fireballs in Soft Gamma-Ray Repeater Giant Flares. *ApJ* **635**, 516–521 (2005). doi:10.1086/497296
- C.-Y. Ng, B.M. Gaensler, S. Chatterjee, S. Johnston, Radio Polarization Observations of G319.9-0.7: A Bow-Shock Nebula with an Azimuthal Magnetic Field Powered by Pulsar J1509-5850. *ApJ* **712**, 596–603 (2010). doi:10.1088/0004-637X/712/1/596
- M. Nynka, C.J. Hailey, S.P. Reynolds, H. An, F.K. Baganoff, S.E. Boggs, F.E. Christensen, W.W. Craig, E.V. Gotthelf, B.W. Grefenstette, F.A. Harrison, R. Krivonos, K.K. Madsen, K. Mori, K. Perez, D. Stern, D.R. Wik, W.W. Zhang, A. Zoglauer, NuSTAR Study of Hard X-Ray Morphology and Spectroscopy of PWN G21.5-0.9. *ApJ* **789**, 72 (2014). doi:10.1088/0004-637X/789/1/72
- S.A. Olausen, V.M. Kaspi, The McGill Magnetar Catalog. *ApJS* **212**, 6 (2014). doi:10.1088/0067-0049/212/1/6
- F. Pacini, M. Salvati, On the Evolution of Supernova Remnants. Evolution of the Magnetic Field, Particles, Content, and Luminosity. *ApJ* **186**, 249–266 (1973). doi:10.1086/152495
- S. Park, J.P. Hughes, P.O. Slane, D.N. Burrows, B.M. Gaensler, P. Ghavamian, A Half-Megasecond Chandra Observation of the Oxygen-rich Supernova Remnant G292.0+1.8. *ApJL* **670**, 121–124 (2007). doi:10.1086/524406
- L. Pavan, G. Pühlhofer, P. Bordas, M. Audard, M. Balbo, E. Bozzo, D. Eckert, C. Ferrigno, M.D. Filipović, M. Verdugo, R. Walter, Closer view of the IGR J11014-6103 outflows. *A&A* **591**, 91 (2016). doi:10.1051/0004-6361/201527703
- G.G. Pavlov, S. Bhattacharyya, V.E. Zavlin, New X-ray Observations of the Geminga Pulsar Wind Nebula. *ApJ* **715**, 66–77 (2010). doi:10.1088/0004-637X/715/1/66
- G.G. Pavlov, O. Kargaltsev, W.F. Briskin, Chandra Observation of PSR B1823-13 and Its Pulsar Wind Nebula. *ApJ* **675**, 683–694 (2008). doi:10.1086/525842
- G.G. Pavlov, D. Sanwal, V.E. Zavlin, The Pulsar Wind Nebula of the Geminga Pulsar. *ApJ* **643**, 1146–1150 (2006). doi:10.1086/503250
- G.G. Pavlov, M.A. Teter, O. Kargaltsev, D. Sanwal, The Variable Jet of the Vela Pulsar. *ApJ* **591**, 1157–1171 (2003). doi:10.1086/375531
- Planck Collaboration, M. Arnaud, M. Ashdown, F. Atrio-Barandela, J. Aumont, C. Baccigalupi, A.J. Banday, R.B. Barreiro, E. Battaner, K. Benabed, A. Benoit-Lévy, J.-P. Bernard, M. Bersanelli, P. Bielewicz, J. Bobin, J.R. Bond, J. Borrill, F.R. Bouchet, C.L. Brogan, C. Burigana, J.-F. Cardoso, A. Catalano, A. Chamballu, H.C. Chiang, P.R. Christensen, S. Colombi, L.P.L. Colombo, B.P. Crill, A. Curto, F. Cuttaia, R.D. Davies, R.J. Davis, P. de Bernardis, A. de Rosa, G. de Zotti, J. Delabrouille, F.-X. Désert, C. Dickinson, J.M. Diego, S. Donzelli, O. Doré, X. Dupac, T.A. Enßlin, H.K. Eriksen, F. Finelli, O. Forni, M. Frailis, A.A. Fraisse, E. Franceschi, S. Galeotta, K. Ganga, M. Giard, Y. Giraud-Héraud, J. González-Nuevo, K.M. Górski, A. Gregorio, A. Gruppuso, F.K. Hansen, D.L. Harrison, C. Hernández-Monteagudo, D. Herranz, S.R. Hildebrandt, M. Hobson, W.A. Holmes, K.M. Huffenberger, A.H. Jaffe, T.R. Jaffe, E. Keihänen, R. Keskitalo, T.S. Kisner, R. Kneissl, J. Knoche, M. Kunz, H. Kurki-Suonio, A. Lähteenmäki, J.-M. Lamarre, A. Lasenby, C.R. Lawrence, R. Leonardi, M. Liguori, P.B. Lilje, M. Linden-Vørnle, M. López-Caniego, P.M. Lubin, D. Maino, M. Maris, D.J. Marshall, P.G. Martin, E.

- Martínez-González, S. Masi, S. Matarrese, P. Mazzotta, A. Melchiorri, L. Mendes, A. Mennella, M. Migliaccio, M.-A. Miville-Deschênes, A. Moneti, L. Montier, G. Morgante, D. Mortlock, D. Munshi, J.A. Murphy, P. Naselsky, F. Nati, F. Noviello, D. Novikov, I. Novikov, N. Oppermann, C.A. Oxborrow, L. Pagano, F. Pajot, R. Paladini, F. Pasian, M. Peel, O. Perdereau, F. Perrotta, F. Piacentini, M. Piat, D. Pietrobon, S. Plaszczyński, E. Pointecouteau, G. Polenta, L. Popa, G.W. Pratt, J.-L. Puget, J.P. Rachen, W.T. Reach, W. Reich, M. Reinecke, M. Remazeilles, C. Renault, J. Rho, S. Ricciardi, T. Riller, I. Ristorcelli, G. Rocha, C. Rosset, G. Roudier, B. Rusholme, M. Sandri, G. Savini, D. Scott, V. Stolyarov, D. Sutton, A.-S. Suur-Uski, J.-F. Sygnet, J.A. Tauber, L. Terenzi, L. Toffolatti, M. Tomasi, M. Tristram, M. Tucci, G. Umana, L. Valenziano, J. Valiviita, B. Van Tent, P. Vielva, F. Villa, L.A. Wade, D. Yvon, A. Zacchei, A. Zonca, Planck intermediate results. XXXI. Microwave survey of Galactic supernova remnants. *A&A* **586**, 134 (2016). doi:10.1051/0004-6361/201425022
- T.A. Porter, A.W. Strong, A new estimate of the Galactic interstellar radiation field between 0.1 μ m and 1000 μ m. *ICRC* **4**, 77 (2005)
- B. Posselt, G. Spence, G.G. Pavlov, A Chandra Search for a Pulsar Wind Nebula around PSR B1055-52. *ApJ* **811**, 96 (2015). doi:10.1088/0004-637X/811/2/96
- B. Posselt, G.G. Pavlov, P.O. Slane, R. Romani, N. Bucciantini, A.M. Bykov, O. Kargaltsev, M.C. Weisskopf, C.-Y. Ng, Geminga's puzzling pulsar wind nebula. *ArXiv e-prints* (2016)
- S.P. Reynolds, Magnetohydrodynamic Models for the Structure of Pulsar-Wind Nebulae. *ArXiv Astrophysics e-prints* (2003)
- S.P. Reynolds, Synchrotron-Loss Spectral Breaks in Pulsar-Wind Nebulae and Extragalactic Jets. *ApJ* **703**, 662–670 (2009). doi:10.1088/0004-637X/703/1/662
- S.P. Reynolds, H.D. Aller, Radio observations of the Crab-like supernova remnant 3C 58. I - Total intensity observations. *ApJ* **327**, 845–852 (1988). doi:10.1086/166242
- S.P. Reynolds, K.J. Borkowski, A Compact X-Ray Source in the Radio Pulsar-wind Nebula G141.2+5.0. *ApJL* **816**, 27 (2016). doi:10.3847/2041-8205/816/2/L27
- S.P. Reynolds, R.A. Chevalier, Evolution of pulsar-driven supernova remnants. *ApJ* **278**, 630–648 (1984). doi:10.1086/161831
- S.P. Reynolds, F.C. Jones, A Green's Function Solution for the Spherical Diffusion Equation in the Presence of Energy Losses, and its Applications to Crablike Supernova Remnants. *International Cosmic Ray Conference* **2**, 400 (1991)
- M.S.E. Roberts, C.R. Tam, V.M. Kaspi, M. Lyutikov, G. Vasisht, M. Pivovarov, E.V. Gotthelf, N. Kawai, The Pulsar Wind Nebula in G11.2-0.3. *ApJ* **588**, 992–1002 (2003). doi:10.1086/374266
- R.W. Romani, M.S. Shaw, F. Camilo, G. Cotter, G.R. Sivakoff, The Balmer-dominated Bow Shock and Wind Nebula Structure of γ -ray Pulsar PSR J1741-2054. *ApJ* **724**, 908–914 (2010). doi:10.1088/0004-637X/724/2/908
- M.M. Romanova, G.A. Chulsky, R.V.E. Lovelace, Winds, B-Fields, and Magnetotails of Pulsars. *ApJ* **630**, 1020–1028 (2005). doi:10.1086/431727
- C.J. Salter, S.P. Reynolds, D.E. Hogg, J.M. Payne, P.J. Rhodes, 84 gigahertz observations of five Crab-like supernova remnants. *ApJ* **338**, 171–177 (1989). doi:10.1086/167191
- N.I. Serafimovich, Y.A. Shibano, P. Lundqvist, J. Sollerman, The young pulsar PSR B0540-69.3 and its synchrotron nebula in the optical and X-rays. *A&A* **425**, 1041–1060 (2004). doi:10.1051/0004-6361:20040499
- F.D. Seward, F.R. Harnden Jr., A new, fast X-ray pulsar in the supernova remnant MSH 15-52. *ApJL* **256**, 45–47 (1982). doi:10.1086/183793
- P. Slane, Y. Chen, N.S. Schulz, F.D. Seward, J.P. Hughes, B.M. Gaensler, Chandra Observations of the Crab-like Supernova Remnant G21.5-0.9. *ApJL* **533**, 29–32 (2000). doi:10.1086/312589
- P. Slane, D.J. Helfand, E. van der Swaluw, S.S. Murray, New Constraints on the Structure and Evolution of the Pulsar Wind Nebula 3C 58. *ApJ* **616**, 403–413 (2004). doi:10.1086/424814
- P. Slane, D.J. Helfand, S.P. Reynolds, B.M. Gaensler, A. Lemièrre, Z. Wang, The Infrared Detection of the Pulsar Wind Nebula in the Galactic Supernova Remnant 3C 58. *ApJL* **676**, 33 (2008). doi:10.1086/587031
- S.J. Tanaka, F. Takahara, A Model of the Spectral Evolution of Pulsar Wind Nebulae. *ApJ* **715**, 1248–1257 (2010). doi:10.1088/0004-637X/715/2/1248
- S.J. Tanaka, F. Takahara, Study of Four Young TeV Pulsar Wind Nebulae with a Spectral Evolution Model. *ApJ* **741**, 40 (2011). doi:10.1088/0004-637X/741/1/40
- X. Tang, R.A. Chevalier, Particle Transport in Young Pulsar Wind Nebulae. *ApJ* **752**, 83 (2012). doi:10.1088/0004-637X/752/2/83
- T. Temim, R.D. Gehrz, C.E. Woodward, T.L. Roellig, N. Smith, L. Rudnick, E.F. Polomski, K. Davidson, L. Yuen, T. Onaka, Spitzer Space Telescope Infrared Imaging and Spectroscopy of the Crab Nebula. *AJ* **132**, 1610–1623 (2006). doi:10.1086/507076
- T. Temim, P. Slane, S.P. Reynolds, J.C. Raymond, K.J. Borkowski, Deep Chandra Observations of the Crab-

- like Pulsar Wind Nebula G54.1+0.3 and Spitzer Spectroscopy of the Associated Infrared Shell. *ApJ* **710**, 309–324 (2010). doi:10.1088/0004-637X/710/1/309
- T. Temim, P. Slane, C. Kolb, J. Blondin, J.P. Hughes, N. Bucciantini, Late-Time Evolution of Composite Supernova Remnants: Deep Chandra Observations and Hydrodynamical Modeling of a Crushed Pulsar Wind Nebula in SNR G327.1-1.1. *ApJ* **808**, 100 (2015). doi:10.1088/0004-637X/808/1/100
- C. Thompson, R.C. Duncan, The Soft Gamma Repeaters as Very Strongly Magnetized Neutron Stars. II. Quiescent Neutrino, X-Ray, and Alfvén Wave Emission. *ApJ* **473**, 322–342 (1996). doi:10.1086/178147
- W.W. Tian, Z. Li, D.A. Leahy, Q.D. Wang, VLA and XMM-Newton Observations of the SNR W41/TeV Gamma-Ray Source HESS J1834-087. *ApJ* **657**, 25–28 (2007). doi:10.1086/512544
- A. Tiengo, G. Vianello, P. Esposito, S. Mereghetti, A. Giuliani, E. Costantini, G.L. Israel, L. Stella, R. Turolla, S. Zane, N. Rea, D. Götz, F. Bernardini, A. Moretti, P. Romano, M. Ehle, N. Gehrels, The Dust-scattering X-ray Rings of the Anomalous X-ray Pulsar 1E 1547.0-5408. *ApJ* **710**, 227–235 (2010a). doi:10.1088/0004-637X/710/1/227
- A. Tiengo, G. Vianello, P. Esposito, S. Mereghetti, The spectacular X-ray echo of a magnetar burst. *X-ray Astronomy 2009: Present Status, Multi-Wavelength Approach and Future Perspectives* **1248**, 81–84 (2010b). doi:10.1063/1.3475361
- H. Tong, On the possible wind nebula of magnetar Swift J1834.9-0846: a magnetism-powered synchrotron nebula. *Res.Astron.Astrophys.* **16**, 143 (2016). doi:10.1088/1674-4527/16/9/143
- D.F. Torres, A rotationally-powered magnetar nebula around Swift J1834.9-0846. *ArXiv e-prints* (2016)
- D.F. Torres, A. Cillis, J. Martín, E. de Oña Wilhelmi, Time-dependent modeling of TeV-detected, young pulsar wind nebulae. *JHEAp* **1**, 31–62 (2014). doi:10.1016/j.jheap.2014.02.001
- E. van der Swaluw, T.P. Downes, R. Keegan, An evolutionary model for pulsar-driven supernova remnants. A hydrodynamical model. *A&A* **420**, 937–944 (2004). doi:10.1051/0004-6361:20035700
- E. van der Swaluw, A. Achterberg, Y.A. Gallant, G. Tóth, Pulsar wind nebulae in supernova remnants. Spherically symmetric hydrodynamical simulations. *A&A* **380**, 309–317 (2001). doi:10.1051/0004-6361:20011437
- A. Van Etten, R.W. Romani, Multi-zone Modeling of the Pulsar Wind Nebula HESS J1825-137. *ApJ* **742**, 62 (2011). doi:10.1088/0004-637X/742/2/62
- D. Viganò, N. Rea, P. Esposito, S. Mereghetti, G.L. Israel, A. Tiengo, R. Turolla, S. Zane, L. Stella, Searching for small-scale diffuse emission around SGR 1806-20. *Journal of High Energy Astrophysics* **3**, 41–46 (2014). doi:10.1016/j.jheap.2014.10.001
- M. Vigelius, A. Melatos, S. Chatterjee, B.M. Gaensler, P. Ghavamian, Three-dimensional hydrodynamic simulations of asymmetric pulsar wind bow shocks. *MNRAS* **374**, 793–808 (2007). doi:10.1111/j.1365-2966.2006.11193.x
- M.J. Vorster, O. Tibolla, S.E.S. Ferreira, S. Kaufmann, Time-dependent Modeling of Pulsar Wind Nebulae. *ApJ* **773**, 139 (2013). doi:10.1088/0004-637X/773/2/139
- K.W. Weiler, N. Panagia, Are Crab-type Supernova Remnants (Plerions) Short-lived? *A&A* **70**, 419 (1978)
- M.C. Weisskopf, J.J. Hester, A.F. Tennant, R.F. Elsner, N.S. Schulz, H.L. Marshall, M. Karovska, J.S. Nichols, D.A. Swartz, J.J. Kolodziejczak, S.L. O'Dell, Discovery of Spatial and Spectral Structure in the X-Ray Emission from the Crab Nebula. *ApJ* **536**, 81–84 (2000). doi:10.1086/312733
- F.P. Wilkin, Modeling Nonaxisymmetric Bow Shocks: Solution Method and Exact Analytic Solutions. *ApJ* **532**, 400–414 (2000). doi:10.1086/308576
- B.J. Williams, K.J. Borkowski, S.P. Reynolds, J.C. Raymond, K.S. Long, J. Morse, W.P. Blair, P. Ghavamian, R. Sankrit, S.P. Hendrick, R.C. Smith, S. Points, P.F. Winkler, Ejecta, Dust, and Synchrotron Radiation in SNR B0540–69.3: A More Crab-Like Remnant than the Crab. *ApJ* **687**, 1054–1069 (2008). doi:10.1086/592139
- D.S. Wong, J.M. Cordes, S. Chatterjee, E.G. Zweibel, J.P. Finley, R.W. Romani, M.P. Ulmer, Chandra Observations of the Guitar Nebula, in *High Energy Processes and Phenomena in Astrophysics*, ed. by X.D. Li, V. Trimble, Z.R. Wang IAU Symposium, vol. 214, 2003, p. 135
- G. Younes, C. Kouveliotou, O. Kargaltsev, G.G. Pavlov, E. Göğüş, S. Wachter, XMM-Newton View of Swift J1834.9-0846 and Its Magnetar Wind Nebula. *ApJ* **757**, 39 (2012). doi:10.1088/0004-637X/757/1/39
- G. Younes, C. Kouveliotou, O. Kargaltsev, R. Gill, J. Granot, A.L. Watts, J. Gelfand, M.G. Baring, A. Harding, G.G. Pavlov, A.J. van der Horst, D. Huppenkothen, E. Göğüş, L. Lin, O.J. Roberts, The wind nebula around magnetar Swift J1834.9-0846. *ArXiv e-prints* (2016)
- G. Younes, C. Kouveliotou, A. Jaodand, M.G. Baring, A.J. van der Horst, A.K. Harding, J.W.T. Hessels, N. Gehrels, R. Gill, D. Huppenkothen, J. Granot, E. Göğüş, L. Lin, X-ray and radio observations of the magnetar SGR J1935+2154 during its 2014, 2015, and 2016 outbursts. *ArXiv e-prints* (2017)
- F. Yusef-Zadeh, J. Bally, A non-thermal axially symmetric radio wake towards the Galactic centre. *Nature* **330**, 455–458 (1987). doi:10.1038/330455a0
- F. Yusef-Zadeh, B.M. Gaensler, A radio study of the mouse, G359.23 - 0.82. *Advances in Space Research*

- 35**, 1129–1136 (2005). doi:10.1016/j.asr.2005.03.003
- A. Zajczyk, Y.A. Gallant, P. Slane, S.P. Reynolds, R. Bandiera, C. Gouiffès, E. Le Floch, F. Comerón, L. Koch Miramond, Infrared imaging and polarimetric observations of the pulsar wind nebula in SNR G21.5-0.9. *A&A* **542**, 12 (2012). doi:10.1051/0004-6361/201117194
- S.V. Zharikov, D.A. Zyuzin, Y.A. Shibano, R.E. Mennickent, The PSR J1124-5916 wind nebula in the near-infrared. *A&A* **554**, 120 (2013). doi:10.1051/0004-6361/201321283